THE UNIVERSITY OF CHICAGO

# OXIDATION OF SEMICONDUCTORS AND SEMIMETALS BY SUPERSONIC BEAMS OF $O_2$ WITH SCANNING TUNNELING MICROSCOPY VISUALIZATION

A DISSERTATION SUBMITTED TO
THE FACULTY OF THE DIVISION OF THE PHYSICAL SCIENCES
IN CANDIDACY FOR THE DEGREE OF
DOCTOR OF PHILOSOPHY

DEPARTMENT OF CHEMISTRY

BY
ROSS ANTHONY EDEL

CHICAGO, ILLINOIS
DECEMBER 2019

The true delight is in the finding out rather than in the knowing.

-Isaac Asimov

# Table of Contents

## List of Figures

# List of Tables

# Acknowledgments

Thank you to my advisor Professor Steven Sibener, for always pushing me to be the best scientist I can be.

Thank you to my thesis committee, Professors Sarah King and Andrei Tokmakoff, for all of your advice.

Thank you to Tim, for being the consummate lab partner all these years; without you this dissertation would weigh a lot less.

Thank you to Brian, for patiently teaching me how to do everything back when I was new and couldn't even pronounce the word Auger.

Thank you to all of my friends and coworkers in the Sibener group: Michelle Brann, Sarah Brown, Rachael Farber, Jacob Graham, Zack Hund, Grant Langlois, Wenxin Li, Alison McMillan, Julia Murphy, Kevin Nihill, Jon Raybin, Jeff Sayler, Becca Thompson, Caleb Thompson, Darren Veit, and Sarah Willson, for all of your help and advice, and for making graduate school more fun than I ever could have expected.

Thank you to Kevin Gibson, who has forgotten more about running experiments than I will ever know.

Thank you to John Philips, without whom the lab would be underwater by now.

Thank you to Maria Jimenez and Tanya Hagerman, who keep the group running.

Thank you to Melissa and Andy, whose friendship has kept me mostly sane.

Thank you to my parents, who supported and believed in me even when I didn't.

Thank you to my sister Claire; I’m glad mom and dad didn’t take you back to the hospital like I told them to.

Thank you to Paloma, my favorite person in the world. You’re the best thing that happened to me during grad school and I hope to someday measure up to your first love, a poster of Legolas.

# Abstract

The research presented in this dissertation examines the oxidation of semiconductor and semimetal surfaces using a novel, one-of-a-kind instrument that combines a supersonic molecular beam with an in-line scanning tunneling microscope (STM) in ultra-high vacuum. This new approach to surface reaction dynamics provides spatio-temporal information on surface oxidation over nanoscopic and mesoscopic length scales. We have uncovered the kinetic and morphological effects of oxidation conditions on three technologically relevant surfaces: Si(111)-7×7, highly oriented pyrolytic graphite (HOPG), and GaAs(110). A complete understanding of the oxidation mechanism of these surfaces is critical due to their technological applications and roles as model systems. Samples were exposed to $O_2$ with kinetic energies from 0.4-1.2 eV and impingement angles 0-45° from normal, with STM characterization between exposures. In some cases, we were able to monitor the evolution of specific features by revisiting the same nanoscopic locations. Our study of Si(111)-7×7 revealed two oxidation channels, leading to the formation of dark and bright reacted sites. The dark sites dominated the surface and exhibited almost no site selectivity while the bright sites preferred the corner sites of the 7×7 unit cell. Our observations suggest that two adsorption pathways, trapping-mediated and direct chemisorption, occur simultaneously. On HOPG, we found that different oxygen energies, incident angles, and surface temperatures produce morphologically distinct etching features: Anisotropic channels, circular pits, and hexagonal pits. Reaction probability increased with beam energy and demonstrated non-Arrhenius behavior with respect to surface temperature, peaking at around 1375 K. Finally, oxidation of GaAs(110) was found to proceed by two morphologically distinct, competing mechanisms: a homogeneous process leading to layer-by-layer oxide growth, and a heterogeneous process with oxide islands nucleating from surface defects. The rates of both mechanisms change with $O_2$ kinetic energy, with homogeneous oxidation dominating at lower energies (<0.7 eV) and heterogeneous oxidation with higher energies (≥1.0 eV). In all three cases multiple oxidation mechanisms existed simultaneously on the surface, which could only be distinguished with exacting control over reaction conditions and high spatial resolution. The results obtained in this work provide vital information about the morphological evolution and kinetics of semiconductor and semimetals, offering a comprehensive overview of the spatio-temporal correlations that govern oxidation dynamics on surfaces.

# Chapter 1: Introduction

The experiments described in this dissertation rely on a combination of techniques that allow exacting control over experimental conditions and detailed characterization of the outcome of reactions resolved in both time and space. To effectively study gas-surface reactions, samples must be isolated in ultra-high vacuum (UHV) to ensure exposure to only the intended reactant. Our UHV system has a base pressure of better than $5\times10^{-11}$ torr. Given that a monolayer of adsorbed molecules forms in about 1 second at a pressure of $1\times10^{-6}$ torr, it can be expected that it would take more than five hours of exposure to background gas in our chamber for a monolayer of an unintended species to form. In reality, the low reactivity of many of the samples used for this research towards common background gases such as hydrogen, nitrogen, and water ensures sample cleanliness for even longer. The reactant of interest, here oxygen, is introduced by way of a supersonic molecular beam (SMB), a method which allows the kinetic energy and impingement angle of gas molecules to be tightly controlled. Thus, rather than the chaotic maelstrom of colliding molecules found in atmospheric conditions, reactions are examined under pristine conditions, simplified down to a single reactive species colliding with a clean surface with a known kinetic energy and angle so as to eliminate confounding factors. The characterization method is scanning tunneling microscopy (STM), a technique which affords spatial resolution spanning from the atomic level to multiple microns. Unlike other characterization techniques that average over large, macroscopic areas of the surface, STM is able to resolve single reacted surface atoms and nanoscopic topography. The principles of operation behind both STM and supersonic molecular beams will be explained in more detail later in this chapter. The unique construction of our instrument, which will be described in **Chapter 2**, for the first time allows the STM to examine a given nanoscopic area over time as it is exposed to monoenergetic gas molecules from the molecular beam. This yields never-before-accessible information on spatio-temporal correlations as a function of experimental conditions, allowing individual surface features to be monitored as the reaction progresses. This research thus represents a new approach to surface reaction dynamics, probing reaction barriers with energy-selected gas molecules and uncovering the mechanisms of the resulting reactions by tracking the evolving morphology and spatial distribution of surface features over time.

The first topic chosen upon the completion of our instrument fully demonstrates the potential of our new investigative approach. In **Chapter 3,** the site selectivity of primary and secondary oxidation reactions on the complex Si(111)-7×7 unit cell will be examined. The Si(111)-7×7 surface has served as a model semiconductor for decades, and its complex unit cell provides rich information on site selectivity and secondary reactions. With transistors approaching atomic dimensions it is essential to understand the initial oxidation process in detail, opening the way to more precise device fabrication. Room-temperature Si(111)-7×7 was exposed to 45 degree 0.4 eV $O_2$ with $\Delta E/E=0.28$ (an order of magnitude higher than 0.03 eV background oxygen), with the oxidation of specific surface atoms monitored by revisiting nanoscopic areas after each oxygen exposure. The ability to examine a given area before and after oxidation is especially important for this system, given the difficulty of distinguishing between oxidized sites and preexisting surface defects. Our results revealed two oxidation channels, leading to the formation of dark and bright reacted sites. This differing STM contrast results from the structure of oxidized sites, with bright sites corresponding to adatoms with O atoms inserted into the Si–Si backbond, and dark sites with oxygen adsorbing directly on top of adatoms, quenching the dangling bond.[1] The dark sites dominated the surface and exhibited almost no site selectivity while the bright sites showed only a slight preference for the corner sites of the 7×7 unit cell, in contrast to the strong selectivity previously seen with lower oxygen energies.[2] The bright sites are also highly reactive and saturate at ~4 % surface coverage. This aids the domination of dark sites which start to form clusters even at < 15 % coverage. Two adsorption pathways, trapping-mediated and direct chemisorption, are found to occur simultaneously even above the previously-reported threshold of 0.15 eV for the transition to direct chemisorption.[3]

**Chapter 4** examines the oxidation of highly oriented pyrolytic graphite (HOPG) under a variety of reaction conditions. HOPG is widely studied due to the importance of carbonic materials in applications such as high velocity flight systems as well as its key role as a model system for other carbonic materials such as graphene and carbon nanotubes, but the oxidation mechanism is not fully understood. Our precise control over reaction conditions allowed us to disentangle the effects of surface temperature, oxygen energy, and impingement angle, something not possible with the tube furnaces previously used. HOPG samples were heated to between 1275-1475 K and exposed to 0.4-0.7 eV $O_2$ impinging normal to the surface or 45 degrees from normal. The morphology of etch features differed greatly with different conditions, appearing as anisotropic channels, circular pits, and hexagonal pits. The faceted and circular etch pits were formed at low $O_2$ energy, with faceting only apparent below a critical surface temperature. This faceting can be attributed to the preferential reaction of armchair-type edge carbons, leaving only hexagonal pits with zig-zag edges aligned with the < 1 1 -2 0 > lattice directions.[4] Due to nearest-neighbor effects, armchair-type edge carbons are less stable and thus slightly favored for removal. Anisotropic etching was observed with exposure to higher energy oxygen. Comparison of low- and high-grade reacted samples show that anisotropic channels likely result from the presence of grain boundaries. Reaction probability increased with beam energy and demonstrated non-Arrhenius behavior with respect to surface temperature, likely due to the increased desorption of adsorbed O atoms at higher temperatures.[5] Further, lower energies and more glancing angles slowed the onset of etching, in agreement with calculations performed by our collaborators.[6]

Finally, **Chapter 5** presents an investigation of the oxidation of GaAs(110), a compound semiconductor with important applications in radiation-hardened electronics and solar cells, and as a model for other III-V compound semiconductors. Room-temperature GaAs(110) samples were exposed to $O_2$ with kinetic energies of 0.4-1.2 eV and normal or 45 degree impingement angles. Two competing mechanisms were observed, a homogeneous process with randomly distributed chemisorbed oxygen leading to layer-by-layer oxide growth, and a heterogeneous process with oxides nucleating on structural surface defects and growing vertically and laterally with continued exposure. Our instrument's unique capabilities have allowed us to revisit nanoscopic areas to monitor oxide island growth and to individually determine the kinetics of each mechanism. The mode of GaAs(110) oxidation is a source of some controversy, with previous studies using low energy oxygen finding either homogeneous[7] or heterogenous oxidation.[8] At higher oxygen energies, our results indicate that both mechanisms occur, with the heterogeneous mechanism kinetically favored. No oxidation was observed during the experimental time frame with oxygen kinetic energies below 0.7 eV; by contrast a nonlinear increase in the rate of oxidation from 1.0-1.2 eV was found with homogeneous and heterogeneous oxidation proceeding simultaneously until full surface coverage was reached. 1.0 eV oxygen, for instance, was 2-3 orders of magnitude more reactive than background-dosed oxygen[9] and precipitated the formation not only of monolayer oxide films but also elevated multilayer features, likely caused by "blistering" due to subsurface oxidation near structural surface defects.

## 1.1 Surface Structures

Silicon follows the diamond cubic crystal structure, shown in **Figure 1-1**, such that each silicon atom maintains tetrahedral bonding.[10] This structure is equivalent to two overlaid face-centered cubic lattices, with one lattice transposed diagonally by one quarter of the unit cell width. Many compound semiconductors, including gallium arsenide, follow the related zinc blende structure, which is identical to the diamond cubic lattice but with atoms of alternating species (in other words, each gallium atom is bonded to four arsenic atoms and each arsenic to four gallium atoms).

Si(111) is a surface created by cleaving the crystal diagonally across the unit cell, as shown by the dotted lines in **Figure 1-1**. This leaves a face normal to the Miller indices (111), or in other words, a plane which intercepts the unit cell corners one cell width from the origin in each direction. This truncation of the bulk crystal leaves an unstable surface with many dangling bonds. As a result, when the sample temperature is high enough surface atoms may rearrange into a more stable configuration, known as a surface reconstruction. The 7×7 reconstruction of Si(111) is particularly complex, with a unit cell width seven times that of the bulk-terminated surface in both lattice directions (thus it is defined as the '7×7' reconstruction). This reconstruction is described by the dimer-adatom-stacking fault model.[11] The unit cell features two subunits, offset vertically due to a stacking fault, that are bordered by dimers. The cell contains six rest atoms and twelve elevated adatoms. The adatoms are of particular interest, as they provide bonding sites for oxygen and can be imaged by STM, as will be discussed in **Chapter 3**. GaAs(110), meanwhile, has a substantially less complex 1×1 reconstruction with the topmost As atom raised and the Ga atom lowered, creating a tilt of about 27 degrees relative to the surface.[12,13] These manifest in STM imaging as rows running along the $[\bar{1}10]$ lattice direction.[14]

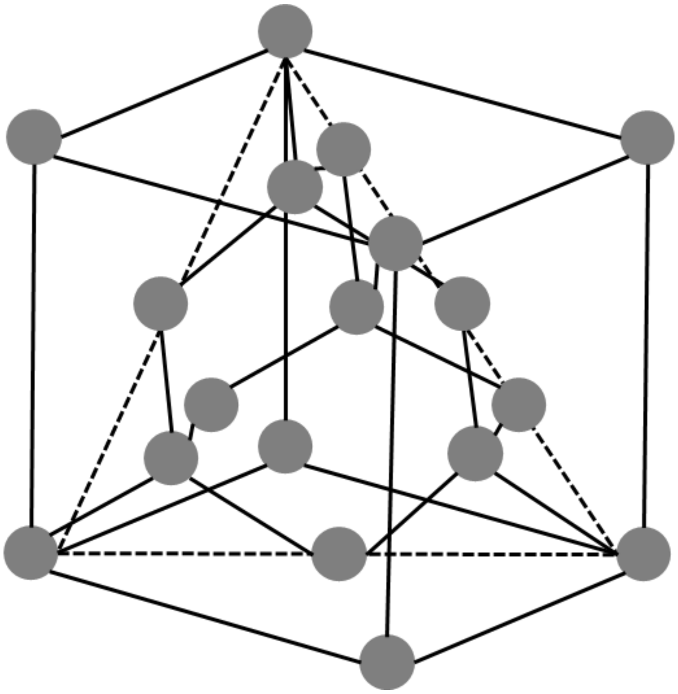

**Figure 1-1.** A diagram of the diamond cubic crystal unit cell. The (111) plane is defined by the dashed lines.

Graphite, which unlike silicon and gallium arsenide is a semimetal rather than a semiconductor, has a rather different structure. As opposed to the $sp^3$, tetrahedral bonding found in silicon and diamond, the bonding in graphite is $sp^2$ hybridized, with each carbon atom bonded to three neighbors. The covalently bonded carbon atoms form graphene sheets with a hexagonal, honeycomb lattice. The stacked graphene layers are bound by weak van der Waals interactions, and thus have a large inter-layer spacing of 335 pm, much larger than the bond length of 142 pm for carbon atoms in the graphene sheets.[15] Each graphene sheet is offset from the next such that only half of the carbon atoms, referred to as α atoms, are located directly above an atom in the subsequent layer while their neighbors, the β atoms, are located above hollow sites.[16] Only β atoms are imaged by STM, leading to images that resemble a hexagonal close packed lattice of β atoms separated by 246 pm, as will be shown in **Chapter 4**.

## 1.2 Scanning Tunneling Microscopy

The characterization tool used for all of the experiments presented in this thesis is scanning tunneling microscopy, or STM. This powerful technique was invented in 1982 by Binnig and Rohrer,[17] and has subsequently become one of the most-used methods for imaging conductive surfaces, such as metals, semimetals, and semiconductors, on an atomic scale. STM operates by placing a sharp metal tip in close proximity to the surface, and applying a voltage across the resulting gap. Although current flow across this gap is classically forbidden, electrons are able to tunnel through the barrier and establish a tunneling current. The tunneling current can be calculated by invoking the Wentzel-Kramers-Brillouin (WKB) approximation[18,19] as the potential can be assumed to vary slowly, giving the following expression:

$$I_t = \int_0^{eV} \rho_s(E)\rho_T(E - eV)\exp\left(-\left(\frac{2z\sqrt{2m}}{\hbar}\right)\sqrt{\frac{\phi_s + \phi_t}{2} + \frac{eV}{2} - E}\right)dE \qquad (1-1)$$

Where $I_t$ is the tunneling current, $V$ is the applied voltage, $\rho_s$ and $\rho_T$ are the density of states of the sample and tip, $z$ is the tip height, and $\phi_s$ and $\phi_t$ are the work functions of the sample and tip. From this equation it is evident that the tunneling current depends exponentially on the gap width. This is the key to the atomic resolution of the STM, as the gap width and therefore the current is affected by small changes in the topography of surface features. It is also apparent that the tunneling current depends on the density of surface states $\rho_s$, allowing the STM to perceive electronic states as well as topographical information. Thus, the images produced are a convolution of both of these and not purely a height map of the surface. When a negative bias voltage is applied to the sample, electrons tunnel from the occupied surface states to the tip, while at positive bias electrons tunnel from the tip into unoccupied states, as shown in **Figure 1-2.**

Because the surface states depend on the local chemical environment, the STM can be used to monitor reactions on the surface.

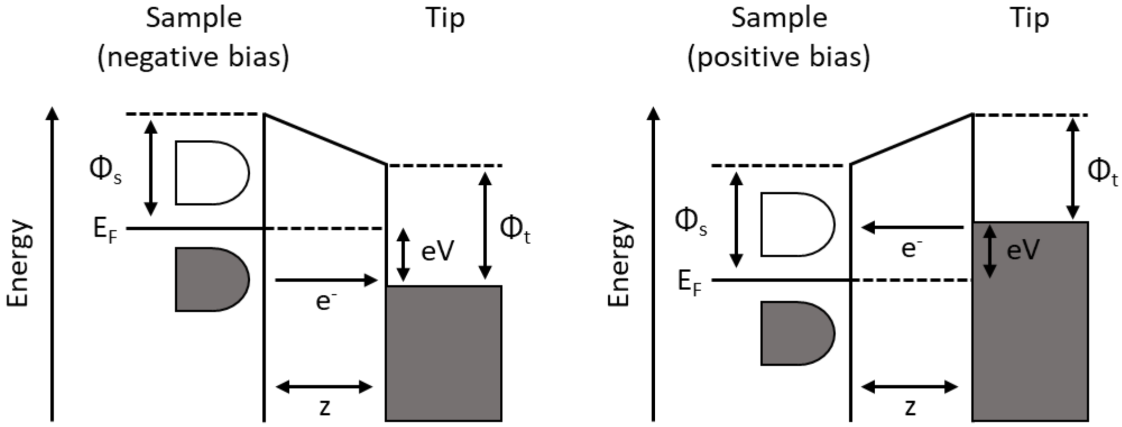

**Figure 1-2.** An electron band diagram of the STM tunneling junction, showing electrons tunneling from the occupied surface states into the tip when a negative bias is applied to the sample (left), and tunneling from the tip into the unoccupied surface states at positive bias (right).

During STM scanning, the tip follows a raster pattern over the surface while the tip height is controlled by a proportional-integral-derivative (PID) feedback loop. Scanning is typically performed in constant-current mode, wherein the feedback loop continuously adjusts the tip height to maintain the tunneling current at a setpoint defined by the user. The tip height therefore responds to changes in surface topography and local density of states, and is recorded at each point in the raster scan to generate the STM image. By changing the bias on the tip, the density of states at different energies can be probed to gain insight into the bonding environment of surface atoms and to distinguish between topography and electronic effects.

### 1.3 Supersonic Molecular Beams

A supersonic molecular beam consists of a jet of gas expanded through a nozzle from a high-pressure source into a vacuum.[20–23] A supersonic expansion occurs in the case that the nozzle aperture diameter is much larger than the mean free path of the source gas, such that molecules collide frequently and their random individual velocities converge on the bulk gas flow velocity. Put another way, the gas undergoes an isentropic expansion, meaning that the enthalpy of the randomly moving source gas is converted into translational kinetic energy in the direction of the jet. The internal temperature of the beam is cooled by this expansion, with vibrational and rotational energy largely converted into translational energy. The distribution of velocities in the beam narrows, with all molecules near the flow velocity and colliding only infrequently. This corresponds to a high Mach number, which is defined as follows:

$$M = \frac{u}{c} = u\sqrt{\frac{m}{\gamma k T}} \qquad (1-2)$$

where $M$ is the Mach number, $u$ is the flow velocity, $c$ is the speed of sound in the beam, $m$ is the mass, $\gamma$ is the heat capacity ratio, $k$ is the Boltzmann constant, and $T$ is the temperature in the beam. As the expansion occurs the flow velocity increases and the speed of sound, which for an ideal gas is proportional to the square root of beam temperature, decreases as the temperature in the beam drops. Once the expansion is complete, $M > 1$ and the beam has become supersonic.

# Chapter 2: Experimental Methods

## 2.1 Instrument Design

A novel ultra-high vacuum system, shown in **Figure 2-1**, equipped with a supersonic molecular beam and a custom scanning probe microscope with the surface plane normal to the beam (when the incident angle is set at 0˚ polar angle) was used for all experiments described in this thesis. This geometric arrangement allows us to perform real-time and real-space *in-situ* imaging. The configuration is such that the STM assembly can independently rotate 0˚ – 50˚ for polar-angle-dependent studies. The tip has the capability to move in XYZ directions to precisely and repeatedly access different areas of the sample and remove the tip from the beam's line of sight for dosing in order to avoid shadowing. The SMB beamline consists of three differentially

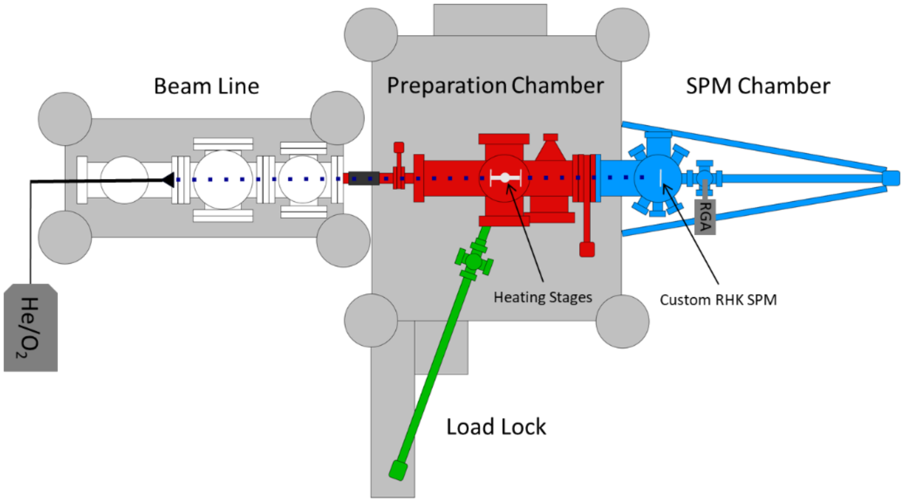

**Figure 2-1.** Diagram showing the combined supersonic molecular beam/materials preparation/SPM system.

pumped stages separated by a skimmer (first stage) and a collimating aperture (second stage). The third and final stage houses the final collimating aperture, which determines the 4 mm beam spot size at the sample when placed in the STM. The Beam Dynamics Model #2 skimmer has a 0.5 mm orifice, 1.0" length, and 25 degree included angle. It is placed about 8 mm from the beam nozzle. The beam nozzle aperture is 30 μm and both collimating apertures are 1 mm. The final collimating aperture is located about 70 cm downrange from the skimmer, and the sample is located about 64 cm from the final aperture when mounted on the prep chamber manipulator, and 158 cm from the aperture when mounted in the STM in the pan chamber. Two Oerlikon Leybold 600 L $s^{-1}$ magnetically suspended turbomolecular pumps evacuate the first and second stages of the beam line. These pumps are backed by a single Edwards nXDS15i dry scroll pump. A 100 L $s^{-1}$ ion pump is used to evacuate the third region of the beamline. The first, second, and third differential region working pressures with the beam on are ~$10^{-3}$, $10^{-6}$, and $10^{-9}$ Torr, respectively. The differentially pumped STM chamber, evacuated with a Gamma Vacuum 200L/s DC ion pump and a titanium sublimation pump, has a base pressure better than 5 x $10^{-11}$ Torr and remains in the low $10^{-10}$ Torr region during beam exposure. The SMB is connected to the sample preparation chamber by custom metal bellows and a mini conflat gate valve. The SMB and STM systems rest on separate air leg isolation tables with the bellows providing additional vibration decoupling as well as lateral movement for beam alignment. The presence of the SMB chambers does not produce electrical or mechanical noise in the STM data; therefore, the beamline can remain in full operation between sample exposures.

The preparation chamber is evacuated with a Perkin Elmer 220L/s DI ion pump and a titanium sublimation pump and has a base pressure better than 5 x $10^{-11}$ Torr. It can also be pumped out via the load lock, which is evacuated by a Balzers TMU65 55L/s turbomolecular drag pump and backed by a Varian SH-110 scroll pump. The preparation chamber contains a manipulator capable of rotation and translation in the X, Y, and Z directions equipped with two resistive sample heaters manufactured by RHK, with one mounted normal to the beam and the other oriented 45 degrees from normal. When exposing, samples on the resistive heaters are positioned 1.3 m from the beam nozzle, with a 2 mm diameter beam spot at the crystal. Samples on the manipulator can also be positioned in-line with a PHI 04-150 ion gun for sputtering.

## 2.2 Scanning Tunneling Microscope

The microscope is a custom-designed RHK PanScan LT SPM based on the design of Shuheng Pan.[24] Pictures of the microscope are shown in **Figure 2-2.** The sample and tip are maintained at the same temperature, ensuring stable operation. It has been constructed with the entire assembly mounted on springs and able to be rotated, and with the surface plane vertical such that the sample may be exposed to the beam while the tip is in contact. This unprecedented design allows samples to be imaged *in-situ* after each beam exposure, with the ability to revisit a given nanoscopic area and monitor the progress of oxidation. The microscope is capable of STM as well as AFM imaging using RHK qPlus sensors, although only STM imaging was used for the experiments described in this dissertation due to the resolution limits of AFM. The microscope is controlled by a low-noise RHK R9 SPM control system.

STM tips are prepared from 0.25 mm diameter $Pt_{0.8}Ir_{0.2}$ wire either by mechanical cutting or by electrochemical etching. The cutting method simply involves cutting the wire with Lindstrom wire cutters at a sharp angle while pulling away to create a rough point on the end of the tip. These tips do not look as macroscopically sharp as those produced by etching, but frequently perform well in practice as only microscopic sharpness is relevant to imaging quality. Etched tips are prepared by mounting $Pt_{0.8}Ir_{0.2}$ wire in an electrochemical cell with 2 M NaCl electrolyte and a nickel counter electrode. The wire is first cleaned by inserting about 5 mm into the solution and applying a 5 V, 60 Hz alternating current with a Variac transformer. The wire is then moved to an insertion depth of about 2 mm, and 35 V is applied to the cell until the wire has etched above the level of the electrolyte solution, breaking the circuit. The tip is then washed with deionized water, cut to length, dried with nitrogen, and mounted in a tip holder for insertion into the instrument.

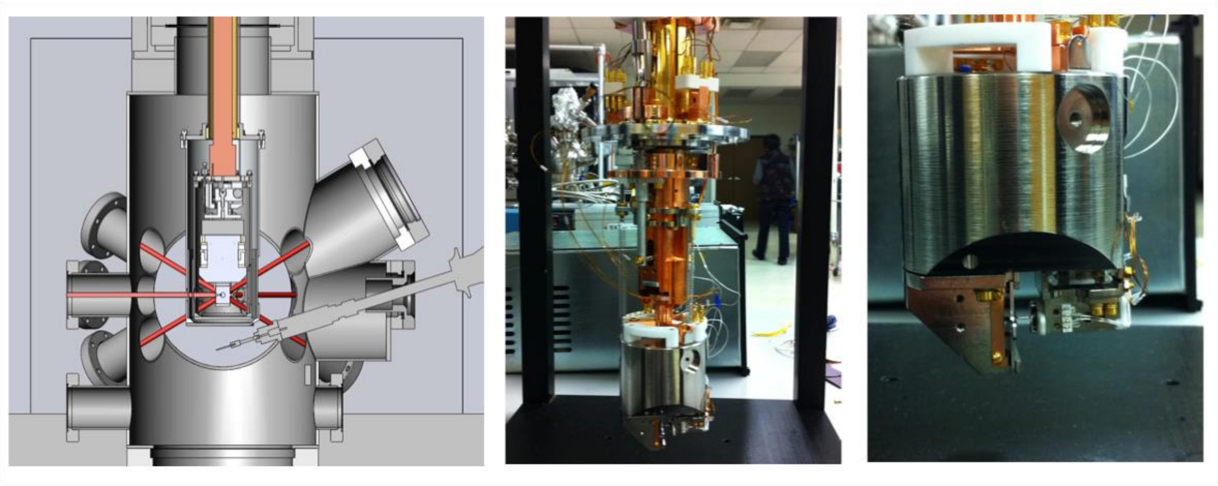

**Figure 2-2.** Pictures showing the custom RHK PanScan SPM. The SPM is mounted vertically with rotation capabilities so that the sample can face the beam at varying polar angles of incidence.

Samples and tips are inserted into the sample and tip stages of the microscope, and for experiments which involve revisiting a given nanoscopic area after beam exposure, the microscope is rotated 45 degrees to allow line of sight to the sample for the beam. Due to shadowing from the tip at this angle, simultaneous exposure and imaging is not possible and the tip must be moved several microns backwards or laterally to allow exposure, then returned to the area of interest. The tip is controlled by a four-quadrant piezo tube, with voltage placed across the tube along each axis to induce a shape change and move the tip. The scanner is diagramed in **Figure 2-3**, showing the

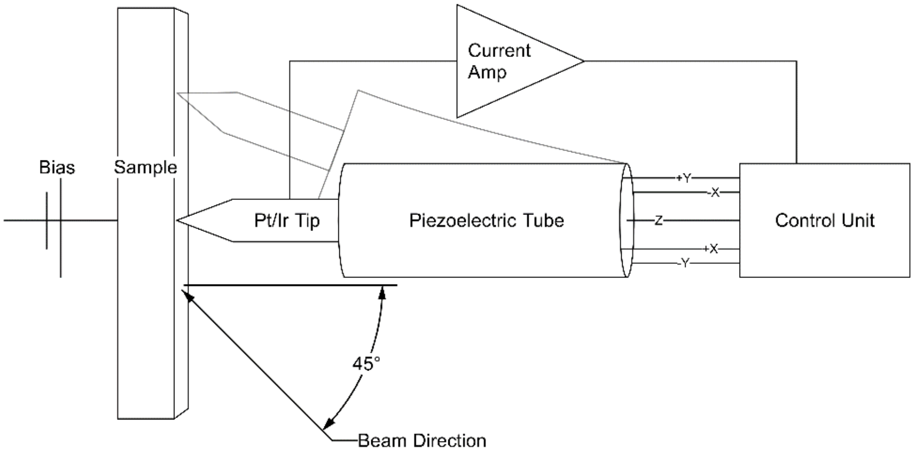

**Figure 2-3.** A diagram of the PanScan STM showing the piezoelectric tube that controls the movement of the tip in three dimensions, and the impingement direction of the beam which allows exposure of the sample while the tip is in contact. The tilt of the tip is exaggerated to illustrate its motion.

movement of the tip by the piezo tube as well as the impingement angle of the beam. The tip is manually course approached towards the sample, monitored by a camera, and then undergoes a software-controlled approach by stepping towards the sample until the setpoint tunneling current is detected. Once approached, the sample is scanned in constant current mode (as the alternative constant height mode risks crashing the tip into tall surface features). Constant current mode maintains the tunneling current at the setpoint value using a PID feedback loop by adjusting the tip height. The integral gain is adjusted during scanning so as to quickly respond to changes in surface topography at a given scanning speed. Excessive gain values cause ‘ringing’ in the line scan, due to the underdamped tip oscillating for some time after encountering a topography change, while insufficient gain values smear features as the overdamped tip responds too slowly. While scanning the integral gain is set between 50-1000 m/As, but is increased to between 3-4 km/As during approach to increase stepping speed. The feedback type is linear, and the tip control is set to unlimit. Typical bias values are between -3 and 3 V, and typical current set points are between -1 and 1 nA. The current filter cut off frequency is set to 1 kHz, and the current input has the offset DAC set to -13.3 pA with a gain value of 4. Configuration settings for the RHK PMC100 are given in **Table 2-1**.

| Direction | Amplitude | Sweep Time | Steps per Click | Time between Sweeps | Invert |
|---|---|---|---|---|---|
| +X | 220 V | 2.000 ms | 1 | 0.000 ms | ✓ |
| -X | 220 V | 2.000 ms | 1 | 0.000 ms | |
| +Y | 220 V | 1.000 ms | 1 | 0.000 ms | ✓ |
| -Y | 220 V | 1.000 ms | 1 | 0.000 ms | |
| Approach | 200 V | 1.000 ms | 1 | 0.000 ms | |
| Retract | 200 V | 1.000 ms | 1 | 0.000 ms | |

**Table 2-1:** The configuration settings for the RHK PMC100 piezo motor controller applied in the Rev9 software.

### 2.3 Image Processing

All STM images were processed in the open-source SPM data processing application Gwyddion.[25] In cases where the scanning resolution was high, images were simply flattened using plane subtraction and scan row alignment. In some instances when processing small (typically <200 nm) images with insufficient resolution, denoising was performed by combining the forward and reverse scan data in reciprocal space. As any true surface features should be present in both data sets, they will be preserved while random noise that is uncorrelated between the data sets will be suppressed. This procedure requires well-aligned forward and reverse topography images, so these are mutually cropped and one is temporarily subtracted from the other using the Multidata Arithmetic tool to check for consistency. The 2D Fast Fourier Transform (FFT) tool is then used to convert both scans into reciprocal space data sets in real and imaginary parts. The forward and reverse real FFT images and forward and reverse imaginary FFT images are combined using the

Multidata Arithmetic tool. **Equation 2-1** shows the expression most frequently used for this operation, although a variety of expressions may be implemented to achieve the desired level of noise suppression.

$$\left(1-\left(\frac{\mathrm{abs}(\mathrm{d1}-\mathrm{d2})}{\max(\mathrm{abs}(\mathrm{d1})+\mathrm{abs}(\mathrm{d2}),10^{-20})}\right)\right)\left(\frac{\mathrm{d1}+\mathrm{d2}}{2}\right) \qquad (2-1)$$

This expression scales the average of the data points from each FFT image (defined as d1 and d2) based on their relative difference, with points of opposite sign being eliminated entirely. The max() function in the denominator is used to avoid divide by zero errors.

Statistical data were generally extracted from STM images by masking grains in Gwyddion. Grains can be marked by threshold, watershed, or assigned manually. For instance, to determine the area of a surface feature, a mask is placed over the feature using the Threshold tool, and may be adjusted manually using the Edit Mask tool. Statistics are then generated from this grain, including its area in nm$^2$. To count features, small grains are manually placed over each feature and statistics are generated such as the number of grains and their x and y positions (from which information such as the distance to nearest neighbors can be calculated).

## 2.4 Sample Cleaning

The prep chamber is configured to allow sample cleaning by cycles of sputtering and annealing without the need to transfer the sample between stages. The manipulator can be equipped with a normal-angle resistive heater, a 45 degree-angle resistive heater, or up to two normal-angle electron beam heaters. Sputter/anneal procedures are provided here for an example semiconductor, GaAs(110), and an example metal, Ru(0001), but the exact procedure will depend on the sample being used. GaAs(110) is sputtered using the 45 degree-angle resistive heater, which is positioned at the manipulator coordinates x=4.5, y=5.0, z=8 $\frac{20}{32}$", and θ=100°, a position located by maximizing the drain current. The gate valve between the prep and load lock chambers must be opened and the prep chamber ion pump turned off before introducing argon, such that the prep chamber is pumped exclusively by the turbo pump in the load lock. A background pressure of $5\times10^{-5}$ torr of argon is reached by adjusting the Varian leak valve. An emission current of 20 mA is placed across the sputter gun filament, at which point a beam voltage of 1 kV is activated and sputtering commences with a drain current of ~3 μA measured from the heater to the ground. Typical sputter cycles last 30-90 min, after which the beam voltage and emission current are terminated, the leak valve closed, and the sample rotated until visible through the main prep chamber window (a manipulator angle of about 10°). For convenience, the ion pump is typically not turned on until the last heating cycle. A current of ~1.4 A is placed across the sample using an Electro Industries Model 4025 power supply, with the current adjusted to maintain a temperature of 430 C as measured by a Mikron infrared pyrometer (with the emissivity set to 0.69). Anneal cycles also typically last 30-90 min. The cleaning procedure for metal samples (in this example ruthenium) is similar, but the electron beam heater is used as the resistivity of the sample is too low to allow resistive heating. The heater is positioned at manipulator coordinates x=6.5, y=3.0, z=9 $\frac{2}{32}$", and θ=100°, and sputtered for about 30 min with an Ar pressure of $5\times10^{-7}$ torr, emission current of 10 mA, beam voltage of 500 V, and a measured drain current of about 7 nA. In this case the ion pump is turned on for heating cycles. The manipulator is again turned until the sample is visible, and a current of about 4 A is placed across the e-beam filament (0.25mm, W99/Th1) suing the Electro Industries power source. The sample is flashed several times to ~1200 C for 10-20 s by applying a bias of ~475 V between the heater sample mount and ground using a Sorensen Model XG 600-14 power supply. The sample temperature is monitored using the pyrometer with an emissivity of 0.35, and the prep chamber pressure is maintained below about $5\times10^{-6}$ torr during the flashes.

## 2.5 Venting and Bakeout

The system is vented by opening the gate valves between the load lock, prep, and pan, and turning off all pumps for those chambers (along with the ion gauges). Once the load lock turbo has spun down, the door on the load lock is unlatched and nitrogen is introduced through the valve on the load lock until atmospheric pressure is reached and the door can be easily opened. If necessary, the beam stages can be vented by turning off the turbo and ion pumps, then turning off the backing scroll pump and opening the first stage leak valve. After venting, the system is pumped down using the load lock turbo, with the prep and pan ion pumps off. The beam stages are pumped down by closing the leak valve and turning on the scroll and turbo pumps, followed by the ion pump when the pressure reaches about $10^{-6}$ torr. To achieve pressures better than the $10^{-9}$ torr range, it is necessary to bake out all chambers except for the beam stages. Before baking, all cables and equipment that are not heat stable are removed from the prep and pan chambers, including the STM and AFM connections, the pan chamber camera, and the cable to the prep chamber ion gauge. All glass windows are covered with aluminum foil, and the pan chamber and load lock are wrapped in heating tape and covered in foil to ensure even heating (the steel chamber walls have a low heat conductivity and do not redistribute heat effectively). The heating tape is plugged into Variac power supplies. The prep chamber is covered in a custom fiberglass heating tent with the edges and any gaps secured with duct tape, which is then heated with a TecTra Model SBHI 236V Standby Bakeout Heater. A thermocouple is inserted into the fiberglass tent to monitor the baking temperature, while the pan chamber temperature is monitored using the SPM cryostat thermocouple. The prep and pan ion pump heaters are plugged in, and the Variacs and the tent heater adjusted to achieve temperatures of about 110 C in both chambers, taking care not to exceed ~130 C in the pan chamber and risk damaging the SPM piezos. The system is maintained above 100 C for at least 48 hours, at which point all heaters are turned off and the ion pumps and ion gauges are turned back on. The TSPs in the prep and pan are run every 1-2 hours over the course of the day to further reduce the background pressure.

### 2.6 Beam Alignment and Flux Calculation

The beam stages can be aligned with the sample in the STM while the instrument is vented by using a telescope to ensure collinearity of the STM sample stage, 3rd stage aperture, and the skimmer. The RGA, sample, second stage aperture, and third stage aperture are first removed and the STM tip stage and prep chamber manipulator are elevated to allow line of sight from the pan chamber window to the skimmer. The telescope is focused on the center of the STM sample stage, then focused on the skimmer and adjusted using the tilt controls to center the skimmer. The telescope is then focused once again on the STM sample stage and adjusted using the x and y translation controls to center. This process is repeated until the telescope, STM sample stage, and skimmer are exactly colinear. The third stage aperture is reinstalled, and the beam table air legs are adjusted until the aperture is centered in the sight of the telescope. The second stage aperture is then reinstalled and should appear centered in the telescope, confirming that the beam is now correctly aimed at the center of the sample. When the system is returned to UHV, the beam nozzle can be aligned with the skimmer by maximizing the downrange flux of the beam. After the beam is allowed to equilibrate at the desired nozzle temperature, the x and y translation knobs for the beam source are adjusted while monitoring the RGA signal for the gas of interest or, if the flux is high enough, the pan chamber ion gauge reading. The pressure in the pan chamber is maximized by first adjusting one of either x or y, followed by the other axis of adjustment, continuing to alternate between the two until no further maximization is possible. This procedure must be repeated every time the beam nozzle temperature is altered. The beam flux can be calculated using either the RGA signal or the ion gauge reading, adjusted for the sensitivity of the ion gauge to the gas in question. The beam flux is approximated by equating the rate of gas entry into the pan chamber to the rate of gas removal by the pan ion pump:

$$\phi_{in}A_{spot} = \frac{N_{out}}{t} \qquad 2-2$$

for beam flux $\phi_{in}$, spot size $A_{spot}$, and molecules $N_{out}$ removed per time interval $t$. Assuming an ideal gas:

$$\phi_{in}A_{spot} = \frac{V_{out}\Delta P}{tkT} \qquad 2-3$$

for volume of gas removed $V_{out}$ and change in pressure with the beam on as compared to the base pressure $\Delta P$. Substituting in the pumping speed $S = \frac{V_{out}}{t}$ and rearranging:

$$\phi_{in} = \frac{S\Delta P}{kTA_{spot}} \qquad 2-4$$

This equation was used to approximate the flux for all experiments presented in the following chapters, with $\Delta P$ kept constant for each exposure so as to ensure constant flux conditions.

# Chapter 3: Temporally and Spatially Resolved Oxidation of Si(111)-(7×7) using Kinetic Energy Controlled Supersonic Beams in Combination with Scanning Tunneling Microscopy

## Summary

The site-specific locations of molecular oxygen reactivity on Si(111)-(7×7) surfaces were examined using kinetic energy selected supersonic molecular beams in conjunction with *in situ* scanning tunneling microscopy. We herein present a detailed visualization of the surface as it reacts in real-time and real-space when exposed to molecular oxygen with translational energy $E_i$=0.37 eV. Atomically-resolved images reveal two channels for oxidation leading to the formation of dark and bright reaction sites. The darks sites dominate the reaction throughout the range of exposures sampled and exhibit almost no preference for occurrence at the corner or inner adatom sites of the reconstructed (7x7) unit cell. The bright sites show a small preference for corner vs. inner site reactivity on the reconstructed (7x7) unit cell. The bright site corner preference seen here at elevated kinetic energies and with selected incident kinematics is smaller than that typically observed for more conventional thermal (background dosed) oxidation processing. These observations suggest that two adsorption pathways, trapping-mediated chemisorption and direct chemisorption, occur simultaneously when using energetic molecular oxygen but with modified relative probability as compared with thermal dosing. These results demonstrate the efficacy of using angle- and energy-selected supersonic molecular beams to gain a topographical diagram of the accessible reactive potential surface energy and precise control of semiconductor oxidation, a process that is of growing importance as we seek to create high-quality and precisely-defined oxides having atomic dimensions.

## 3.1 Introduction

The oxidation of silicon surfaces has received considerable attention over the past four decades, serving as a general model for semiconductor oxidation.[26–28] As devices continue to decrease in size and approach atomic dimensions, the challenge of producing thinner, homogeneous, and perfected oxide layers increases. Current metal oxide semiconductor field-effect transistors (MOS-FETs) utilize oxide layers approximately four atoms thick, and further improvements using existing methods have been evolving slowly. In order to gain more refined control over oxidation and to produce defect-free oxide monolayers, it is essential to understand the initial oxidation process at subnanometer dimensions with atomic resolution. FETs with 3D structures, such as fin-FETs, are one illustrative candidate for future devices; several studies have examined fin-FETs with gate oxides on Si(111) fin sidewalls.[29,30] It is therefore valuable to understand the mechanism of oxygen adsorption not only on Si(100), but also on other crystallographic planes as well. The complex Si(111)-(7×7) interface, due to the presence of several different inherent atomic sites within the reconstructed unit cell, presents a unique opportunity to examine complex oxidation processes on semiconductor surfaces.[31,32]

Numerous studies of oxygen adsorption on silicon have been conducted experimentally[33–36] and theoretically.[37–41] In particular, several groups have investigated silicon oxidation using scanning tunneling microscopy (STM).[42–45] These studies found that the adsorption of thermal $O_2$ on Si(111)-(7×7) produced bright and dark reaction sites at adatoms, with the oxide coverage increasing with oxygen exposure. It was determined that the bright sites are so-called *ins* × *n (n= 1 – 3)* structures with oxygen atoms inserted into the Si–Si backbond.[42,45,46] The *ins* × *n* configuration elevates the Si adatom relative to the surface plane, causing a bright contrast in the STM image.[42] The dark sites consist of so-called *ad-ins* × *n* structures with oxygen adsorbed directly on top of a previously reacted *ins* × *n* site; these are therefore products of a subsequent reaction that occurs under thermal conditions. The adsorption of oxygen on top of an adatom suppresses its dangling bond so that it appears as a dark contrast depression in STM images.[31] Furthermore, recent photoelectron studies suggest *ins* structures are the initial product of oxygen adsorption on Si(111)-(7×7).[47] First principle calculations using a complete (7×7) unit cell have determined that chemisorbed molecular oxygen dissociates spontaneously upon adsorption without an activation barrier, creating *ins* × *n* primary products followed by *ad-ins* × *n* secondary products.[37] Throughout this chapter we will interpret bright and dark sites as *ins* × *n* and *ad-ins* × *n* configurations, respectively. **Figure 3-1** shows several possible *ins* and *ad* configurations.

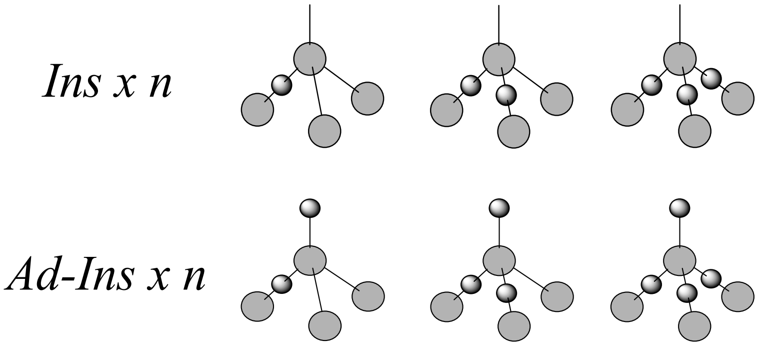

**Figure 3-1.** Ball and stick models of different oxygen adsorption configurations. Large circles represent Si atoms and small circles represent oxygen atoms; n is the number of oxygen inserted into the Si-Si bonds.

Supersonic molecular beams (SMBs) present an incisive tool for studying energetic site specific reactivity[48–51] on surfaces including oxygen[52–55]. Nolan and coworkers[56,57] report two types of molecular oxygen adsorption processes on Pt(111) depending on the incident translational energy ($E_i$). They utilized *in situ* high-resolution electron energy loss spectroscopy (HREELS) with SMBs to determine whether molecular oxygen experiences superoxo-like or peroxo-like precursor states prior to dissociating on the surface. High-kinetic-energy oxygen over the 0.2 to

1.37 eV range chemisorbs initially as a peroxo-like molecular species. On the other hand, at 0.055 eV they observed a high population of both superoxo-like and peroxo-like adsorbed oxygen. As with metal surfaces, the incident translational energy also plays a role in molecular oxygen adsorption on Si(111)-(7×7).[58–60] Yan *et al.*[58] performed an energy-dependent study with incident energies ranging from 0.02 to 0.25 eV. They observed no energy dependence for the formation of dark sites and found that bright site selectivity increases as a function $E_i$, with corner sites becoming more favorable at higher energies. They suggested two different molecular precursors resulting in the different oxygen-silicon configurations and attributed the kinetic energy dependence of bright site creation to the presence of multiple adsorption pathways: precursor-mediated chemisorption and direct activated chemisorption. Our current study builds on their early results with the additional capability of monitoring the exact scanning region over multiple oxygen exposures, i.e., with time resolution for visualization of the ongoing oxidation mechanism(s). Similarly, Yoshige and Teraoka[59,60] also report trapping-mediated chemisorption and direct chemisorption adsorption pathways for $O_2$ adsorption on Si(111)-(7×7). They monitored the change in photoelectron spectroscopy peaks while exposing the surface either to thermal (i.e., background dosed) or SMB molecular oxygen. The trapping state occurred for thermal $O_2$ adsorption, which has an average molecular kinetic energy defined by the most probable speed in the Maxwell Boltzmann distribution of ~0.03 eV, and also for SMB energies less than 0.06 eV. They suggest a mixture of mediated and direct chemisorption for energies ranging from 0.06 to 0.15 eV; however, at 0.39 eV only direct chemisorption was found.

The experimental findings with oxidation *via* supersonic oxygen beams clearly demonstrate that incident translational energy plays a role in the oxidation mechanism on the surface. SMBs are traditionally paired with non-local spectroscopy techniques (such as Auger, XPS, or HREELS) or configured in a way such that observing local chemical dynamics is not possible, thus obscuring the time-dependent atomic and nanoscale effects of energy and angle variation in the overall reaction mechanism. Therefore, we have constructed a new instrument that can provide time dependent and spatial resolution of interfacial reactivity as a function of translational kinetic energy with specified incident kinematic conditions.

In this study, we report a visual mapping of Si(111)-(7×7) oxidation at room temperature in real-space and real-time utilizing supersonic molecular beams with *in situ* scanning tunneling microscopy. High-resolution imaging reveals distinct adsorption chemistry for SMB $O_2$ in comparison with thermally-dosed $O_2$. In addition, our studies provide insight into atomically-resolved site-specific oxidation of a specific location for various exposure levels over time. This combination of techniques allows us to study oxygen adsorption as a function of kinetic energy in an unprecedented fashion.

### 3.2 Experimental

N-type Si(111) substrates (0.001 – 0.006 Ω-cm) were used in this experiment. The samples were degassed at 700°C overnight, followed by flashing to ~1200°C while maintaining a pressure of $\leq 7.5 \times 10^{-10}$ Torr. The surface temperature was monitored by a Mikiron infrared pyrometer and heated by applying current directly through the sample. Several areas on the surface were checked for cleanliness and (7×7) reconstruction by STM prior to oxygen exposure. Etched $Pt_{0.8}Ir_{0.2}$ tips were used for imaging.

Supersonic beams of molecular oxygen (SMB-$O_2$) were generated by expanding a 5% $O_2$ / 95% He mixture through a 30 μm diameter molybdenum pinhole at 15 psi. A translational kinetic energy of 0.37 eV with an energy distribution width of $\Delta E/E=0.28$ was found using time of flight measurements. **Equation 3-1** was used to calculate a flux of ca. $10^{11}$ molecules $cm^{-2}$ $s^{-1}$, as described in **Chapter 2**. Here S is the pumping speed, ΔP is the change of pressure between beam on and off, and $A_{spot}$ is the cross-sectional area of the beam at the sample. A residual gas analyzer was used to monitor the change in pressure in the STM chamber. An incident angle of 45° relative to the sample normal was used for all SMB exposures.

$$\phi = \frac{S\Delta P}{kTA_{spot}} \qquad (3-1)$$

### 3.3 Results and Discussion

**Figure 3-2** shows high resolution constant current STM images of the occupied and unoccupied states of Si(111)-(7×7). The images adhere to Takayanagi's[11] dimer-adatom-stacking fault (DAS) model with the *faulted* (bright triangular region of the STM unit cell image) and *unfaulted* (dark triangular region of the STM unit cell image) subunits clearly visible when using negative scanning bias. The reconstructed unit cell contains 12 adatoms that provide direct bonding sites for oxygen molecules. The 12 adatoms can be divided into six corner and six inner

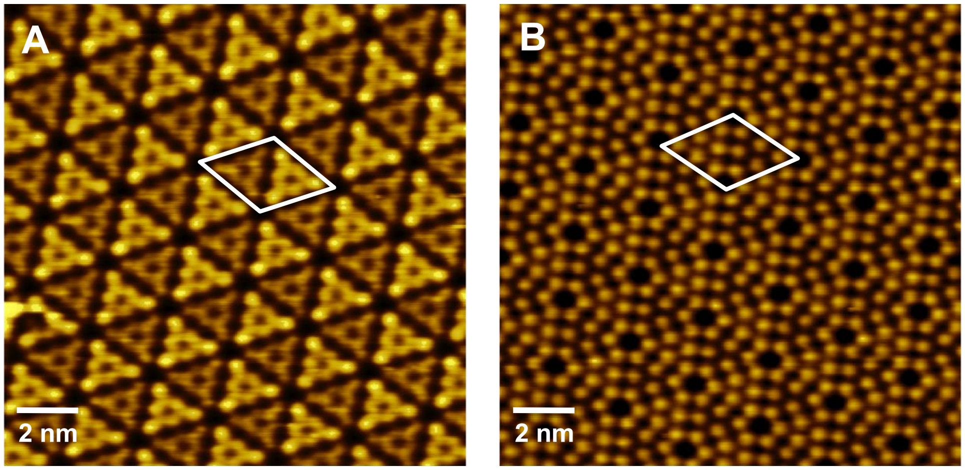

**Figure 3-2.** STM images showing **A)** occupied (-1.3 V 200 pA) and **B)** unoccupied states (2 V 200 pA) of a Si(111)-(7×7) surface; white overlay indicates the unit cell.

adatoms; the corner adatoms are adjacent to corner holes that create a distinct local electronic environment compared to the inner adatoms. Our results agree with the trend of the initial oxidation reactivity showing preference for the faulted side of the unit cell.[61] The corner and inner preference will be discussed in greater detail below.

In order to obtain accurate statistical information of the surface at various stages of oxidation, oxidation sites were surveyed over scan areas roughly 50×50 nm in size. These images consisted of approximately 3500 to 4000 available adatoms, with typically less than 2% defect concentration prior to oxygen exposure. The tip was retracted during each exposure and subsequently brought back to the same location to examine the surface after reaction. The data were collected either as a series of sequential images of an identical area (reacquired using surface defects or prior oxidation sites for absolute positioning) or statistically using nearby regions located microns apart. The surface reactivity shows good reproducibility within the expected statistics over multiple exposures. **Figure 3-3** shows three images in the same scan area, after three different SMB-$O_2$ exposures. High-resolution STM images revealed both dark (D) and bright (B) sites dispersed heterogeneously across the surface after exposure to SMB-$O_2$. Previous studies of thermal oxidation *via* background gas dosing show bright and dark sites have approximately a 1:1 concentration ratio at low exposures (< 0.6 L); only after additional oxidation do the dark sites start to dominate.[40] The surface becomes disordered and the (7×7) reconstruction is lifted at high oxygen exposures.[26,61] In contrast to the background gas dosing outcome, we found a predominance of dark sites throughout the SMB-$O_2$ oxidation process including at initial low exposures. However, the bright sites show some resemblance to outcomes observed using background gas dosing. Recently, Onoda *et al*.[62] addressed the question of what happens to the atomic oxygen after the molecular species dissociate on Si(111)-(7×7) at room temperature by

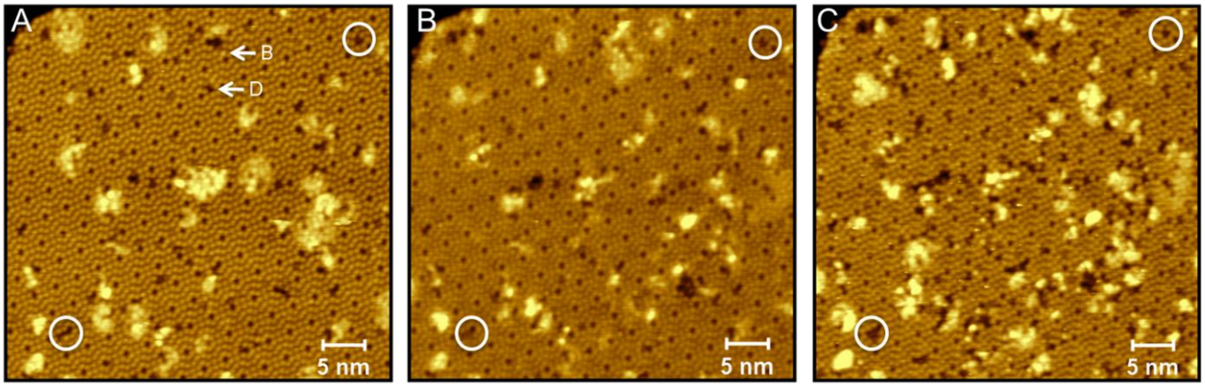

Exposure: 5.9 ×$10^{13}$ molecules•cm$^{-2}$

Exposure: 8.8 ×$10^{13}$ molecules•cm$^{-2}$

Exposure: 11.7 ×$10^{13}$ molecules•cm$^{-2}$

**Figure 3-3.** STM images in the same scan area after multiple SMB-$O_2$ exposures. Circles are used as reference points. The images display bright (*ins*) and dark (*ad*) features distributed heterogeneously across the surface. The *ad* structures dominate the adsorption type even at low surface coverage. All images were recorded at 2 V and 200 pA.

utilizing scanning probe microscopy and density functional theory calculations. Their AFM images show bright sites that were either in pairs on adjacent Si adatoms or isolated single sites without another bright site in the immediate surroundings. They identified the bright sites in pairs as two adjacent *ins* × *1* structures, with one O atom inserted in a Si adatom's back-bond, whereas single bright sites were ascribed to *ins* × *2* configurations, with two O atoms inserted into the backbonds of one Si adatom (see **Figure 3-1**). The experiments also illustrated the conversion of bright sites to dark sites after additional oxidation with the addition of an O atom on the top site of a previously reacted adatom. Our SMB results are in agreement with the dominance of single over paired bright sites found in their thermally-dosed experiment. However, **Figure 3-4** displays sequential images in the same location that exhibit a single bright site becoming paired after further oxidation, implying that some of the pairs may actually be two *ins* × *2* sites adjacent to one another. **Figure 3-4** also highlights a bright site converting into a dark site after additional oxygen exposure. This follows the conventional oxidation scheme of an *ins* × *n* site undergoing a secondary oxidation reaction and becoming an *ad-ins* × *n* site. These results show that the initial oxidation process can be complex and reveal new insight that was not previously available without the ability to obtain atomic resolution of the same location over multiple SMB-$O_2$ exposures.

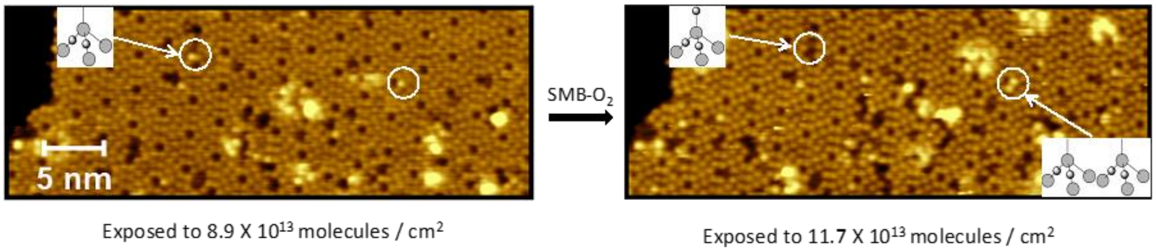

Exposed to 8.9 X $10^{13}$ molecules / $cm^2$

Exposed to 11.7 X $10^{13}$ molecules / $cm^2$

**Figure 3-4.** STM images of atomic level oxidation at two sequential exposure times, t = 3 min and t = 4 min. Circles indicate areas of change, e.g., a bright site converting to dark after additional SMB-$O_2$ exposure, and an area where a single bright site changed into a pair of adjacent bright sites. Images were taken at 2 V and 230 pA.

Atomic resolution images allow us to discern spatial, site-specific information for the reacted Si adatoms. A model (7×7) lattice was used to manually determine the number of adatoms and/or reacted sites present in each image. Only areas that show clear Si adatoms or reacted sites were used in the calculations to plot the graph. Previous defects prior to oxygen exposure and tip artifacts (bright clouds) were discarded in the total number of available sites. The graph in **Figure 3-5a** shows that the overall reactivity follows a linear trend. An initial sticking probability of ~0.1 was determined using the calculated flux of the impinging molecules, the change in defect coverage, and the surface density of available adatoms.

**Figure 3-5b** shows the coverage of bright or dark sites relative to the overall number of available sites. As mentioned above, previous thermal oxidation experiments report a roughly equal number of bright and dark sites on the surface for the early stages of oxidation. Interestingly, at similar exposures by SMB-$O_2$, dark sites dominate the adsorption process. This is a notable finding as the oxygen-silicon configuration during the early oxidation stages is altered by the use of SMB exposure. Congruent with the overall reactivity, the dark site coverage increases linearly

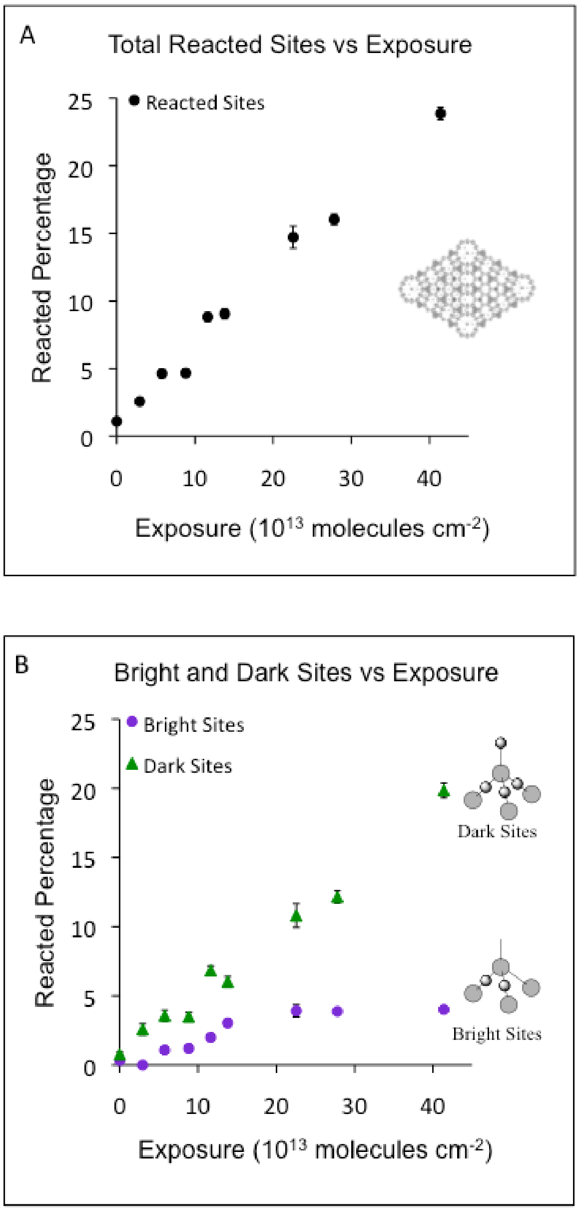

**Figure 3-5. A)** Reactivity vs. time for the entire surface. **B)** Decomposition of the overall reactivity into the percentage of dark and bright structures found on the surface vs. time. Note that bright and dark sites correspond to various ins × n and ad-ins × n structures, respectively, where n = 1, 2 or 3. Each point represents an STM image that contained approximately 4000 possible reaction sites. Some of the points represent statistics garnered from combining the results from multiple images. Error bars generated by sample size counting statistics.

as function of oxygen exposure. On the other hand, the bright site coverage remains ~4 % throughout multiple exposures, which is a lower steady state point than the 10 % previously found by thermal studies.[63] **Figure 3-6** shows a large scan area of the surface with ~14 % of the available adatoms reacted after SMB-$O_2$ exposure. The dark sites have increased significantly in number and started to form islands (i.e., groups or clusters of reacted sites), whereas bright sites are still dispersed across the surface and occupy a low percentage of the surface. Based on sequential images showing the creation and subsequent conversion of bright sites, we estimate the probability for the primary reaction of an unreacted adatom with a given $O_2$ molecule is ~0.05, which is similar to that for thermal oxidation.[63,64] On the other hand, the secondary reaction probability of a bright site is higher (up to twice as reactive) when exposed to energetic and 45 degree incident polar angle SMB-$O_2$ as opposed to the probability found for thermal background dosed oxygen.[63,64] The

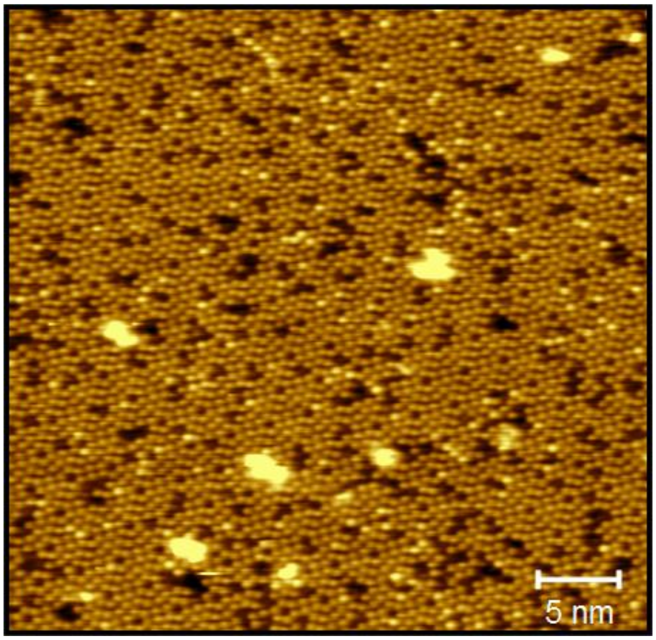

**Figure 3-6.** Large scale image after $2.8 \times 10^{14}$ molecules / $cm^2$ SMB-$O_2$ exposure. The dark sites are beginning to form regions of adjacently reacted sites, referred to as clusters or islands of reacted areas, whereas the majority of bright sites remain isolated and are therefore not in contact with another bright site. Set point: 1.8 V, 250 pA.

increased probability of secondary reaction for bright sites converting to dark sites accounts for the low concentration of bright sites and cluster formation of dark sites after multiple oxidation exposures as discussed previously in **Figure 3-5**.

We have also examined the site selectivity of bright and dark structures for corner and inner adatoms. In general, very little difference is seen. Upon close examination of bright site formation, we find a small preference for corner reactivity vs. inner sites. The dark sites show very little preference, with perhaps a slight bias towards inner site reactivity, as shown in **Figure 3-7**. We note that oxidation using energetic molecular oxygen does indeed differ from thermal processing with background gas dosing, with the bright sites created *via* SMB exhibiting a lower preference of ~1.2:1 for corner sites, as compared to 2.0 – 4.0 as previously cited for thermal $O_2$.[43,65,66] The dark sites overall exhibit a ~1:1 site selectivity, and in fact dark sites without an observed bright intermediate prefer inner adatoms. This indicates that dark sites are also produced by a process other than the conversion of bright sites, leading to different site selectivity. Thus, the conversion of bright sites upon further local reaction together with the direct formation of dark sites leads to the formation of islands (clustered regions) of dark sites. For thermal $O_2$, where trapping-mediated chemisorption dominates the adsorption process, the initial oxidation readily occurs at the corner sites, likely due to the corner adatoms' strain energy associated with their unique environment within the (7x7) unit cell.[43] The observed lower selectivity when using translationally fast $O_2$ is consistent with a higher overall probability for direct chemisorption occurring across the unit cell,[59] that is, more regions of the operative potential energy surface become accessible to $O_2$ reactivity due to the higher energy of the incident molecular ensemble. According to the potential energy surface diagram for the $O_2$ adsorption on Si(111)-(7×7) found in Ref 35, there are barriers of 0.6 eV and 0.39 eV. At energies $\leq$ 0.6 eV the molecules can enter a trapping state and diffuse

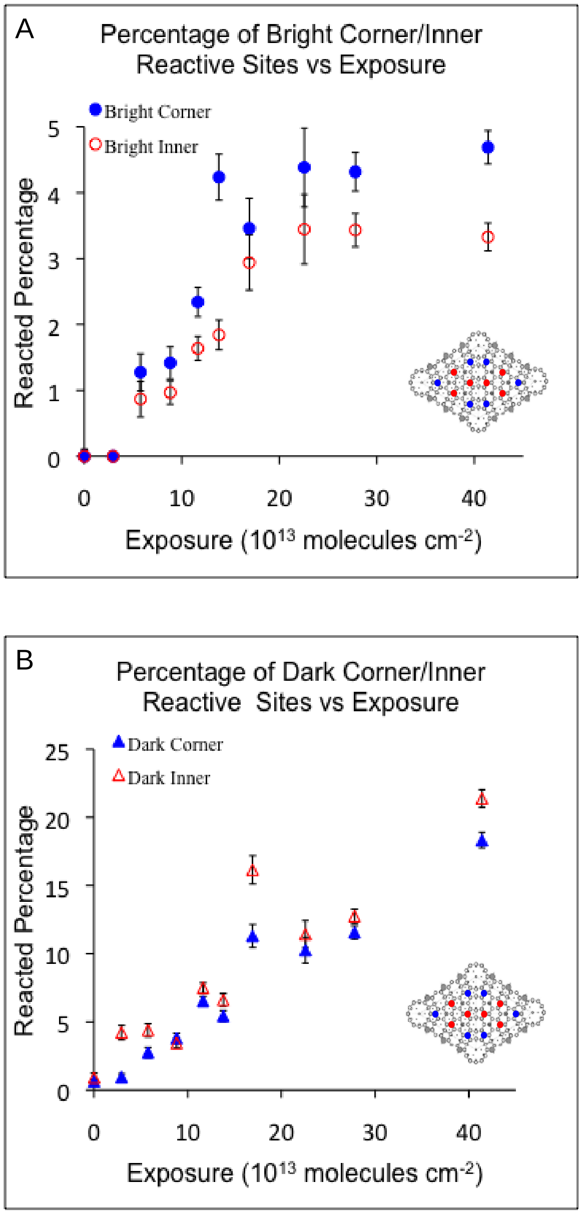

**Figure 3-7. A)** Reactivity at corner and inner adatom sites for bright site formation. **B)** Reactivity at corner and inner adatom sites for dark site formation. Corner and inner adatom symbols are filled and unfilled, respectively. The uncertainties are standard errors determined by sample size counting statistics. Insert shows a schematic of the Si(111)-(7×7) dimer-adatom-stacking fault model with corner (blue) and inner (red) adatoms highlighted.

across the surface to the preferred dissociate site (corner site). At our elevated translational energy of 0.37 eV, the molecules have enough energy to overcome the first barrier and reach the next region where $O_2$ more readily dissociates without diffusing on the surface. This increases the probability of reacting at the initial adsorption site, which has a 1:1 probability of occurring at a corner or inner site.

### 3.4 Conclusions

The site-specific locations of molecular oxygen reactivity on Si(111)-(7×7) surfaces were examined using kinetic-energy-selected supersonic molecular beams of molecular oxygen in conjunction with *in situ* scanning tunneling microscopy. We presented a detailed visualization of the surface as it reacts in real-time and real-space when exposed to molecular oxygen with translational energy $E_i$=0.37 eV. Atomically-resolved STM images reveal two channels for oxidation leading to the formation of dark and bright reaction sites. Sequential images show the overall reactivity increases linearly with respect to oxygen exposure. In contrast to thermal oxidation, the darks sites dominate the reaction throughout the range of exposures sampled, but exhibit no statistical preference for corner or inner adatom sites of the reconstructed (7x7) unit cell. The bright sites show a small preference for corner vs. inner site reactivity on the reconstructed (7×7) unit cell. The bright site corner preference seen here at elevated kinetic energies and with selected incident kinematics is smaller than that typically observed for more conventional thermal (background dosed) oxidation processing. Under the reaction conditions used in this study the bright sites have a population that reaches a steady state at about 4% of surface coverage. The increased probability of secondary reaction for bright sites converting to dark sites accounts for the low concentration of bright sites and cluster formation of dark sites after multiple oxidation exposures. These observations suggest that two adsorption pathways, trapping-mediated chemisorption and direct chemisorption, occur simultaneously when using energetic molecular oxygen but with modified relative probability as compared with thermal dosing. These results demonstrate the efficacy of using angle- and energy-selected supersonic molecular beams to gain a topographical diagram of the accessible reactive potential surface energy and precise control of semiconductor oxidation. Such precise control over interface oxidation is important, and will contribute to the development of more efficacious processing for the creation of high-quality and precisely defined oxides that are on the order of atomic dimensions.

# Chapter 4: Atomically-Resolved Oxidative Erosion and Ablation of Basal Plane HOPG Graphite Using Supersonic Beams of $O_2$ with Scanning Tunneling Microscopy Visualization

## Summary

The detailed mechanism and kinetics for the oxidative erosion and ablation of highly oriented pyrolytic graphite (HOPG) with molecular oxygen has been examined by monitoring the spatio-temporal evolution of the reacting interface. This has been accomplished using a new, unique gas-surface scattering instrument that combines a supersonic molecular beam with a scanning tunneling microscope (STM) in ultra-high vacuum. Using this new instrument, we are able to tightly control the energy, angle, and flux of impinging oxygen along with the surface temperature and examine the reacted surface spanning atomic, nano, and mesocopic length-scales. We observe that different oxidation conditions produce morphologically distinct etching features: Anisotropic channels, circular pits, and hexagonal pits faceted along crystallographic directions. These outcomes depend upon independent effects of oxygen energy, incident angle, and surface temperature. Reaction probability increased with beam energy and demonstrated non-Arrhenius behavior with respect to surface temperature, peaking at around 1375 K. At the incident collision energies used, it was found that beam impingement angle had only minor effects on the reaction probability and etch pit morphology. Comparison of the relative reactivity of higher grade versus lower grade HOPG indicates that the formation of etched channels largely depends on the presence of grain boundaries. We have also observed the transition to multilayer etching. The influence of structural inhomogeneities such as defects and grain boundaries can now be assessed by real-time visualization of reacting interfaces. For example, the insertion of intentionally created point defects *via* ion sputtering leads to marked enhancement in interfacial reactivity. The approach used herein

has allowed us to correlate time-evolving surface morphology with atomic-level interfacial kinetics and dynamics, providing new insight into the reactivity of materials in aggressive, energetic environments.

## 4.1 Introduction

Graphite oxidation is widely studied due to its relevance to technological applications such as high-performance aircraft and propulsion systems and due to its important role as a model system for fundamental studies of materials degradation. The oxidation process with molecular oxygen removes carbon from the surface as the products CO and $CO_2$, with CO being the dominant reaction product at all surface temperatures[67–70] and impinging oxygen energies.[71–73] Oxygen molecules dissociatively adsorb and diffuse across the surface[74] as adsorbed O before reacting with and removing carbon atoms from the surface. The prismatic plane of HOPG is oxidized much more rapidly than the basal plane, leading to the domination of lateral etching of graphite layers starting from vacancy defects and step edges.[75–79]

This work presents a new approach to studying the dynamics and kinetics of interfacial erosion chemistry where we monitor reactivity not by monitoring CO or $CO_2$ product formation but rather by visualization of the reacting interface using the combination of supersonic beam scattering coupled with ultra-high vacuum scanning tunneling microscopy (STM). This novel approach allows us to directly link the time-evolving morphology of the reacting interface with the observed reaction kinetics, in essence, giving access to the spatio-temporal correlations that govern time-evolving interfacial reactivity. In this instance, visualization encompasses several length-scales including atomic, nano, and mesoscopic distances. The ability to conduct such information-rich experiments was demonstrated for the site-specific energetic oxidation of Si(111)-(7×7).[80]

Such spatio-temporal measurements of surface morphological change and surface chemical change directly reveal the key roles that minority structures such as grain boundaries and defects play in determining the time evolution of the interface. This statement, in a broader sense, is especially relevant for intrinsically heterogeneous materials such as functional composites. In this study we intentionally introduce localized defects using ion sputtering, creating single or multi-atom vacancies visible to STM as positive contrast hillocks. These vacancies expose prismatic edge carbons and provide nucleation points for oxidation.[81,82] After a certain induction period, or nucleation phase, the removal of edge carbons results in a visible, negative contrast pit. By providing artificial nucleation points *via* sputtering, the density of etch features is substantially and controllably increased.

Previous research has used STM to examine graphite samples etched in furnaces under a high flux of heated molecular oxygen.[75–78,83–88] Circular, monolayer-deep pits were found to arise from these conditions, nucleating exclusively at natural and artificial defects at low temperatures (<1150 K) but nucleating even on the locally perfect (undefected) basal plane at higher temperatures (>1150 K).[78] In some cases elongated, anisotropic channels were observed on furnace-oxidized graphite, but formed a small minority of features with circular pits dominating.[78,82,89] Pit diameters were found to increase linearly with oxygen exposure, with the lateral etch rate increasing with temperature. The linear growth of pit diameters comports with an overall carbon reaction rate limited by the available density of reactive edge carbons.

At very high temperatures (>1275 K) the overall rate of carbon removal from the surface exhibits apparent non-Arrhenius temperature dependence as a result of the interaction of a number of competing reaction rates. Supersonic beam experiments have determined that reactivity peaks at 1400 – 1500 K, likely due to the increased desorption of adsorbed O atoms at higher temperatures.[71,90,5,91] An excess of adsorbed O enhances both the formation of new surface vacancies and the etching of existing defects by reducing the barrier to reaction and stabilizing the resulting dangling carbon bonds.[92–94]

More recently, the dependence of etching morphology on surface temperature has been demonstrated, with faceted pits aligned with lattice directions formed below a certain critical temperature, transitioning to circular pits as the temperature was increased.[4] This faceting can be attributed to the preferential reaction of armchair-type edge carbons, leaving only hexagonal pits with zig-zag edges aligned with the < 1 1 -2 0 > lattice directions.[95] Although both zig-zag and armchair sites have two neighboring carbon atoms, zig-zag sites have two fully-coordinated nearest neighbors while armchair sites only have one. The higher stability of zig-zag edges thus slightly favors the removal of armchair sites from the surface ($\Delta E_a \approx 0.52$ eV).[4] Above the transition temperature, the reactivity of the two types of edge carbons becomes essentially equivalent and circular pits result.

## 4.2 Experimental

Supersonic beams of molecular oxygen were generated by expanding a 5% $O_2$/95% He gas mixture through a 30 μm diameter molybdenum pinhole at 20 psi and 70 psi for nozzle temperatures of 300 K and 600 K, respectively. The nozzle was heated by resistively heated wire, and the temperature was monitored by a thermocouple. A translational kinetic energy of 0.37 eV with an energy distribution width of $\Delta E/E = 0.28$ was found for the beam with a 300 K nozzle using time-of-flight measurements; the translational kinetic energy of the 600 K beam was extrapolated to be ~0.7 eV. A flux on the order of $10^{13}$ $O_2$ molecules $cm^{-2}$ $s^{-1}$ was determined for both beam conditions. Samples were positioned 1.3 m from the nozzle, with a 2 mm diameter beam spot at the crystal.

HOPG samples were placed in a UHV chamber (base pressure of $1\times10^{-10}$ Torr) in sample mounts that aligned the surface normal either parallel to the beam or at a 45° angle. The sample was maintained at the appropriate temperature (1275-1475 K) during exposure to the supersonic beam of $O_2$. After exposure, the cooled sample was transferred under vacuum to the STM chamber for imaging.

For these experiments, highly oriented pyrolytic graphite (HOPG, SPI-2 and SPI-3) samples were cut into approximately 2 mm × 1 cm strips with a sharp blade and cleaved with adhesive tape. Samples were outgassed in a UHV chamber (base pressure of $1\times10^{-10}$ Torr) up to experimental temperatures (1275-1475 K) prior to exposure. The surface temperature was monitored by a Mikron infrared pyrometer and heated by applying current directly through the sample. Several areas on the surface were checked for cleanliness by STM prior to oxygen exposure. Etched $Pt_{0.8}Ir_{0.2}$ tips were used for imaging. When required, a Phi sputter ion gun was used to create atomic vacancies in the HOPG basal plane by bombarding the sample with 4 keV $Ar^+$ ions. The 4 keV $Ar^+$ ions used to prepare our samples induce local point defects most likely consisting of 1-10 removed atoms per created vacancy, this based on prior STM studies.[96] At this scale, the precise atomic-level morphology of the vacancy is obscured by the electronic enhancement resulting from unsaturated dangling bonds.

## 4.3 Results and Discussion

As the undefected HOPG surface is minimally reactive, defects were introduced by sputtering. **Figure 4-1** shows an unsputtered and unreacted basal plane of HOPG as well as a surface that was sputtered to induce surface vacancies. The average surface density of reactive defects after sputtering was $7\times10^9 \pm 1\times10^9$ $cm^{-2}$. Sputter defects serve as nucleation points, leading to a higher density of etch features. In addition, the defects shorten the nucleation phase, defined as the period of time (exposure) that transpires before visible etch pits are formed. In the case of a sputtered surface, a certain number of atoms must be removed from around the initial vacancy before it is imaged by STM as a depression rather than a hillock. A longer nucleation phase is observed on a clean basal surface in comparison to an artificially defected surface as a result of the amount of exposure necessary for a very low probability event, the abstraction of a fully coordinated basal carbon atom, to occur before this transition from hillocks to pits can commence.

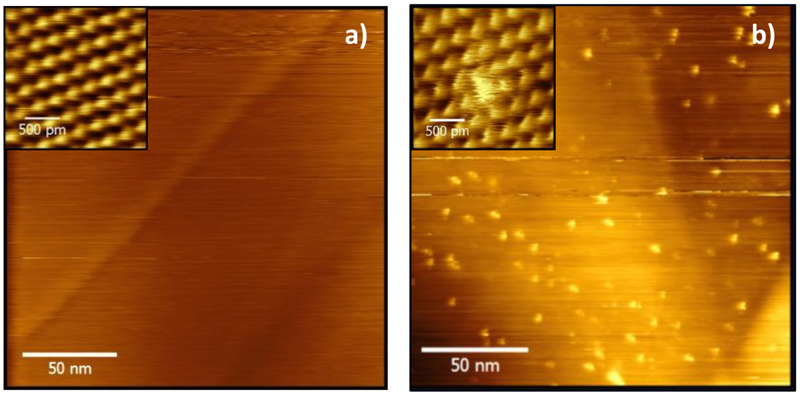

**Figure 4-1**. High resolution STM images. **A)** A typical image of the clean basal plane of HOPG with an inset of the clean lattice. **B)** A typical sputtered HOPG sample (4 keV $Ar^+$) with an inset of a single vacancy formed from collision of an $Ar^+$ ion with the HOPG surface. Images taken at 100 mV and 600 pA.

As seen in **Figure 4-2**, the nucleation phase of a sputtered sample is reduced by half as compared to an unsputtered sample. While nucleation was observed predominantly at sputter defects at a surface temperature of 1275 K, at higher surface temperatures pit formation was observed on the undefected portions of the surface that remained after all initial nucleation points had been consumed. This vertical etching has a higher energetic barrier than lateral etching ($E_a$=2.00 eV compared to $E_a$=1.48 eV for the latter)[76] because it requires the removal of a carbon atom from an undefected basal plane. Therefore, it only emerges at higher surface temperatures and occurs much more slowly.

Along with changes in the overall kinetics of carbon removal from the surface, the surface temperature also affects the morphology of etch pits. Below surface temperatures of ~1325 K, etch pits formed on the surface by exposure to 0.4 eV oxygen were hexagonal. Computational and

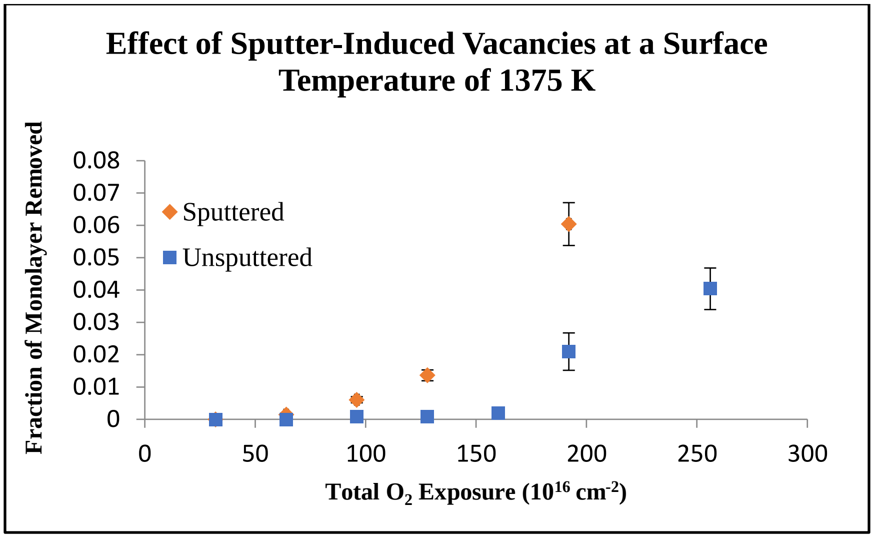

**Figure 4-2.** The effect of sputter-induced vacancies on the nucleation phase of a 1375 K HOPG surface exposed to an effusive distribution of background $O_2$ at 1×$10^{-6}$ Torr.

experimental studies have demonstrated that lower surface temperature etching forms hexagonal pits on the surface due to small energetic differences between removing a zig-zag and an armchair carbon atom.[4] Consequently, armchair sites will etch at a higher rate than zig-zag sites, leading to the formation of hexagonal pits with zig-zag edges, as seen in **Figure 4-3a**. **Figure 4-3b** demonstrates the difference between zig-zag and armchair sites on the HOPG honeycomb lattice, while **Figure 4-3c** is a schematic representing the sequential removal of zig-zag and armchair carbon atoms during the growth of a hexagonal pit. Note that the STM only images every other basal carbon atom in the full honeycomb lattice (namely, out of the α and β atoms contained in each unit cell only the β atom is detected), as seen in **4-3c** and the inset of **4-3a**.[16] At a higher surface temperature of 1375 K, circular, monolayer pits form on the surface when exposed to 0.4 eV $O_2$. This suggests that the surface has enough energy to overwhelm any small energetic differences between armchair and zig-zag sites, which results in the two sites etching at approximately the same rate. This leads to the formation of circular pits, as seen in **Figure 4-4**. A similar transition was found in previous work under different experimental conditions.[4] As would

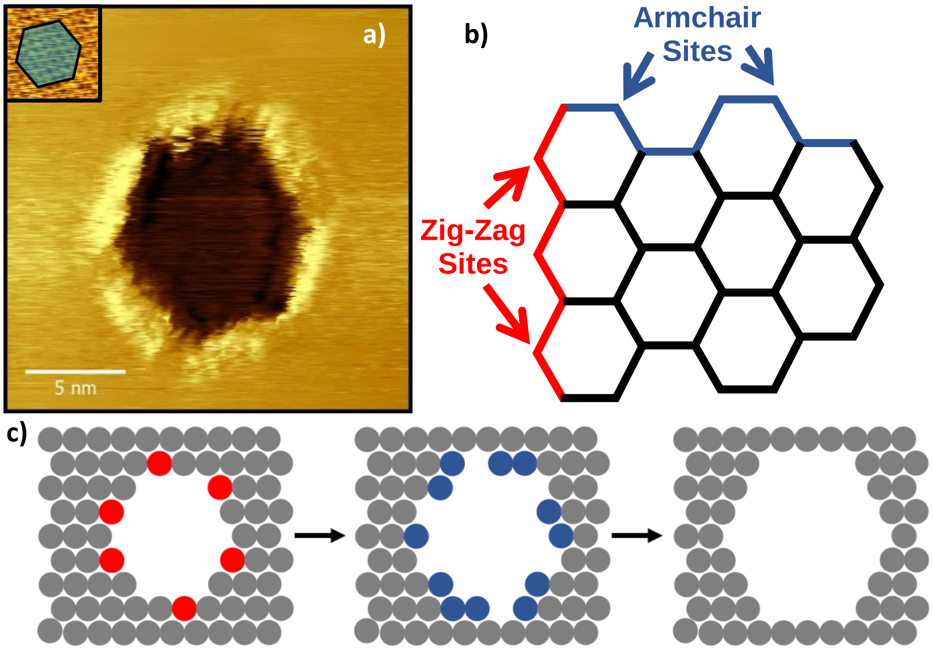

**Figure 4-3. A)** STM image of a representative etch pit formed on a sputtered HOPG sample after exposure to 0.4 eV $O_2$ at a surface temperature of 1275 K, with inset showing lattice aligned with pit edges. Set point: 1.1 V, 600 pA. **B)** Skeleton diagram of the HOPG basal plane demonstrating the difference between zig-zag (red) and armchair (blue) sites. **C)** Schematic representation of the formation of hexagonal pits through preferential etching of armchair (blue) over zig-zag (red) carbon atoms. The diagram represents the lattice as imaged by STM, as seen in the inset of **(A)**.[16]

be expected, the creation of circular etch pits was observed at the higher surface temperature of 1475 K when exposed to 0.4 eV $O_2$, although these pits grew at a much slower rate than those on a 1375 K surface.

Previous work with samples reacted in tube furnaces has demonstrated the diameter of etch pits growing linearly with exposure,[75–78] indicating that the total rate of carbon removal increases with $O_2$ exposure. This suggests that the surface becomes more reactive as etch features grow and edge carbons with unsaturated dangling bonds become more pervasive. Interestingly, under all conditions examined here, the rate of carbon removal was constant with oxygen exposure, with no increase due to the proliferation of edge carbons. This suggests that $O_2$ can adsorb at an arbitrary

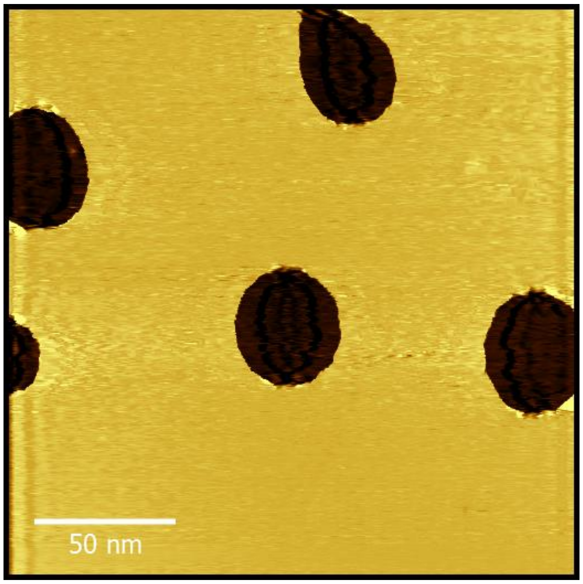

**Figure 4-4.** STM image of representative etch pits formed on a sputtered HOPG sample after exposure to 0.4 eV $O_2$ at a surface temperature of 1375 K. Set point: 300 mV and 600 pA.

location and diffuse across the surface as adsorbed O to find a reactive edge carbon, such that the rate-limiting step of carbon removal from the surface is not sensitive to the density of edge carbons (as in the high $O_2$ flux conditions of previous experiments) but instead is dependent on the concentration of oxygen adsorbed on the surface. **Figure 4-5** demonstrates the constant rate of carbon removal on an HOPG surface at temperatures of 1275, 1375, and 1475 K. The slope of each linear fit corresponds to the probability of a given $O_2$ molecule removing a carbon atom from the surface. For 0.4 eV $O_2$ molecules, the values of these reaction probabilities are $3\times10^{-6} \pm 1\times10^{-6}$, $2\times10^{-4} \pm 1\times10^{-4}$, and $7\times10^{-6} \pm 3\times10^{-6}$ for surface temperatures of 1275 K, 1375 K, and 1475 K, respectively. Previous studies on graphite oxidation have demonstrated non-Arrhenius behavior with respect to surface temperature, and our findings exhibit similar behavior.[71,91] Our experiments in the 1275 K – 1475 K surface temperature range reached a maximum reaction probability at ~1375 K, which agrees well with previously reported values. This behavior is likely due to decreasing coverage of adsorbed O atoms with increased temperature.[5,90] The effect of oxygen

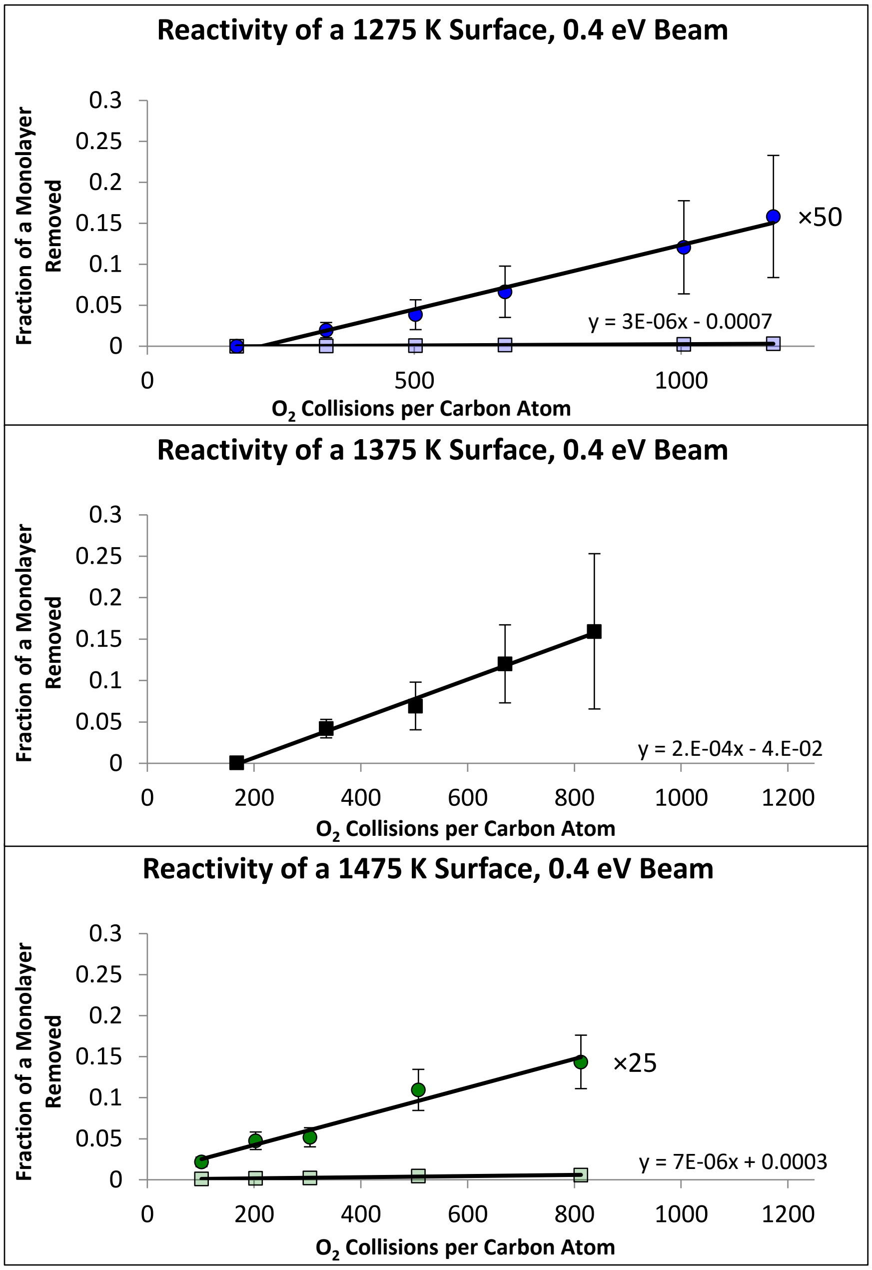

Reactivity of a 1275 K Surface, 0.4 eV Beam

Reactivity of a 1375 K Surface, 0.4 eV Beam

Reactivity of a 1475 K Surface, 0.4 eV Beam

**Figure 4-5.** Reactivity plots of 1275 K (top), 1375 K (middle), and 1475 K (bottom) HOPG surfaces exposed to 0.4 eV $O_2$, where the fraction of the surface monolayer reacted is plotted against the average number of collisions an individual carbon atom has with $O_2$ molecules. The linear fit to each of these plots corresponds to the probability of an $O_2$ molecule ultimately removing a carbon atom from the surface. The reactivity plots for the 1275 K and 1475 K surfaces are magnified by 50 and 25 times, respectively, to be visible on the same scale as the 1375 K surface.

energy on reactivity in the initial oxidation regime is clear in the normally-oriented beam experiments: when the beam energy was raised from 0.4 eV to 0.7 eV, the overall reactivity of the surface increased significantly for both the 1275 K and 1375 K surfaces. The reaction probability of impinging 0.7 eV $O_2$ is $4\times10^{-4} \pm 2\times10^{-4}$ and $5\times10^{-4} \pm 2\times10^{-4}$ for surface temperatures of 1275 K and 1375 K, respectively; this corresponds to an increase of a factor of over 100 for the 1275 K surface and of over 2 for the 1375 K surface, as seen in **Table 4-1**.

| **Translational $O_2$ Energy Normal to the Surface (eV)** | **HOPG Grade** | **Impinging $O_2$ Angle (°)** | **Surface Temperature (K)** | **Reaction Probability** |
|---|---|---|---|---|
| 0.4 | SPI-3 | 90 | 1275 | $3\times10^{-6} \pm 1\times10^{-6}$ |
| 0.4 | SPI-3 | 90 | 1375 | $2\times10^{-4} \pm 1\times10^{-4}$ |
| 0.4 | SPI-3 | 90 | 1475 | $7\times10^{-6} \pm 3\times10^{-6}$ |
| 0.4 | SPI-3 | 45 | 1375 | $1.1\times10^{-4} \pm 5\times10^{-5}$ |
| 0.7 | SPI-3 | 90 | 1275 | $4\times10^{-4} \pm 2\times10^{-4}$ |
| 0.7 | SPI-3 | 90 | 1375 | $5\times10^{-4} \pm 2\times10^{-4}$ |
| 0.7 | SPI-2 | 90 | 1375 | $3\times10^{-5} \pm 1\times10^{-5}$ |
| 0.7 | SPI-2 | 45 | 1375 | $3\times10^{-5} \pm 1\times10^{-5}$ |

**Table 4-1**. A complete list of $O_2$ reaction probabilities for all sets of experimental conditions.

The nucleation time that elapses before the formation of visible pits is also affected by the increase in oxygen energy. **Figure 4-6** shows the amount of carbon consumed by etching with molecular oxygen impinging at a normal angle on a 1375 K surface at both 0.4 eV and 0.7 eV kinetic energies. The nucleation time, graphically defined as the x-intercept of the linear trends,

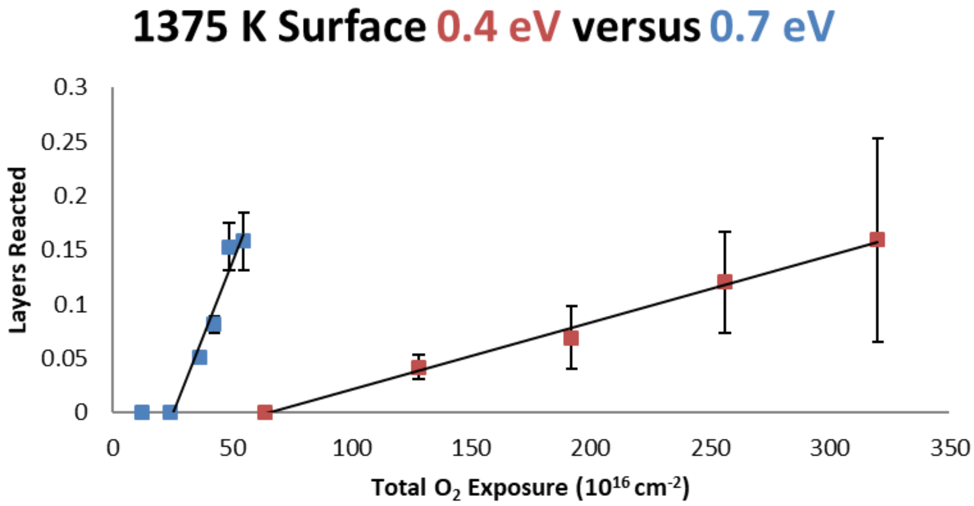

**Figure 4-6.** Reactivity of HOPG samples in terms of layers of graphite reacted versus fluence of $O_2$ from a supersonic molecular beam. Vacancies were introduced by sputtering with 4 keV $Ar^+$ ions to provide nucleation sites. Samples exposed to molecular oxygen with kinetic energies of 0.4 eV (red) and 0.7 eV (blue) at a surface temperature of 1375 K and normal incident angle show marked differences in nucleation time (the x-intercept of the linear regressions) as well as subsequent overall reactivity (the slope). The nucleation time with 0.4 eV oxygen is roughly 2.5 times longer than that of 0.7 eV oxygen.

is about 2.5 times longer for 0.4 eV oxygen, in line with the increase of 1.4 and 2.14 times for defects of 4 and 5 carbon vacancies, respectively, predicted by chemical dynamics simulations performed by our collaborators in the Hase group.[6] Further, the nucleation time does not appear to be strongly related to the subsequent etching rate. The nucleation time for 0.7 eV $O_2$ remained comparatively short even when its etching rate was lowered through the use of a higher quality HOPG sample. Conversely, altering the impingement angle of the beam affected nucleation time but not etching rate, with more glancing angles producing longer nucleation times. Thus, the dissociation process is related in some way to the normal component of the $O_2$ kinetic energy. Taken together the experimental evidence shows that molecular oxygen with higher energy and impingement angles closer to normal do indeed dissociate more readily on sputter vacancies, leading to a higher coverage of adsorbed O and the onset of product formation at smaller $O_2$ exposures.

In addition to increasing the reaction probability of impinging oxygen, raising the incident $O_2$ energy from 0.4 eV to 0.7 eV drastically changes the morphology of the etch features on the surface. 0.4 eV $O_2$ predominantly created symmetrical etch pits, with hexgonal pits formed at lower surface temperatures (<1325 K) and circular pits formed at higher surface temperatures. By contrast, at the higher beam energy of 0.7 eV, irregular, anisotropic etch channels dominated, as seen in **Figure 4-7**. This channeling phenomenon was observed at surface temperatures of both 1275 K and 1375 K, indicating that it is caused solely by the impinging oxygen energy. New pits appeared to remain mostly symmetrical up to a maximum radius of about 20 nm, by which point they spawned rapidly growing channels. The morphology of the pits prior to channeling was similar to those in the 0.4 eV experiments, although the 1275 K surface also formed unusual, nearly triangular pits in some areas (as shown in **Figure 4-7a**) which may result from locally decreased surface temperatures.[97]

It is interesting to note that the reaction probabilities with 0.7 eV $O_2$ at both surface temperatures are roughly equal, suggesting that the large influence of surface temperature over carbon removal rate seen with 0.4 eV oxygen is specific to the formation of circular and hexagonal pits. The enhancement to the reaction probability at both surface temperatures at the higher beam energy can be attributed to the new anisotropic channeling mode that emerges, which is evidently not dependent on surface temperature and dominates over the symmetrical pit etching mode. The etching process giving rise to these channels is thus kinetically as well as morphologically distinct.

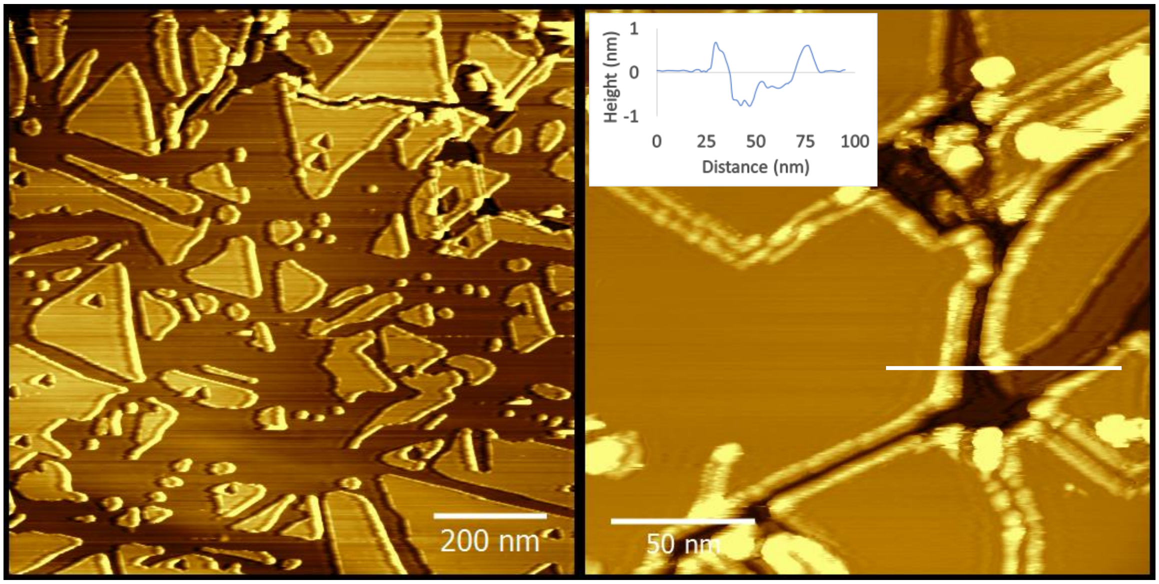

**Figure 4-7**. STM images of representative etch channels formed on a sputtered HOPG sample after exposure to 0.7 eV $O_2$ at a surface temperature of **A)** 1275 K (400mV, 700 pA) and **B)** 1375 K (300 mV, 600 pA); the inset line scan represents areas of single and double layer etching, with two negative contrast terraces at around 0.3 nm and 0.8 nm corresponding to one and two layer deep etch features, respectively. Multilayer etch features are much more abundant on a 1375 K surface in comparison to a 1275 K surface due to increased vertical etching. For example, multilayer etching was more pervasive on the surface shown in (**B)** despite it being exposed to about 1/3 as much $O_2$ as the surface in **(A)**. Faceted etch pits up to ~20 nm in diameter were also observed on the 1275 K surface as seen in **(A)**.

The observed increase in carbon removal rate is unlikely to stem from a direct abstraction mechanism whereby by the $O_2$ molecule removes a carbon atom from the surface through direct collision to form $CO_2$. Studies on systems with much higher incident $O_2$ energies suggest that there is no available reaction mechanism by which an $O_2$ molecule will directly abstract a carbon atom from the surface; the energy required is too great to render this a realistic possibility. Instead, computational and experimental findings demonstrate that $O_2$ does not chemisorb as molecular oxygen but rather undergoes exothermic dissociative chemisorption, forming adsorbed O atoms.[82] Results on higher grade HOPG samples indicate that channels may be following domain boundaries, explaining their irregular, elongated shape. Channels attributed to grain boundaries have been observed previously, although on a larger micron-scale and under different conditions.[98,99] On lower grade HOPG (SPI-3) with lateral grains no larger than 30-40 nm, most pits remain roughly circular up to a ~20 nm diameter before channeling. By contrast, on higher grade samples (SPI-2) with lateral grain sizes of 0.5-1.0 mm, only circular pits are found after exposure to 0.7 eV at a surface temperature of 1375 K, as seen in **Figure 4-8**. This result suggests that intrinsic surface properties dictate channel morphology, as the only significant reactive difference between the two samples is the difference in lateral grain sizes. Due to the absence of channeling, the reaction probability of 0.7 eV $O_2$ on a 1375 K surface drops from $5 \times 10^{-4} \pm 2\times10^{-4}$ on an SPI-3 HOPG surface to $3\times10^{-5} \pm 1\times10^{-5}$ on an SPI-2 HOPG surface, decreasing by over an order of magnitude. This once again demonstrates the connection between kinetics and

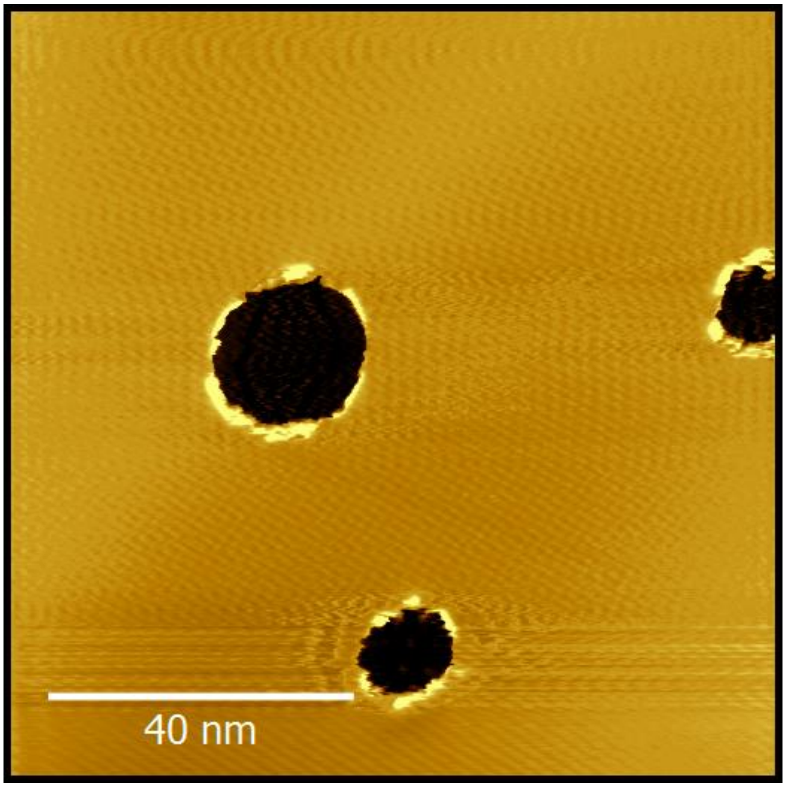

**Figure 4-8**. STM image of representative etch pits formed on a sputtered SPI-2 HOPG sample after exposure to 0.7 eV $O_2$ at a surface temperature of 1375 K. Set point: 300 mV and 700 pA.

morphology: the channeling process must be fundamentally faster than pit formation, and thus when the surface structure is not conducive to channeling the kinetic enhancement of 0.7 eV oxygen fails to materialize.

The relationship between vertical etching rates on 1275 K and 1375 K surfaces remained relatively unchanged with an increase in beam energy from 0.4 eV to 0.7 eV. On a 1375 K surface, large, two-layer etch features were observed after approximately 20% of the surface monolayer was removed, indicating that new etch features were nucleated on the clean second layer after it was unearthed. Additional multi-layer features up to over 20 layers deep, **Figure 4-9**, were observed on the 1375 K sample after an $O_2$ exposure of approximately $4\times10^{18}$ $cm^{-2}$. In contrast, only limited two-layer etch features were observed on the 1275 K HOPG sample, even when about 30% of the surface monolayer was removed, and no etch features over 2 layers deep were observed. Thus, as with 0.4 eV oxygen, the increase in surface temperature allows new pits to nucleate on

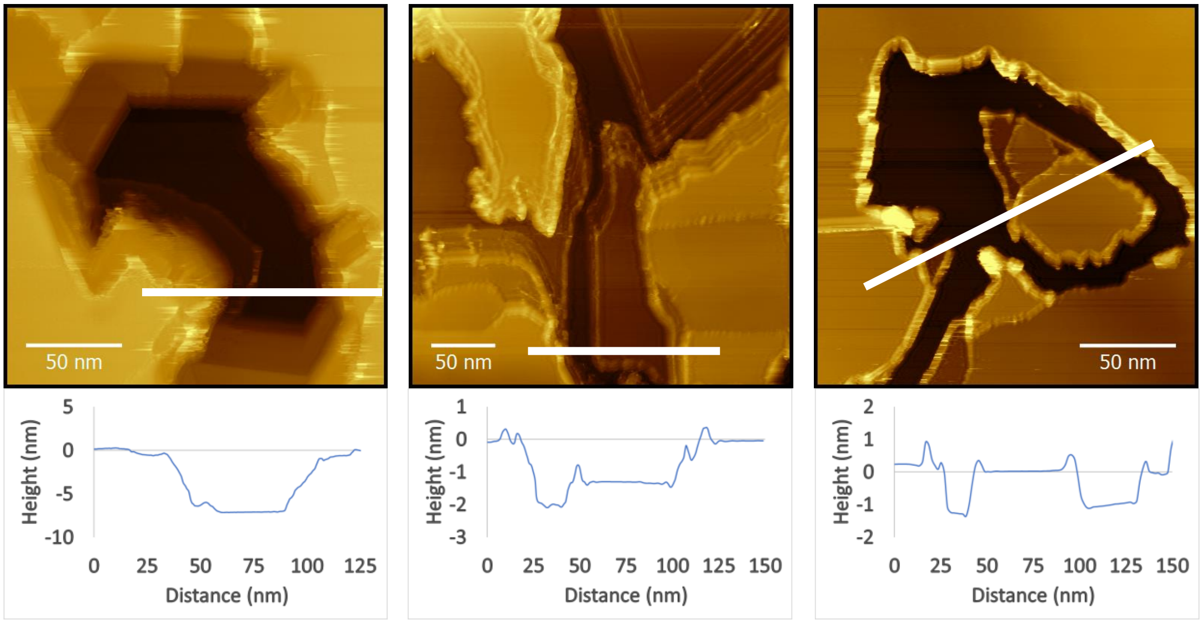

**Figure 4-9**. STM images of multilayer (10's of layers deep) etch pits formed on a sputtered SPI-3 HOPG sample after exposure to 0.7 eV $O_2$ at a surface temperature of 1375 K. Images taken at 300 mV, 700 pA; 100 mA, 700 pA; and 100 mA, 700 pA respectively.

undefected graphite after the consumption of all initial surface defects. This suggests that the abstraction of carbon from the basal plane is limited by surface temperature and not dependent on incident $O_2$ energy.

Experiments conducted with an impinging $O_2$ angle of 45° from the surface normal with 1375 K surfaces suggest that the impact angle of $O_2$ may affect etch feature morphology while the total overall reactivity of the surface remains relatively unchanged. Exposure of 0.4 eV $O_2$ to an SPI-3 1375 K surface at 45° found a negligible decrease in overall reactivity to $1.1\times10^{-4} \pm 5\times10^{-5}$ compared to $2\times10^{-4} \pm 1\times10^{-4}$ with the beam directed normal to the surface. Etch pits were mostly circular as in the normal-angle case. Results from a SPI-2 surface heated to 1375 K and exposed to 0.7 eV $O_2$ at 45° indicate that $O_2$ impinging at that angle may form different etch features than normal-angle $O_2$. The exposed surface was dominated by the formation of faceted, monolayer-deep etch pits, shown in **Figure 4-10a**, in contrast to the circular pits found with 0.7 eV $O_2$ normal to a SPI-2 surface. However, more temperature-dependent studies are needed to conclusively say if and how the impingement angle affects the faceted to circular morphological transition. Interestingly, large elongated pits often nucleated on intrinsic linear defects, as shown in **Figure 4-10b**. While these lines clearly serve as nucleation sites and likely cause the pit elongation by facilitating etching along the defect, they do not form narrow channels like those found on a SPI-3 surface exposed to 0.7 eV oxygen. The measured overall reaction probability with a 1375 K SPI-2 surface exposed to 0.7 eV $O_2$ at a 45° impingement angle is $3\times10^{-5} \pm 1\times10^{-5}$, approximately the same as the normal angle experiment ($3\times10^{-5} \pm 1\times10^{-5}$) despite the $\sqrt{2}$ decrease in $O_2$ translational energy perpendicular the surface. The emergence of faceted pits at a more glancing angle might indicate slight changes in site-selective reactivity, but these differences did not cause a significant change in the overall rate of carbon removal from the surface.

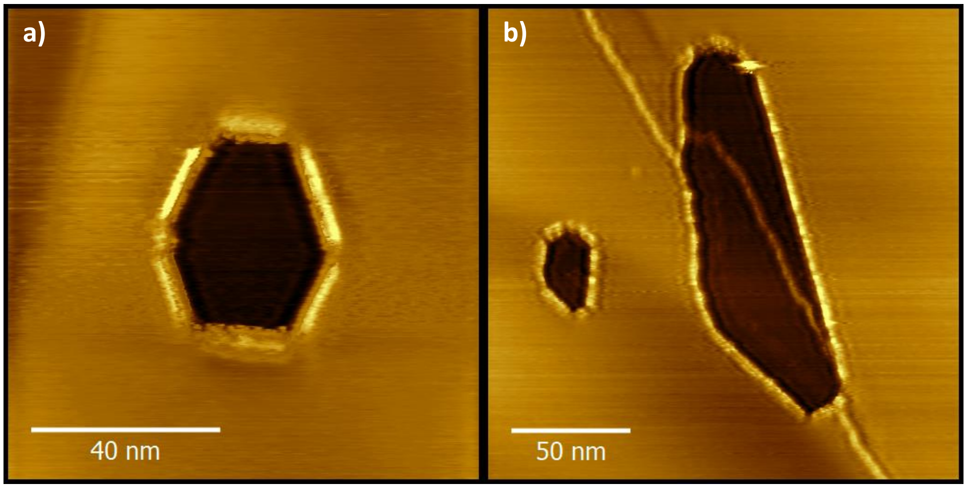

**Figure 4-10.** Images of pits on a 1375 K SPI-2 surface exposed to 0.7 eV $O_2$ impinging at 45° relative to the surface plane. **A)** A faceted pit typical of those that dominated the surface. **B)** An example of a large, elongated pit that formed on a linear defect. Both images were taken at 100 mV and 600 pA.

## 4.4 Conclusions

We have demonstrated the efficacy of using STM and supersonic molecular beams in tandem to combine the realms of macroscopic interfacial kinetics with atomic, nano, and mesoscale morphology, allowing a more holistic examination of graphite oxidation. This novel approach allows us to directly link the time-evolving morphology of the reacting interface with the observed reaction kinetics, in essence, giving access to the spatio-temporal correlations that govern time-evolving interfacial reactivity. The results presented here have uncovered independent effects of oxygen energy, angle, and surface temperature on etching morphology, dictating the formation of hexagonal pits, circular pits, or anisotropic channels. Lower energy (0.4 eV) impinging oxygen produced pits faceted along crystallographic directions on a 1275 K surface that transitioned into circular pits with a 100 K temperature increase. Experiments with different incident angles that compared outcomes using normal versus 45 degrees found only limited kinetic and morphological changes. The reaction probability under a given set of experimental conditions remained constant as the etch features evolved, suggesting that the availability of reactive edge carbons is not the limiting factor in the oxidation rate. An increase in oxygen energy from 0.4 eV to 0.7 eV created anisotropic channels at all surface temperatures, with these features dominating the morphological landscape while other features, such as faceted, circular, and elliptical pits, still exist. Furthermore, the reaction probability increased with impinging oxygen energy, indicating a kinetically distinct process giving rise to the channels. Comparison of the relative reactivity of higher grade versus lower grade HOPG indicates that the formation of etched channels largely depends on the presence of grain boundaries. The fine control over the complete parameter space of surface temperature along with oxygen energy, angle, and flux afforded by this experimental technique has provided fresh insights into the oxidation mechanism for this important model system. Moreover, these findings are of further interest given current needs to perfect advanced carbon containing materials for high performance flight, reentry vehicles, and next generation propulsion systems that need to operate in aggressive oxidizing and high-temperature environments.

# Chapter 5: Room Temperature Oxidation of GaAs(110) Using High Translational Kinetic Energy Molecular Beams of $O_2$ Visualized by STM

## Summary

This study examines the reactive surface dynamics of GaAs(110) oxidation with molecular oxygen at room temperature over a range of impinging kinetic energies. Visualization of the surface by scanning tunneling microscopy (STM) after exposures to $O_2$ with kinetic energies of 0.4-1.2 eV provides morphological and kinetic data that were obtained utilizing a novel instrument that combines a supersonic molecular beam with an in-line, *in-situ* STM. Oxidation was found to proceed by two morphologically distinct, competing mechanisms: a spatially homogeneous process with randomly distributed chemisorbed oxygen atoms leading to layer-by-layer oxide growth, and a spatially heterogeneous process with oxides nucleating on structural surface defects and growing vertically and laterally with continued exposure. Both oxidation mechanisms exhibit enhanced reactivity with increasing kinetic energy. Only trace oxidation was observed with $O_2$ kinetic energies below 0.7 eV; a rapid increase in the rate of oxidation from 1.0-1.2 eV was found with homogeneous and heterogeneous oxidation proceeding simultaneously until full surface coverage was reached. In addition, the relative rates of the two mechanisms appear to change with $O_2$ kinetic energy: spatially homogeneous oxidation is expected to dominate at lower kinetic energies (<0.7 eV) while the heterogenous growth of oxide islands increasingly dominates with higher kinetic energies (≥1.0 eV). The results obtained in this study conclusively demonstrate that a heterogenous oxidation mechanism is activated on GaAs(110) at high $O_2$ kinetic energies, and reveal that thin oxide layers can be achieved with higher efficiency at room temperature using molecular beams of oxygen. These results provide vital information about the morphological evolution of the surface in conjunction with the overall kinetics, and identify a controlled method

of enhanced oxidation at moderate temperatures that could potentially improve abruptness at oxide interfaces and be used in the fabrication of GaAs semiconductor devices.

## 5.1 Introduction

III-V compound semiconductors may be the key to developing ever-faster electronic devices as silicon transistors reach their size limitations.[100] GaAs represents one of the most promising semiconductor materials due to an electron mobility five times that of silicon and a high radiation hardness valuable in aerospace and military applications such as integrated circuits and solar cells for spacecraft.[101] The performance and quality of gallium arsenide metal-oxide-semiconductor (MOS) devices depends critically on the ability to create ultra-thin oxide-films on the substrate surface. Previous studies[102–109] on the oxidation of the GaAs substrate have utilized aggressive conditions involving high-temperature or electrochemical environments to overcome the low reactivity of $O_2$ on GaAs under ambient conditions.[9,110] Ideally, enhancement of GaAs oxidation could be achieved using relatively low surface temperatures and clean environments to maintain surface stoichiometry and reduce defects in the oxide film. A fundamental understanding of the $O_2$-GaAs interface is therefore required to probe new oxidation pathways of the GaAs surface and to ultimately improve the processing and manufacturing of GaAs MOS devices.

In this chapter, we present a marked enhancement of oxidation kinetics on the *p*-type GaAs(110) surface using impinging $O_2$ with high kinetic energies and incident angles oriented normal or 45° to the surface. We have utilized a unique approach to studying interfacial reaction dynamics by visualizing the oxidation of a *p*-type GaAs(110) surface at room temperature with energy- and angle-selected $O_2$ using a combination of supersonic molecular beam and ultra-high vacuum scanning tunneling microscopy (STM) techniques. This experimental approach has been used previously to successfully answer questions about the site-specific reactivity of $O_2$ on Si(111)-7x7[111] and HOPG[112] surfaces. The combination of supersonic molecular beam and STM techniques links time-evolving morphologies to reaction kinetics, providing spatio-temporal correlations that govern the reactivity of surface reactions. By visualizing micrometer to sub-nanometer length-scales over time as oxidation proceeds, we have monitored the oxidation process from its initial phases to the formation of large-scale oxides on the surface. These results demonstrate two simultaneous oxidation mechanisms with distinct spatial distributions: the homogenous accumulation of randomly dispersed chemisorbed oxygen atoms as well as the heterogenous nucleation of oxide islands near defects.

Molecular oxygen starts to dissociatively chemisorb on the GaAs(110) surface at temperatures above 60 K.[113] The initial sticking coefficient for thermally dosed $O_2$ on a clean GaAs(110) surface is $2\times10^{-5}$, with oxygen initially adsorbing at a linear rate followed by a quasi-logarithmic uptake with continued exposure.[110] Results from AES and XPS studies indicate that the initial chemisorption ($\sim3\times10^{5}$ L; 1 L = $10^{-6}$ Torr sec) of $O_2$ is slow and only increases the surface coverage to $\Theta = 0.05$–$0.1$ depending on the amount of surface defects present.[114] The main oxygen uptake onto the surface proceeds *via* activated adsorption followed by field-assisted growth of an oxide phase;[115–118] the formation of subsurface oxides is still disputed.[119–121] Subsequent oxidation appears to be layer-by-layer[115,117] and has been described by the Mott-Cabrera mechanism,[122] a phenomenon in which an electric field assists the oxidation process *via* electrons tunneling through the oxide film.[118] While the initial oxidation is generally assumed to be spatially homogeneous across the surface, there is some indication of spatially inhomogeneous oxidation with oxide islands nucleating on defects.[119,120]

Numerous AES and photoemission studies[123–128] have addressed the bonding coordination of the adsorbed oxygen, with results indicating varying bonding geometries during different stages of the oxidation process. At high oxygen coverages, experimental[119–121] and theoretical evidence[129] indicates O atoms are multicoordinated about equally between Ga and As atoms. In the initial oxidation regime, conflicting evidence supports preferential bonding to surface As[124,130,131] and Ga[114,120,132,133] atoms, as well as bonding in bridge-bond positions with coordination to both Ga and As.[126,134] Experimental and theoretical studies on multiple GaAs(100) surfaces have demonstrated that the bonding of oxygen to surface Ga atoms is thermodynamically favored over bonding to surface As atoms.[135–137]

STM imaging of the clean GaAs(110) surface exhibits atom-selective behavior in which positive sample biases with respect to the STM tip (unoccupied-state imaging) visualize the Ga atoms while negative sample biases (occupied-state imaging) visualize the As atoms.[138] Investigations using STM have demonstrated spatially homogeneous oxidation with the stochastic appearance of scattered oxidized sites on the GaAs(110) surface,[134,139] while the spatially heterogenous nucleation and growth of oxide islands has also been observed by STM on the GaAs(100) surface.[140] The presence of spatially homogeneous adsorbed oxygen atoms on a *p*-type GaAs(110) surface was found on defect-free terraces as shown by subsequent imaging in the same ~225 nm$^2$ area after exposure, and the imaging suggests that the adsorbed oxygen sits in an interchain bridging site aligned in the $[1\bar{1}0]$ direction with respect to the surface As atoms.[134] The adsorbed O atoms demonstrate slight variations in topographical height and width with changes in imaging conditions but always appear as small isolated protrusions on the surface with a lateral size of 4-6 Å at full-width half-maximum (FWHM) on a *p*-type sample. This differs significantly from the delocalized nature of oxygen adsorbates on an *n*-type sample that results from the negatively-charged nature of the adsorbed O atom, as opposed to the neutral adsorbates on *p*-type samples.[139,141] Spatially heterogenous oxidation was observed on a *n*-type GaAs(100) surface, with nucleation centers growing to cover the surface in a manner similar to the oxidation mechanism found on InP.[140,142] 100 nm ×100 nm STM images of the surface with continued exposure to air revealed the nucleation of oxide islands, which grew laterally to cover the surface in a uniform oxide layer ~2 nm thick. This stands in contrast with previous findings indicating that GaAs oxidation is homogenous across the surface and proceeds layer-by-layer.

The results shown in this chapter will detail the reactive oxidation of a GaAs(110) sample at room temperature using high kinetic energy impinging $O_2$ while visualizing the corresponding morphological evolution of the surface during exposures. By employing a combination of molecular beam and STM techniques, we have explored the energetic barriers to reaction using monoenergetic $O_2$ and have illustrated two kinetically and morphologically distinct mechanisms of oxide growth: the heterogeneous nucleation and growth of oxide-islands at $O_2$ kinetic energies ≥1.0 eV, and the homogenous accumulation of randomly distributed oxidized sites leading to layer-by-layer oxide growth. Characterization of the kinetics and surface evolution of both modes of oxide formation will be detailed, and a comprehensive overview of the high kinetic energy oxidation of the GaAs(110) surface will be presented.

## 5.2 Experimental

The results reported here were obtained using a new UHV instrument combining supersonic molecular beam and STM/AFM techniques. The instrument is composed of a triply differentially pumped beamline, a surface preparation/characterization chamber, and an SPM chamber containing a variable temperature SPM based on the ultra-stable design of Shuheng Pan, built in collaboration with RHK. As described in **Chapter 2**, the custom-built Pan STM has been designed with the surface plane vertical such that the sample can be exposed to the supersonic molecular beam with the STM tip still in contact. This unique configuration and the high stability of the microscope allow given nanoscopic areas to be revisited after exposure to the molecular beam, tracking the progression of surface oxidation over time.

Supersonic molecular beams were generated by the expansion of a 5% $O_2$/95% He gas mixture through a 30 μm molybdenum pinhole at pressures from 20-80 psi and nozzle temperatures ranging from 300-975 K (± 5%). The translational kinetic energy of the molecular beam at each nozzle temperature was measured using time-of-flight (TOF), and values of 0.38 ± 0.04 eV, 0.73 ± 0.08 eV, 0.97 ± 0.15 eV, 1.10 ± 0.12 eV, and 1.22 ± 0.17 eV were found for nozzle temperatures of 300, 575, 775, 875, and 975 K, respectively. The uncertainty values in these energies represent the FWHM of each energy distribution. The molecular beam flux for all beam conditions was on the order of $10^{13}$ $O_2$ molecules $cm^{-2}$ $s^{-1}$, as determined by the method described in **Chapter 2**. The GaAs(110) sample was positioned in the SPM chamber during exposures, with a 4 mm diameter beam spot on the crystal. The sample was held at room temperature for all experiments and the surface plane was oriented either normal or at 45° with respect to the impinging beam. The kinetic energy of oxygen in each beam therefore exceeds the thermal energy of the room temperature surface by over an order of magnitude. Imaging was performed between beam exposures. Same-spot visualization experiments, whereby the same set of atoms could be revisited after exposure to high kinetic energy $O_2$, were completed by moving the STM tip laterally multiple micrometers downrange (away from the $O_2$ beam) from the reference area during each exposure to mitigate tip shadowing while keeping the tip in contact with the surface. The STM tip was then moved back to the reference area after the exposure and the set of reference atoms were located using topographical markers on the surface. Only areas of the sample with direct line of sight to the beam were reacted after exposure, confirming that thermalized $O_2$ reflected from the STM tip and/or chamber did not significantly affect the oxidation of the surface.

GaAs(110) crystals (*p*-type Zn-doped, VGF grown, MTI Corporation) were used for all experiments, and were cut into approximately 5 mm × 1 cm strips for appropriate fit onto the sample mounts. Samples were cleaned in a UHV chamber (<5×$10^{-11}$ Torr base pressure) by repeated cycles of ion sputtering at room temperature using 0.5-1.0 keV $Ar^+$ ions followed by subsequent annealing at 700 K ± 30 K to form the well-ordered GaAs(110) surface.[143–145] The surface was heated by applying current directly through the sample and the temperature was monitored using a Mikron infrared pyrometer ($\varepsilon = 0.69$) during the annealing process. An ion flux of ~7 μA/$cm^2$ was measured during the sputtering cycles. STM images were taken using etched or cut $Pt_{0.8}Ir_{0.2}$ tips.

### 5.3 Results and Discussion

A representative clean GaAs(110) surface as imaged by STM is shown in **Figure 1**, which was achieved after multiple cycles of ion sputtering with 0.5-1.0 keV $Ar^+$ ions and subsequent annealing to ~700 K. **Figure 1A** demonstrates both the overall terrace size and topography of the surface on a larger, mesoscopic scale. **Figure 1B** and **1C** illustrate the clean row structure on the terraces running horizontally (and slightly down moving left to right) across the images, along with individual bright site surface defects. The observed row structure in the nanoscopic images

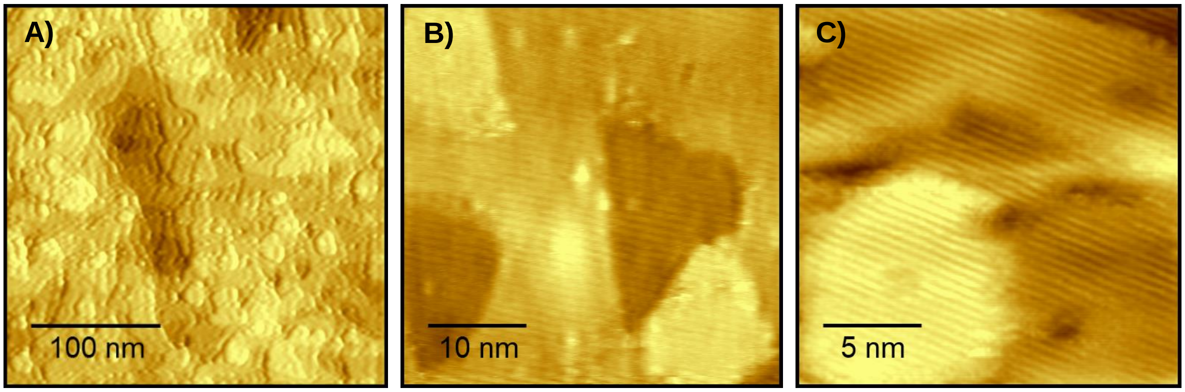

**Figure 5-1. A)** 300 nm × 300 nm (-2.8 V, -0.6 nA), **B)** 40 nm × 40 nm (2.8 V, 0.6 nA), and **C)** 20 nm × 20 nm (-3.0 V, -0.3 nA) STM images of representative clean GaAs(110) surfaces obtained after multiple sputter/anneal cycles. The terrace sizes and overall roughness of the surface are illustrated in **A)**, while the row structure can be seen running horizontally (and slightly down moving left to right) across **B)** and **C)**, along with the presence of natural bright site defects.

matches the expected periodicity of the GaAs(110) surface, scales appropriately with images of different sizes, and does not change with varying scanning conditions.

No significant oxidation was observed with exposures up to 6×$10^{17}$ $cm^{-2}$ using $O_2$ with kinetic energies of 0.4 eV, while 0.7 eV $O_2$ demonstrated only minimal surface oxidation. A critical threshold in reactivity was reached around 1.0 eV, as shown in **Figure 5-2**. After this point, reactivity increased at a greater than linear rate with kinetic energy, reaching a value at 1.2 eV about four orders of magnitude higher than what has been observed previously with background exposure to room temperature oxygen.[9] The observed increase in reactivity is likely due in large part to the activation of the heterogenous oxidation mechanism with oxygen energies ≥0.7 eV. As shown in **Figure 5-3**, STM imaging has revealed the nucleation and growth of "oxide islands"

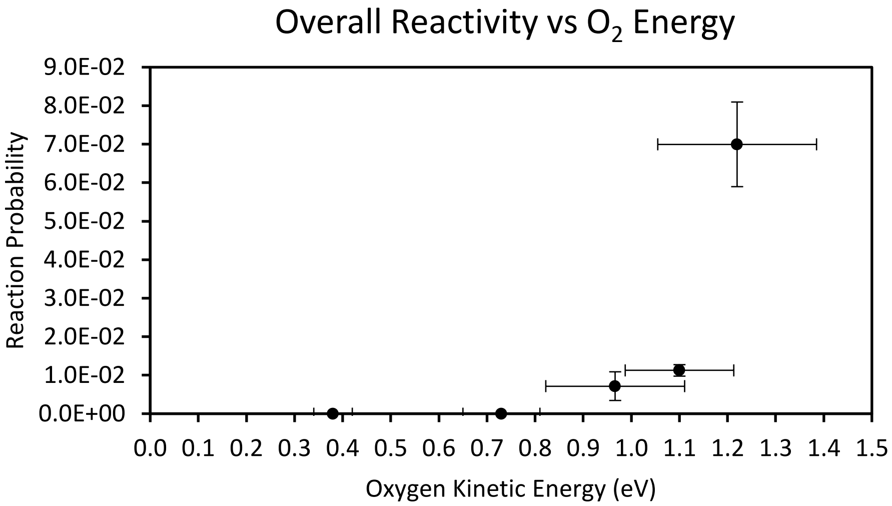

**Figure 5-2.** Overall reaction probability vs $O_2$ kinetic energy for exposure to oxygen impinging normal to the surface with kinetic energies between 0.4 eV and 1.2 eV. Reactivity sharply increases after a critical threshold energy is reached between 0.7 eV and 1.0 eV, showing a nonlinear relationship between $O_2$ energy and reactivity. The horizontal error bars are derived from the TOF measurements at each beam energy to show the width of the distribution of $O_2$ kinetic energies.

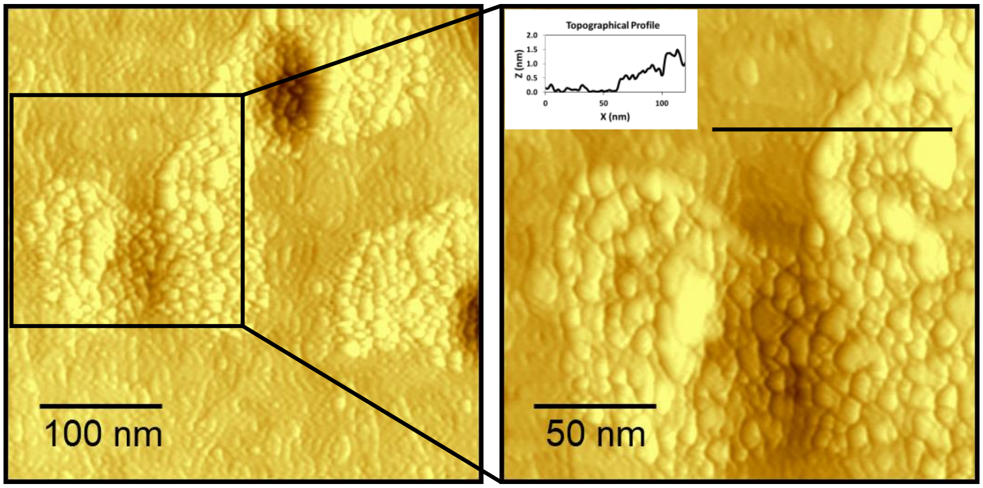

**Figure 5-3.** A 400 nm × 400 nm STM image (-2.0 V, -0.6 nA) of an oxide island on a GaAs(110) surface after exposure to ~$7\times10^{16}$ cm$^{-2}$ of 0.7 eV kinetic energy $O_2$ with a magnified image (200 × 200 nm; -2.0 V, -0.6 nA) showing a more detailed view of the same area. The topographical profile on the magnified image demonstrates the corrugation and height of the oxide island. Spatially heterogeneous oxidation creates patches of oxide that nucleate on surface defects, such as the pit shown here, and grow laterally to cover the surface with further oxygen exposure.

after exposure to ~$7\times10^{16}$ cm$^{-2}$ of 0.7 eV $O_2$ normal to the surface that appear to nucleate on or near pit defects. The oxide islands have a height profile of ~5-10 Å above the surface with both positive and negative scanning bias, consistent with a thin oxide film.[146,147] The oxide islands completely replace the row structure seen on clean terraces and are morphologically distinct from the clean GaAs(110) surface. Given that the surface in all cases was dominated by such ~5-10 Å tall oxide islands, the reactivity shown in **Figure 5-2** was calculated by approximating the fully oxidized surface as consisting of a uniform 10 Å thick sheet of β-$Ga_2O_3$, as any $As_2O_3$ formed at the interface with GaAs is expected to react to form $Ga_2O_3$ and As.[148] This 10 Å thickness value represents an upper bound on the probable thickness of the oxide layer at full coverage. Reaction probability per impinging $O_2$ molecule, $P$, is then given by

$$P = \frac{3\,h\,N_A \rho_{Ga_2O_3}}{2\,M_{Ga_2O_3}\Phi_{O_2} t} \qquad 5-1$$

for oxide thickness $h = 10$ Å, density $\rho_{Ga_2O_3}$, Avogadro's number $N_A$, molar mass $M_{Ga_2O_3}$, stoichiometric factor $\frac{3}{2}$, flux of impinging oxygen $\Phi_{O_2}$, and time to fully oxidize the surface $t$. The reaction probability is therefore here defined as the ratio of the number of impinging $O_2$ molecules that contribute to the 10 Å thick oxide layer to the total fluence of $O_2$ molecules. This calculation allows a reasonable comparison of relative reactivities in order to determine the effect of impinging $O_2$ energy on the reactivity of the GaAs(110) surface.

Infrequent oxide islands grew to a maximum area on the order of $10^4$ nm$^2$ with exposures up to $5\times10^{17}$ cm$^{-2}$ of 0.7 eV oxygen, and cumulatively covered a very small percentage of the surface. At higher energies (≥1.0 eV), the islands expanded laterally with continued exposure until they consumed the entire surface. In some cases, islands grew vertically as well as laterally, with STM visualization revealing the presence of tall, multilayer oxide islands spanning >1 µm in diameter, such as the one shown in **Figure 5-4**. The dramatic vertical growth of these islands likely indicates multilayer/subsurface oxidation near intrinsic large-scale surface defects (*i.e* microfissures, dislocations, *etc.*) as previously suggested in the literature, [120] which then cause the

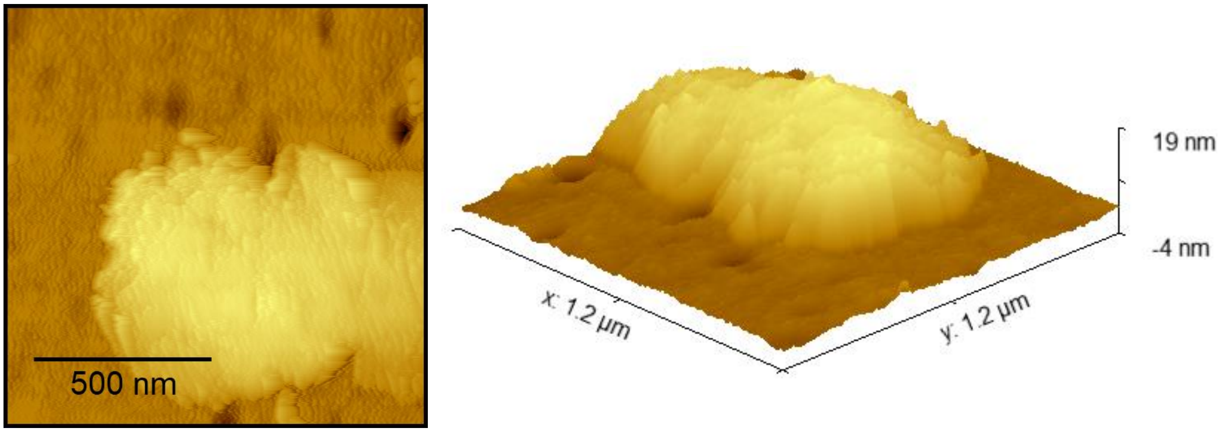

**Figure 5-4.** A 1.2 µm × 1.2 µm image (-2.8 V, -0.6 nA) STM image of an elevated oxide island on a GaAs(110) surface formed after a total exposure of ~$1\times10^{17}$ cm$^{-2}$ of $O_2$ with a kinetic energy of 1.0 eV. A 3D representation of the STM image is shown at right to emphasize the height and roughness of the oxide island. The high vertical elevation of such islands may indicate subsurface oxidation and "blistering" of the surface.

surface to “blister” as a result of the lattice expansion resulting from the formation of subsurface $Ga_2O_3$ and/or $As_2O_3$. **Figure 5-5** shows the uplift of clean GaAs terraces after exposure to 1.2 eV oxygen, possibly as a result of subsurface oxidation. This area of the surface is adjacent to a large-scale surface defect, which comports with the idea that subsurface oxidation occurs through the exploitation of deep surface fissures. This blistering mechanism explains the vertical growth of the islands without the need for mass transport of gallium and arsenic atoms, which at room temperature would be too slow to represent a realistic possibility.

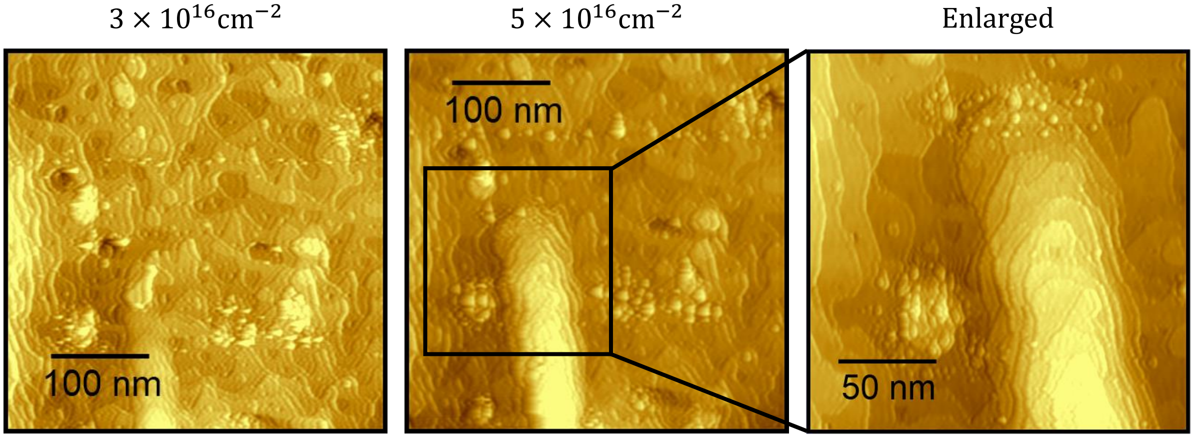

**Figure 5-5.** Sequential STM images (-2.8 V, -0.6 nA) in the same local area illustrating the elevation of clean terraces on a room temperature GaAs(110) surface after exposure to 1.2 eV $O_2$ impinging 45° from normal to the surface. Two 400 nm × 400 nm images show the area after $3 \times 10^{16}$ $\mathrm{cm}^{-2}$ $O_2$ exposure (left) and after $5 \times 10^{16}$ $\mathrm{cm}^{-2}$ $O_2$ exposure (center). The morphological change is likely due to subsurface oxidation and subsequent lattice expansion resulting in the “blistering” of the surface. The magnified 200 nm × 200 nm image at right highlights the raised terraces seen in the middle image.

Using our unique ability to monitor a single nanoscopic area while it is exposed to high energy oxygen, we have directly observed the growth of oxide islands with exposure to 1.2 eV $O_2$ impinging at a 45° angle (0.8 eV kinetic energy normal to the surface) as shown in **Figure 5-6**,

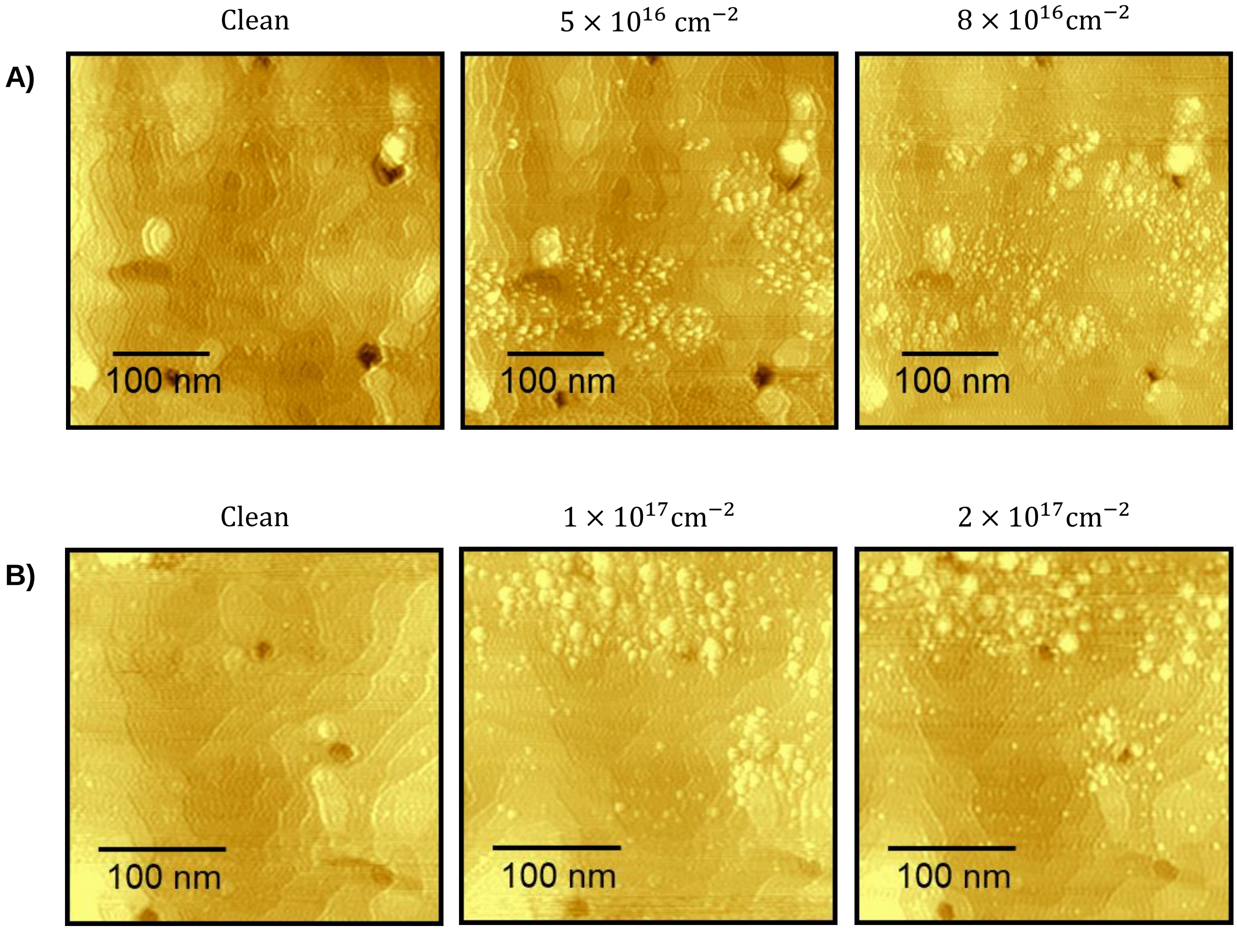

**Figure 5-6.** Multiple examples of sequential STM images (-2.8 V, -0.6 nA) in which the same local area is revisited after each exposure, directly demonstrating the growth of spatially heterogeneous oxide structures on a room temperature GaAs(110) surface with exposure to 1.2 eV $O_2$ impinging 45° from normal to the surface. Total exposures of $O_2$ are given above each STM image. **A)** A sequence of 400 nm × 400 nm images in a single area. **B)** A sequence of 300 nm × 300 nm images in another area with longer exposures. Both **A)** and **B)** demonstrate the emergence of spatially heterogeneous oxide patches (seen as clusters of large bright features on the surface) while nearby terraces remain largely unoxidized.

providing explicit evidence of the spatially heterogeneous oxidation mechanism. This figure illustrates representative examples of the spatially heterogeneous growth of patches of oxide in otherwise clean areas on the GaAs surface. Each set of images shows a single nanoscopic area as it is exposed to oxygen, demonstrating spatially heterogeneous oxide islands nucleating near defects and growing across the surface. There is a sharp divide between oxidized and unoxidized areas in these images, with the terraces not overtaken by oxide islands remaining clean. These images demonstrate conclusively that the heterogenous oxidation mechanism is activated at high oxygen energies, with oxide islands nucleating and growing laterally across the surface while surrounding areas remain unoxidized.

STM imaging with a variety of different surface bias values indicates that the observed elevation of the oxide islands is reflective of the surface topography, not electronic effects. The exact coordination of the chemisorbed oxygen atoms within the oxide cannot be determined by STM, but due to the inherent instability of the GaAs-$As_2O_3$ interface, the oxides are assumed to largely consist of $Ga_2O_3$.[148] The observed spatial heterogeneity suggests that the activated dissociative chemisorption of the high kinetic energy $O_2$ is favored on intrinsic surface defect sites, consistent with previous findings.[119,120] Subsequent three-dimensional oxide growth might then occur at these nucleation sites, which would lead to the formation of the spatially heterogeneous oxide islands. The results of this study conclusively demonstrate the activation of a distinct heterogeneous oxidation process, adding to the knowledge base on the oxidation of this important electronic material.

Although heterogenous oxidation is the dominant mechanism at high oxygen kinetic energies, the homogenous mechanism was also found to occur simultaneously, indicating competition between the two mechanisms. Representative examples of a surface before and after exposure to normal-angle 1.0 eV $O_2$ are shown in **Figure 5-7**, with the randomly distributed bright features corresponding to individual oxidized sites.[134] An analysis of the x and y coordinates of the bright protrusions in seven 40 nm × 40 nm images of a surface exposed to $4\times10^{17}$ $cm^2$ of 1.0 eV oxygen, including the one shown in **Figure 5-7B,** finds an average nearest neighbor separation of 2.2 ± 0.1 nm, which matches the separation of 2.2 ± 0.1 nm expected for a stochastic process

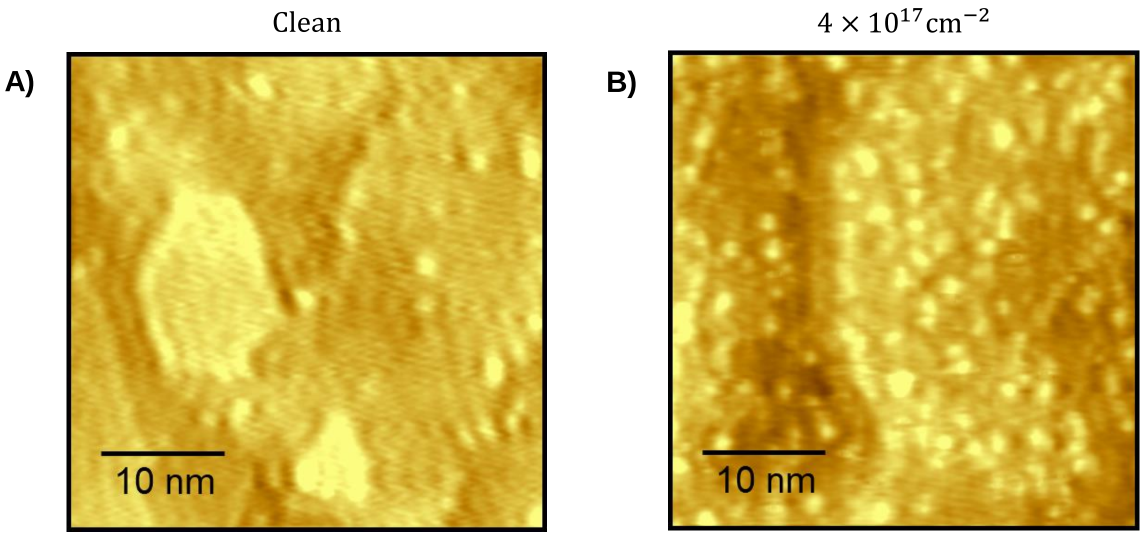

**Figure 5-7.** STM images in different local areas of the surface, representative of the **A)** clean GaAs(110) surface (40 nm × 40 nm; -3.0 V, -0.6 nA) and **B)** a surface after exposure to ~$4\times10^{17}$ $\mathrm{cm}^{-2}$ of $O_2$ with a kinetic energy of 1.0 eV (40 nm × 40nm, -2.0 V, -0.6 nA). Comparison of these two images demonstrates the difference in the density of chemisorbed oxygen atoms (the bright protrusions) before and after exposure to 1.0 eV $O_2$ as the surface undergoes homogeneous oxidation. The spacing between nearest neighbors matches that of a stochastic process, indicating that the presence of the oxidized sites does not significantly affect the reactivity of surrounding surface atoms.

once the presence of image boundaries is taken into consideration.[149] The density of oxidized sites grows linearly with exposure, as shown in **Figure 5-8** for exposure to 1.1 eV oxygen. The slope of this plot corresponds to the reaction probability of the homogenous mechanism at this oxygen kinetic energy. The linear trend therefore indicates a constant reaction probability with exposure, suggesting that in the low coverage limit, the homogeneous chemisorption of oxygen atoms to the GaAs(110) surface does not affect the subsequent reactivity of the surrounding surface sites. The spatially homogeneous oxidation mechanism therefore represents a stochastic process in the low coverage limit whereby oxygen molecules dissociatively chemisorb on unreacted surface sites with a constant reaction probability. The reaction probability of the homogeneous oxidation mechanism at higher coverages could not be measured due to the complete consumption of the surface in an oxide layer resulting from the kinetically dominant heterogeneous oxidation process.

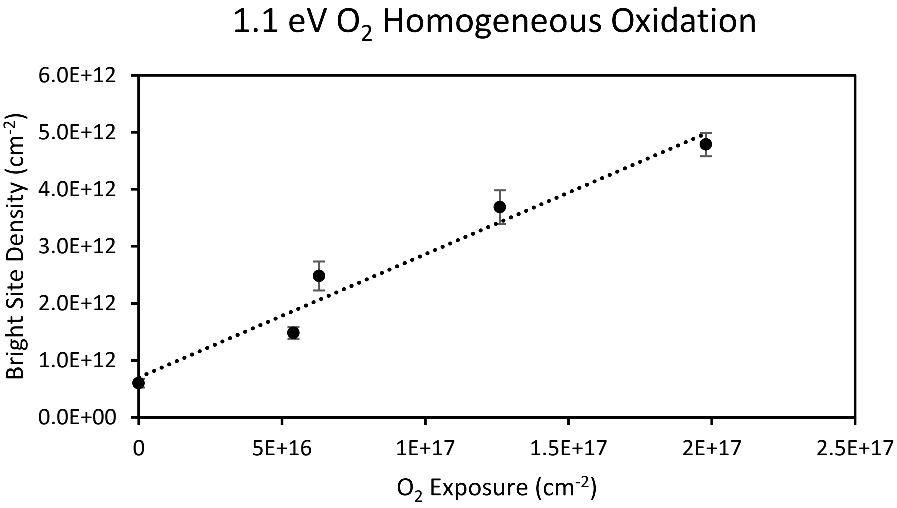

**Figure 5-8.** A reactivity plot demonstrating the increasing areal density of homogeneous oxidation sites on a room temperature GaAs(110) surface after continued exposure to $O_2$ with a kinetic energy of 1.1 eV. The slope of the linear fit represents the probability of an $O_2$ molecule colliding with the GaAs(110) surface and forming an individual bright protrusion as imaged by STM. The linearity of the fit indicates that oxidized sites do not influence the reactivity of the surface to subsequent oxidation in the low coverage limit.

Measurements of oxide formation on the GaAs(110) surface demonstrate that increasing $O_2$ translational kinetic energy normal to the surface greatly enhances the reactivity of both the spatially heterogeneous and homogeneous mechanisms of oxidation above the observed energy threshold of 0.7-1.0 eV. The comparative kinetics for the heterogeneous and homogeneous oxidation mechanisms are plotted in **Figure 5-9** for impinging $O_2$ energies from 1.0-1.2 eV; this plot demonstrates the strong correlation for both mechanisms between impinging $O_2$ kinetic energy and the reactivity of a room temperature GaAs(110) surface. The heterogeneous reaction probability was calculated indirectly by subtracting the contribution of the homogeneous mechanism from the overall reaction probability. The figure demonstrates that the fast kinetics of the heterogeneous mechanism completely dominate surface oxidation at $O_2$ kinetic energies $\geq 1.0$ eV. The homogeneous oxidation reaction rate follows a similar trend as the heterogeneous reaction rate with increasing $O_2$ kinetic energy, but the values for the reaction probability of the homogeneous mechanism at each energy are 3-4 orders of magnitude lower than those of the heterogeneous growth mechanism. The dominant oxidation mechanism at high oxygen energies is therefore the heterogenous nucleation of oxide islands on surface defects that grow laterally to consume the surface, outcompeting the homogenous accumulation of oxidized sites and subsequent layer-by-layer growth.

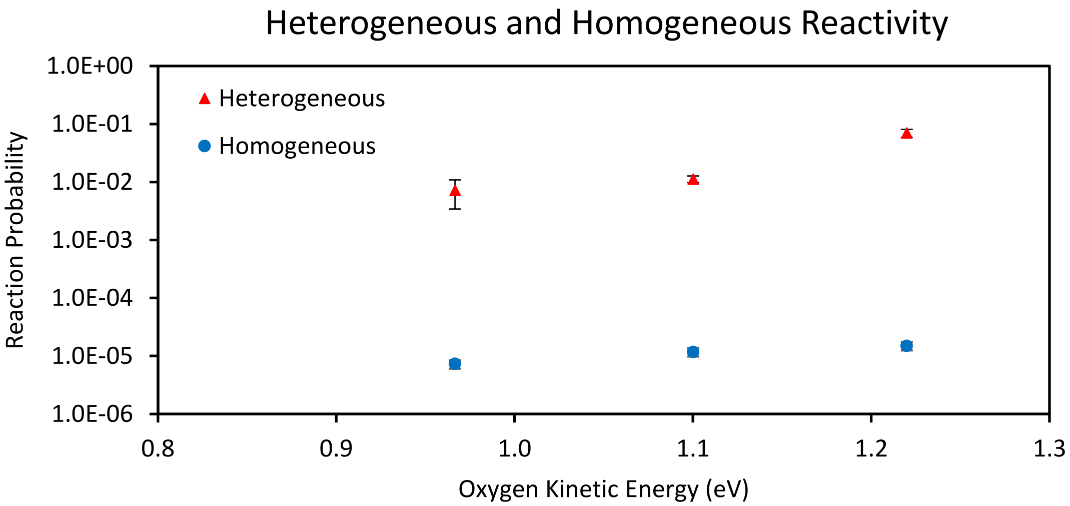

**Figure 5-9.** A reactivity plot illustrating the $O_2$ impinging kinetic energy dependence of the reaction probabilities of the heterogeneous and homogeneous oxidation mechanisms on a room temperature GaAs(110) surface. The data show that the reactivities of both mechanisms increase with oxygen kinetic energy, and that the heterogeneous mechanism dominates over the homogenous mechanism at each energy. The reaction probability is plotted on a logarithmic scale on the y-axis, and is calculated as the ratio of the number of individual bright oxidized sites to the total number of $O_2$ collisions for the homogeneous mechanism, and as ratio of the number of impinging $O_2$ molecules that contribute to a 10 Å thick oxide layer to the total fluence of $O_2$ molecules (minus the contribution of the homogeneous mechanism) for the heterogeneous mechanism.

## 5.4 Conclusions

The results of this study demonstrate the enhanced oxidation of a room temperature GaAs(110) surface using impinging $O_2$ with high kinetic energies ($\geq$1.0 eV), representing an enhanced method of oxidizing a GaAs surface at moderate temperatures. Surface dynamics and energetic dependencies at the atomic scale were examined by monitoring the *in-situ* evolution of the GaAs(110) surface during exposures to tightly controlled energy- and angle-selected $O_2$. Increasing the kinetic energy of the impinging $O_2$ dramatically increases the probability for dissociative chemisorption, while also markedly altering the morphology of the resulting oxides. Oxidation proceeds through multiple competing mechanisms, with the dominant oxidation mechanism dependent upon the incident $O_2$ kinetic energy. While the homogenous mechanism with randomly distributed oxidized sites leading to layer-by-layer growth is expected to dominate at low oxygen kinetic energies, at high kinetic energies the heterogenous mechanism dominates, with oxide islands nucleating on surface defects and growing laterally and vertically. Results suggest that the oxide islands can be physically uplifted by subsurface oxidation that nucleates at defect sites and induces lattice expansion that forces the surface to grow vertically in a "blistering" fashion. Homogeneous oxidation was observed occurring simultaneously but at a lower rate, resulting in the domination of the heterogeneous mechanism. The heterogeneous formation and growth of oxide islands was observed at all impinging $O_2$ kinetic energies at or above 1.0 eV, with the reaction probabilities of both mechanisms increasing with oxygen kinetic energy. The results of this study reveal spatio-temporal correlations that link the varying oxidation kinetics on the GaAs(110) surface to specific surface morphologies on a broad range of length scales. This provides new insight into the initial oxidation stages of GaAs surfaces that is vital to better controlling oxidation during material processing, represents a possible method of creating crucial ultra-thin oxide films with enhanced efficiency at lower surface temperatures, and offers a potential route to enabling a high degree of interfacial abruptness. A greater understanding of the dynamics of GaAs oxidation holds the potential for new techniques allowing passivation and modification of GaAs at moderate surface temperatures for the effective manufacturing and optimal functioning of this high-performance semiconductor.

# Appendix 1: Raw Data Referenced in Figures

This appendix contains images that were used to create each figure presented in this thesis along with the file names.  The figure in which the data appear is given in the captions.  All images used for this thesis are in an electronic repository maintained by the Sibener Group.

**Figure A1-1**

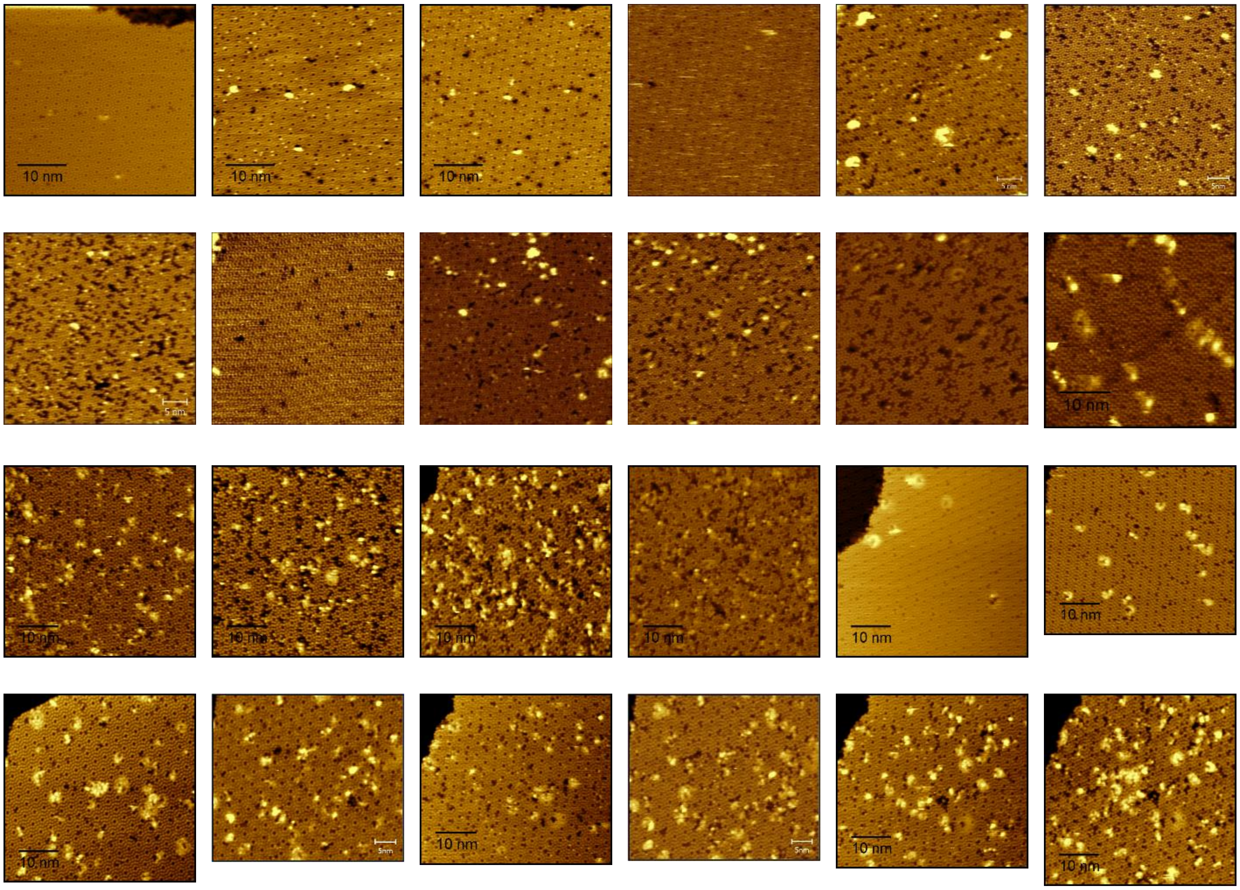

The images used in **Figure 3-5** and **Figure 3-7.**

**Figure A1-1 cont.**

Filenames from top left to bottom right:

Directory: Appendix\A1-1
033015_0007
033015 O2_0015
033015 O2_0023
050115_0006cropped
050115-10 min 95%He5%O2_0016.cropped
050115-20 min 95%He5%O2_0023
050115-30 min 95%He5%O2_0033cropped
050615_0010cropped
050715-10 min seeded beam_0016
050715-20 min seeded beam_0030
050715-30 min seeded beam_0039cropped
101315-O2 seeded 2min_0028cropped
101315.49
101315.58
101315-O2 seeded 8min_0064
101315.69
101515_0012
101515-O2 seeded-1 min_0019
101515-O2 seeded-2 min_0035
101515-O2 seeded-3 min_0044
101515-O2 seeded-3 min_0049
101515-O2 seeded-4 min_0057
101515-O2 seeded-4 min_0062
101515-O2 seeded-4 min_0064

**Figure A1-2**

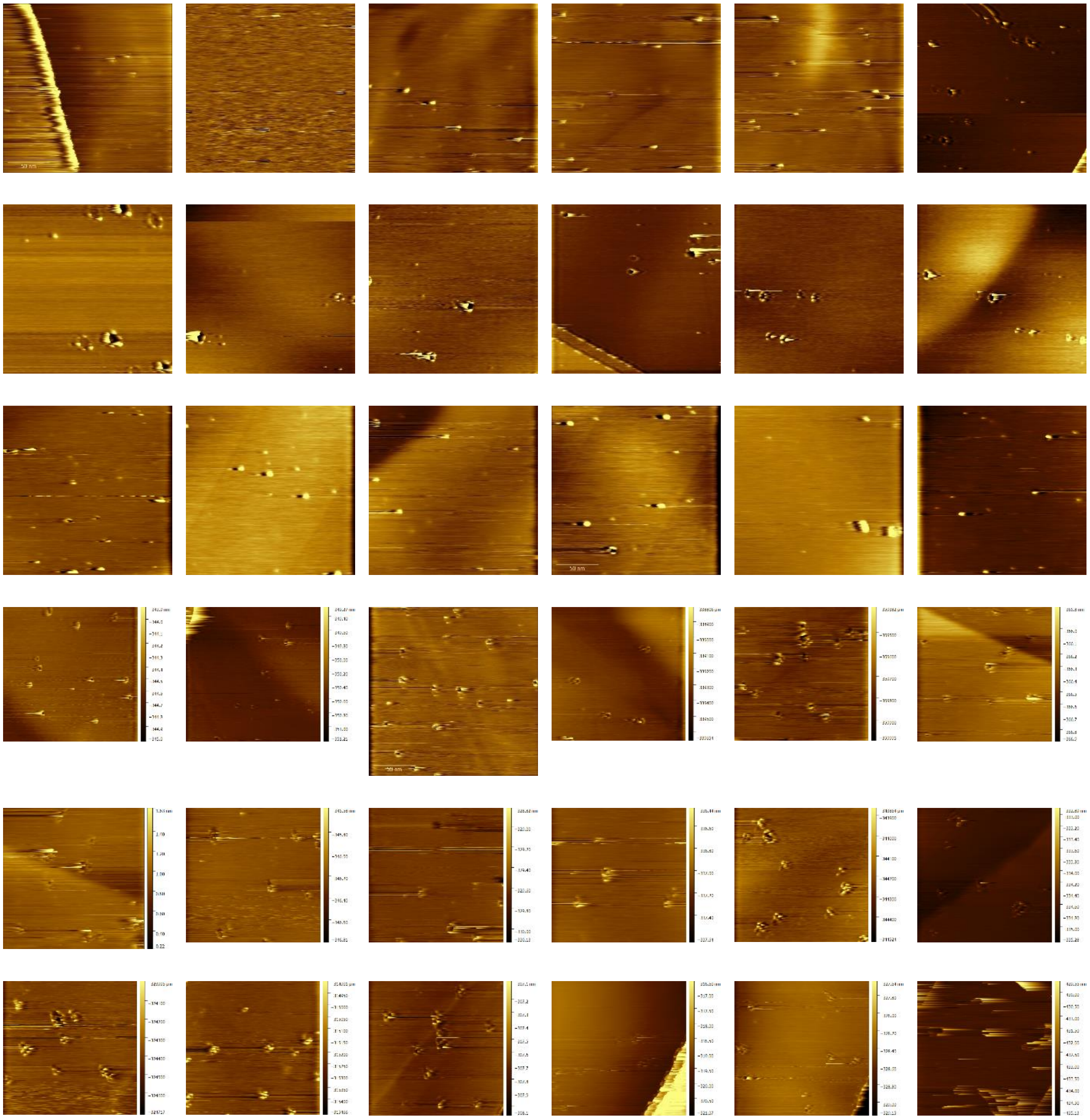

The first set of 36 images used in **Figure 4-2.**

**Figure A1-2 cont.**

Filenames from top left to bottom right:

Directory: Appendix\A1-2\ Sputtered, Leak O2 15min
081716_0019

Directory: Appendix\A1-2\ Sputtered, Leak O2 30min
081916_0002
081916_0003
081916_0004
081916_0007
081916_0010
081916_0011
081916_0012
081916_0013
081916_0014
081916_0015
081916_0016
081916_0018
081916_0019
081916_0020
081916_0021
081916_0022
081916_0023

Directory: Appendix\A1-2\ Sputtered, Leak O2 45min
081916_0024
081916_0025
081916_0026
081916_0027
081916_0028
081916_0029
081916_0030
081916_0031
081916_0032
081916_0033
081916_0034
081916_0035
081916_0036
081916_0037
081916_0038
081916_0040
081916_0041
081916_0042

**Figure A1-3**

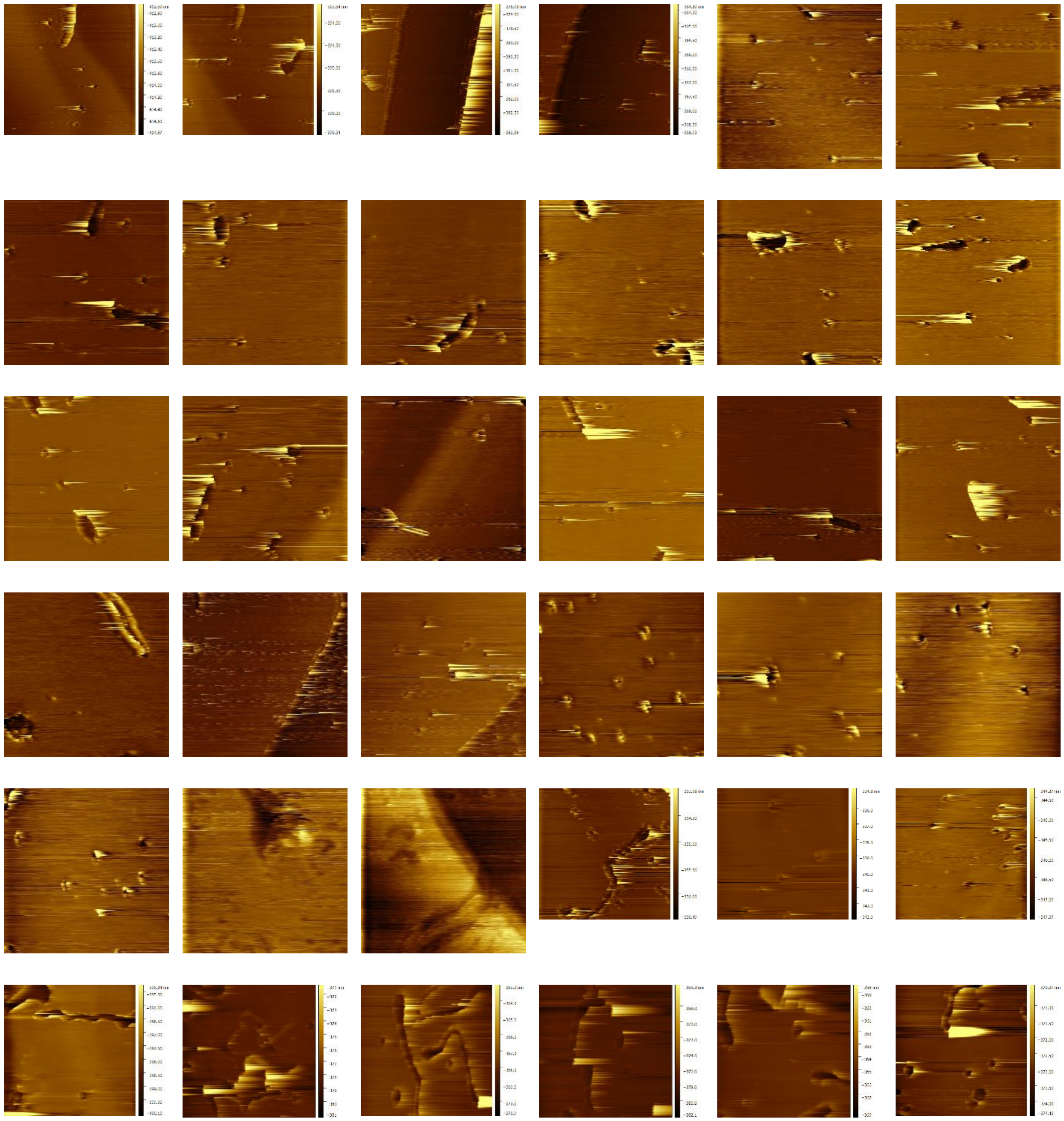

The second set of 36 images used in **Figure 4-2.**

**Figure A1-3 cont.**

Filenames from top left to bottom right:

Directory: Appendix\A1-3\Sputtered, Leak O2 45 min
082116_0001
082116_0002
082116_0003
082116_0004

Directory: Appendix\A1-3\ Sputtered, Leak O2 60min
082216_0002
082216_0003
082216_0004
082216_0005
082216_0006
082216_0007
082216_0008
082216_0009
082216_0010
082216_0011
082216_0012
082216_0013
082216_0014
082216_0015
082216_0016
082216_0017
082216_0018
082216_0019
082216_0020
082216_0022

Directory: Appendix\A1-3\ Sputtered, Leak O2 90min
082216_0023
082216_0024
082216_0027
082216_0029
082216_0031
082316_0001
082316_0002
082316_0003
082316_0004
082316_0005
082316_0006

**Figure A1-4**

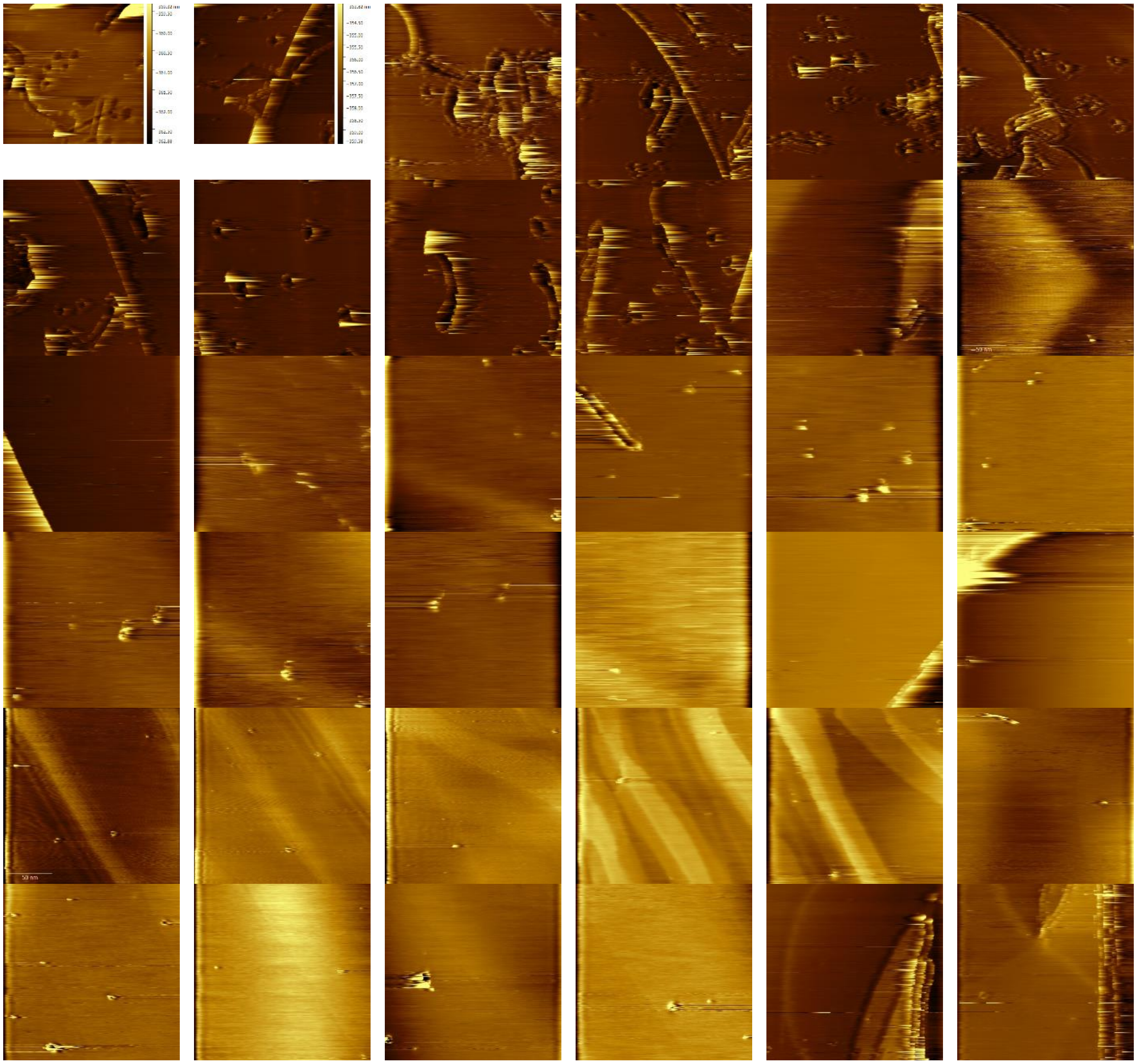

The third set of 36 images used in **Figure 4-2.**

**Figure A1-4 cont.**

Filenames from top left to bottom right:

Directory: Appendix\A1-4\Sputtered, Leak O2 90 min
082316_0007
082316_0008
082316_0009
082316_0010
082316_0011
082316_0012
082316_0013
082316_0014
082316_0015
082316_0016

Directory: Appendix\A1-4\Unsputtered, Leak O2 15 min
082316_0020
082316_0024

Directory: Appendix\A1-4\Unsputtered, Leak O2 30 min
082416_0013
082416_0018

Directory: Appendix\A1-4\Unsputtered, Leak O2 45 min
082416_0022
082416_0023
082416_0024
082416_0025
082416_0026
082416_0028
082416_0029
082416_0030
082416_0031
082416_0032
082416_0035
082416_0036
082416_0037
082416_0038
082416_0039
082416_0040
082416_0041
082416_0042
082416_0043
082416_0044

**Figure A1-4 cont.**

Directory: Appendix\A1-4\Unsputtered, Leak O2 60 min
082516_0001
082516_0002

**Figure A1-5**

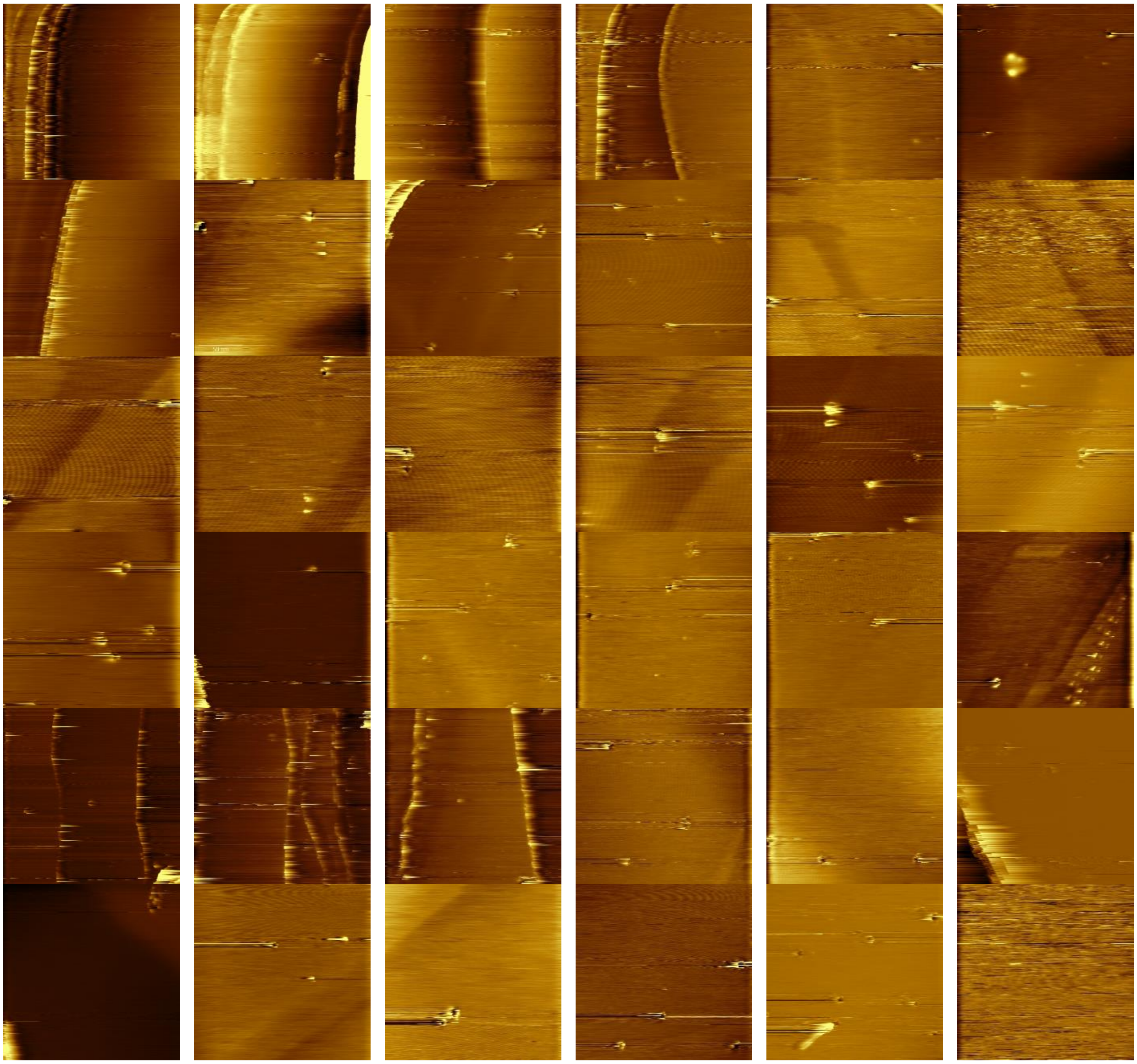

The fourth set of 36 images used in **Figure 4-2.**

**Figure A1-5 cont.**

Filenames from top left to bottom right:

Directory: Appendix\A1-5\Unsputtered, Leak O2 60 min
082516_0003
082516_0004
082516_0005
082516_0006
082516_0007
082516_0008
082516_0009
082516_0010
082516_0012
082516_0013
082516_0014
082516_0015
082516_0016
082516_0017
082516_0018
082516_0019
082516_0020
082516_0021

Directory: Appendix\A1-5\Unsputtered, Leak O2 75 min
082516_0022
082516_0023
082516_0024
082516_0025
082516_0026
082516_0027
082516_0028
082516_0029
082516_0030
082516_0031
082516_0033
082516_0034
082516_0035
082516_0036
082516_0037
082516_0038
082516_0039
082516_0040

## Figure A1-6

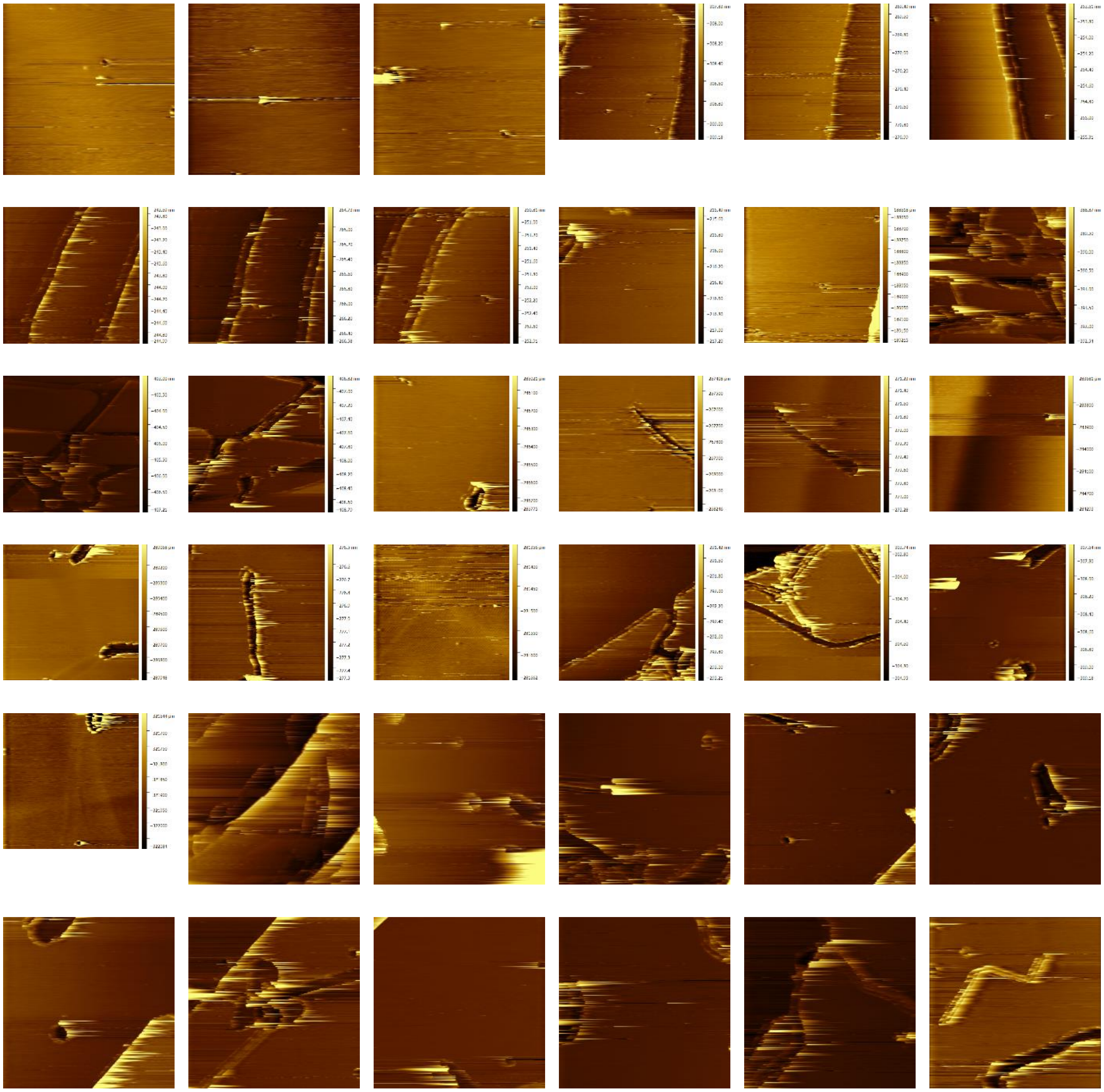

The fifth set of 36 images used in **Figure 4-2.**

**Figure A1-6 cont.**

Filenames from top left to bottom right:

Directory: Appendix\A1-6\Unsputtered, Leak O2 75 min
082516_0041
082516_0042
082516_0043

Directory: Appendix\A1-6\Unsputtered, Leak O2 90 min
082516_0044
082516_0045
082516_0046
082516_0047
082516_0048
082516_0049
082516_0050
082516_0051
082516_0052
082516_0053
082516_0054
082616_0001
082616_0002
082616_0003
082616_0004
082616_0005
082616_0006
082616_0007
082616_0008
082616_0009
082616_0010
082616_0011

Directory: Appendix\A1-6\Unsputtered, Leak O2 120 min
082616_0012
082616_0013
082616_0014
082616_0015
082616_0016
082616_0017
082616_0018
082616_0019
082616_0020
082616_0021
082616_0022

**Figure A1-7**

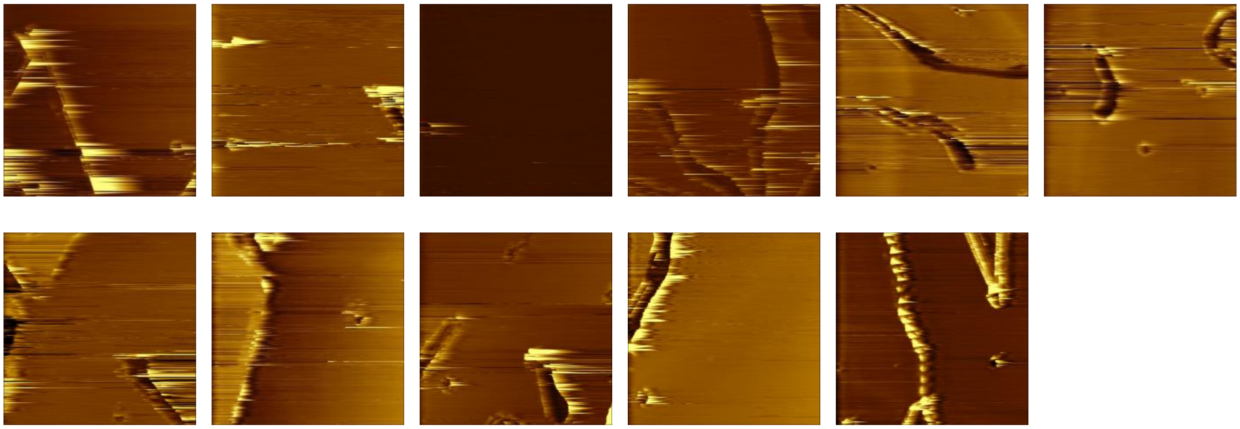

The final 11 images used in **Figure 4-2.**

**Figure A1-7 cont.**

Filenames from top left to bottom right:

Directory: Appendix\ Unsputtered, Leak O2 120min
082616_0023
082616_0024
082616_0025
082616_0026
082916_0001
082916_0002
082916_0003
082916_0004
082916_0005
082916_0006
082916_0007

**Figure A1-8**

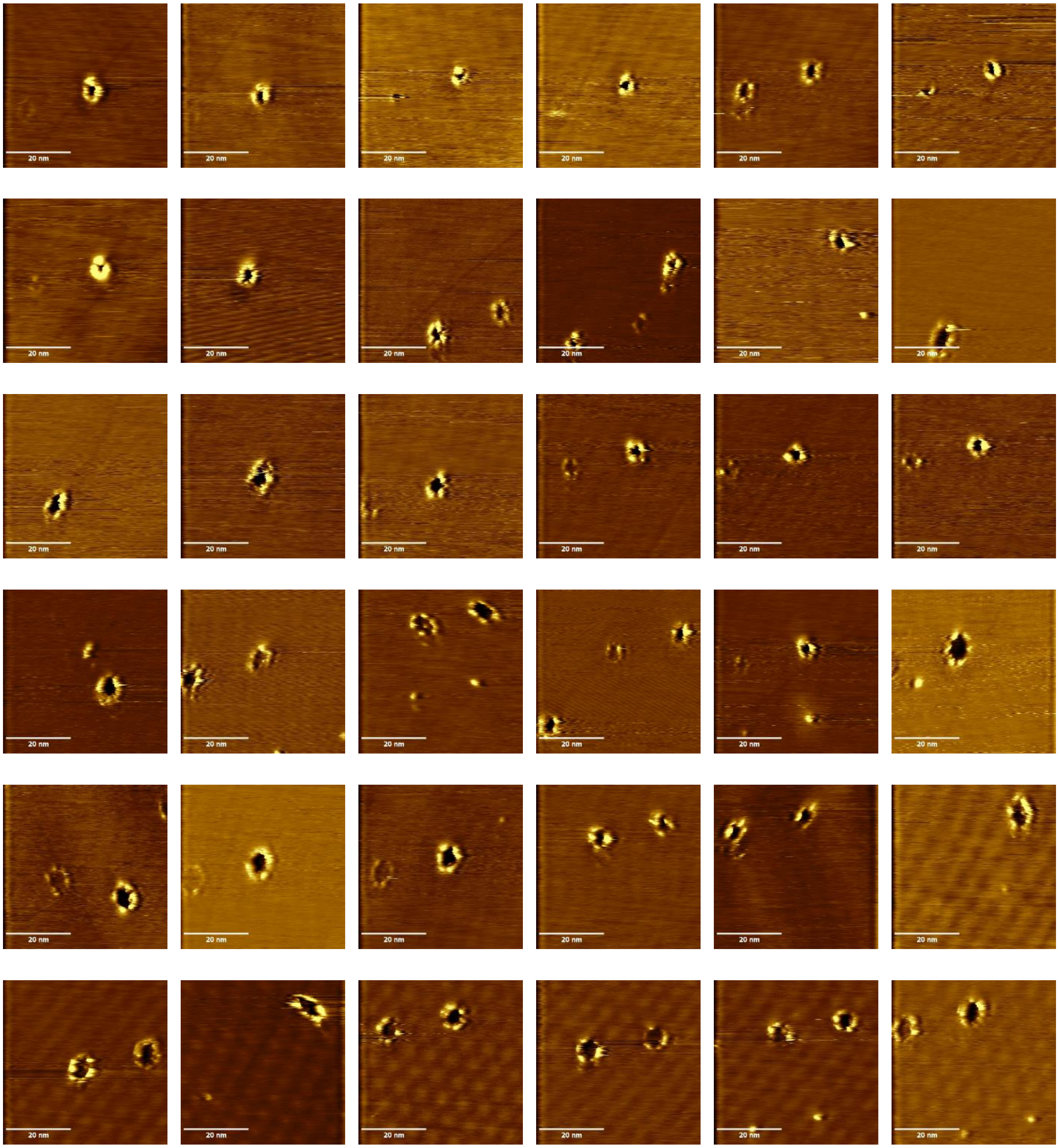

The first set of 36 images used in the top graph in **Figure 4-5** and the first row of **Table 4-1.**

**Figure A1-8 cont.**

Filenames from top left to bottom right:

Directory: Appendix\A1-8\1000C, 0.4eV Beam 7hrs
022817_0002
022817_0005
022817_0007
022817_0010
022817_0014
022817_0016
022817_0018
022817_0019

Directory: Appendix\ A1-8\1000C, 0.4eV Beam 10.5hrs
030117_0007
030117_0008
030117_0009
030117_0012
030117_0013
030117_0016
030117_0018
030117_0020
030117_0021
030117_0022
030117_0024
030217_0001
030217_0006
030217_0011
030217_0013

Directory: Appendix\ A1-8\1000C, 0.4eV Beam 14hrs
030217_0016
030217_0019
030217_0021
030217_0022
030217_0026
030217_0027
030217_0029
030217_0030
030217_0031
030217_0032
030217_0033
030217_0034
030217_0035

## Figure A1-9

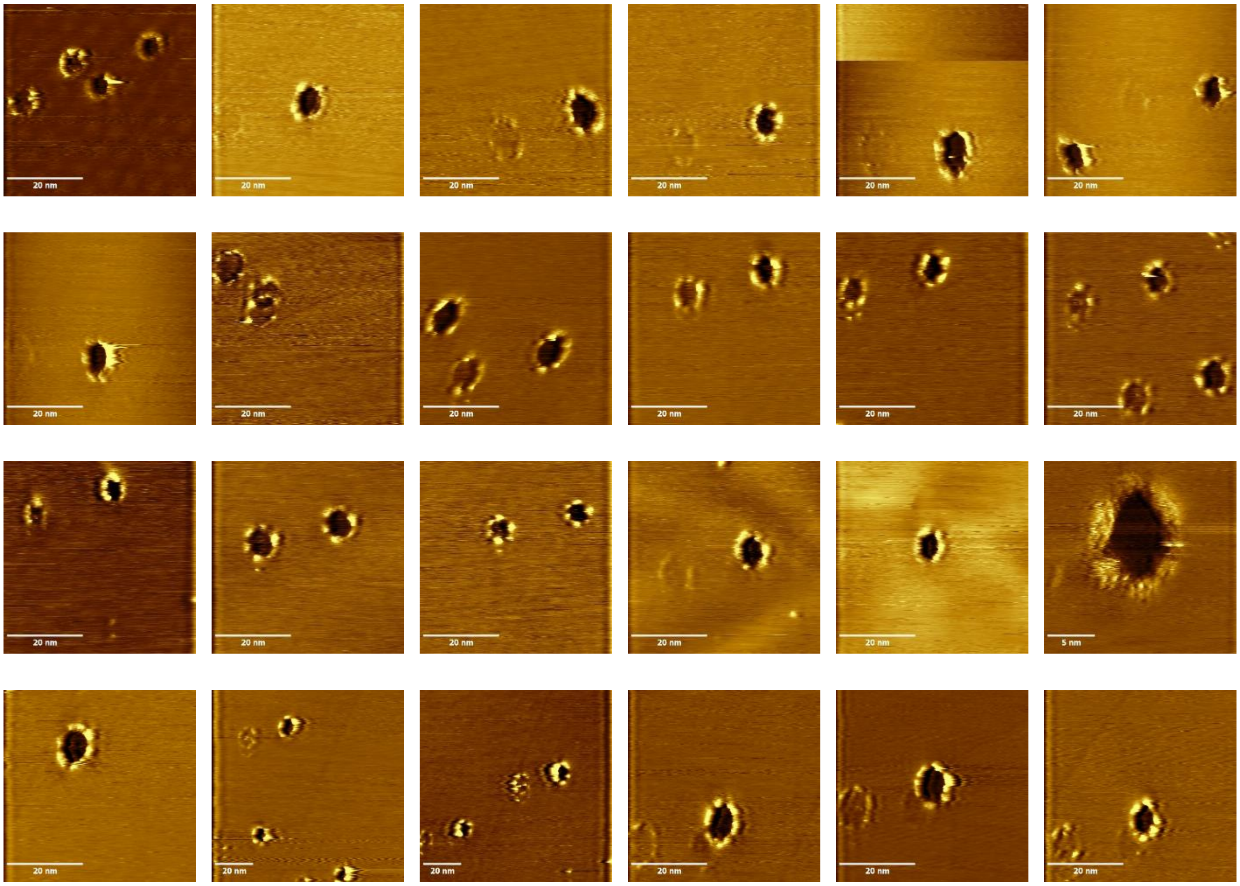

The last 24 images used in the top graph in **Figure 4-5** and the first row of **Table 4-1.**

**Figure A1-9 cont.**

Filenames from top left to bottom right:

Directory: Appendix\A1-9\1000C, 0.4eV Beam 14hrs
030217_0036

Directory: Appendix\A1-9\1000C, 0.4eV Beam 21hrs
030817_0002
030817_0006
030817_0007
030817_0009
030817_0011
030817_0012
030817_0013
030917_0001
030917_0002
030917_0003
030917_0004
030917_0005
030917_0006
030917_0007
030917_0010
030917_0011

Directory: Appendix\A1-9\1000C, 0.4eV Beam 24.5hrs
030917_0013
030917_0015
030917_0017
030917_0018
030917_0020

## Figure A1-10

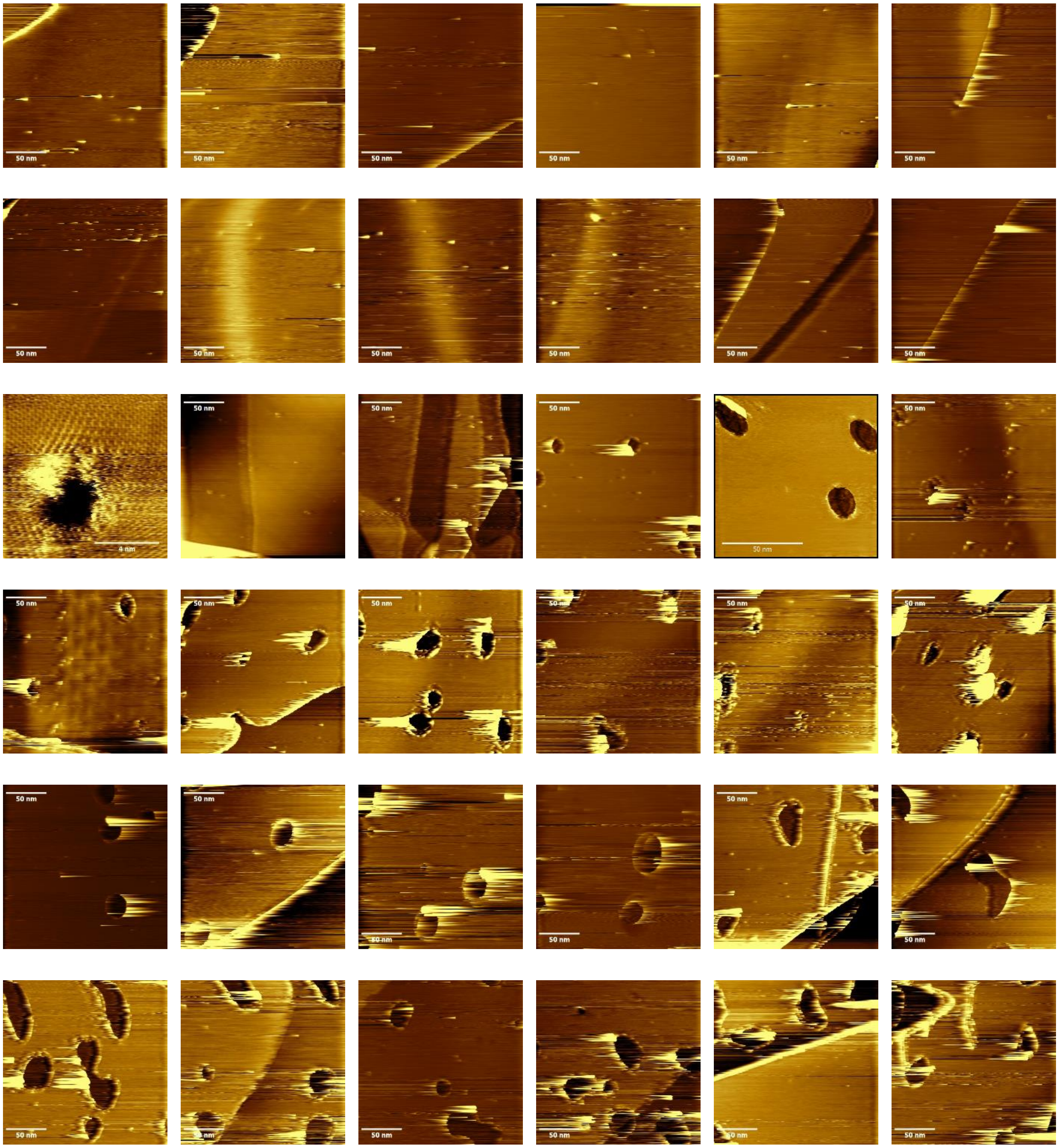

The first set of 36 images used in the middle graph in **Figure 4-5, Figure 4-6,** and the second row of **Table 4-1.**

**Figure A1-10 cont.**

Filenames from top left to bottom right:

Directory: Appendix\A1-10\ 1100C, 0.4eV Beam Trial 1, 3.5hrs
091616_0001
091616_0003
091616_0006
091616_0007
091616_0008
091616_0009
091916_0001
091916_0002
091916_0003
091916_0004
091916_0006
091916_0008
091916_0015
091916_0018
091916_0030

Directory: Appendix\A1-10\ 1100C, 0.4eV Beam Trial 1, 7hrs
092116_0033
092116_0034
092116_0045
092116_0047

Directory: Appendix\A1-10\ 1100C, 0.4eV Beam Trial 1, 9.5hrs
092216_0001
092216_0002
092216_0005
092216_0006
092216_0008
092216_0009
092216_0011
092216_0012
092216_0013
092316_0001
092316_0002
092316_0003
092316_0004
092316_0005
092316_0006
092316_0009
092316_0010

**Figure A1-11**

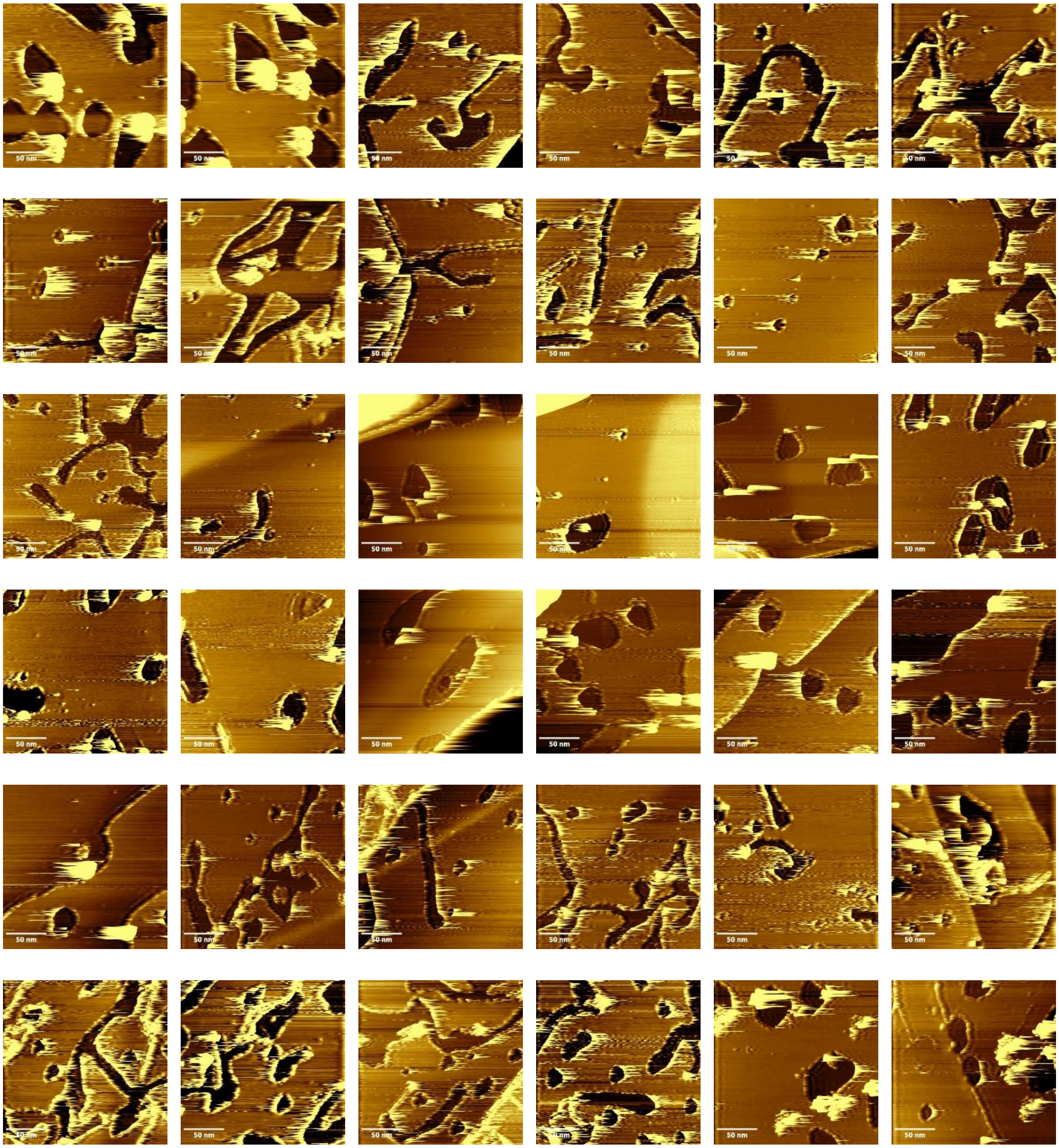

The second set of 36 images used in the middle graph in **Figure 4-5, Figure 4-6,** and the second row of **Table 4-1.**

**Figure A1-11 cont.**

Filenames from top left to bottom right:

Directory: Appendix\A1-11\ 1100C, 0.4eV Beam Trial 1, 14hrs
092616_0005
092616_0006
092716_0001
092716_0002
092716_0003
092716_0004
092716_0010
092716_0011
092716_0014
092716_0015
092716_0016
092716_0017
092716_0018
092716_0019
092716_0021
092716_0022
092716_0023
092716_0025
092716_0026
092716_0027
092716_0028
092816_0001
092816_0002
092816_0003
092816_0004
092816_0020
092816_0021
092816_0022
092916_0001
092916_0002
092916_0003
092916_0004
092916_0005
092916_0006

Directory: Appendix\A1-11\ 1100C, 0.4eV Beam Trial 1, 17.5hrs
093016_0006
093016_0007

## Figure A1-12

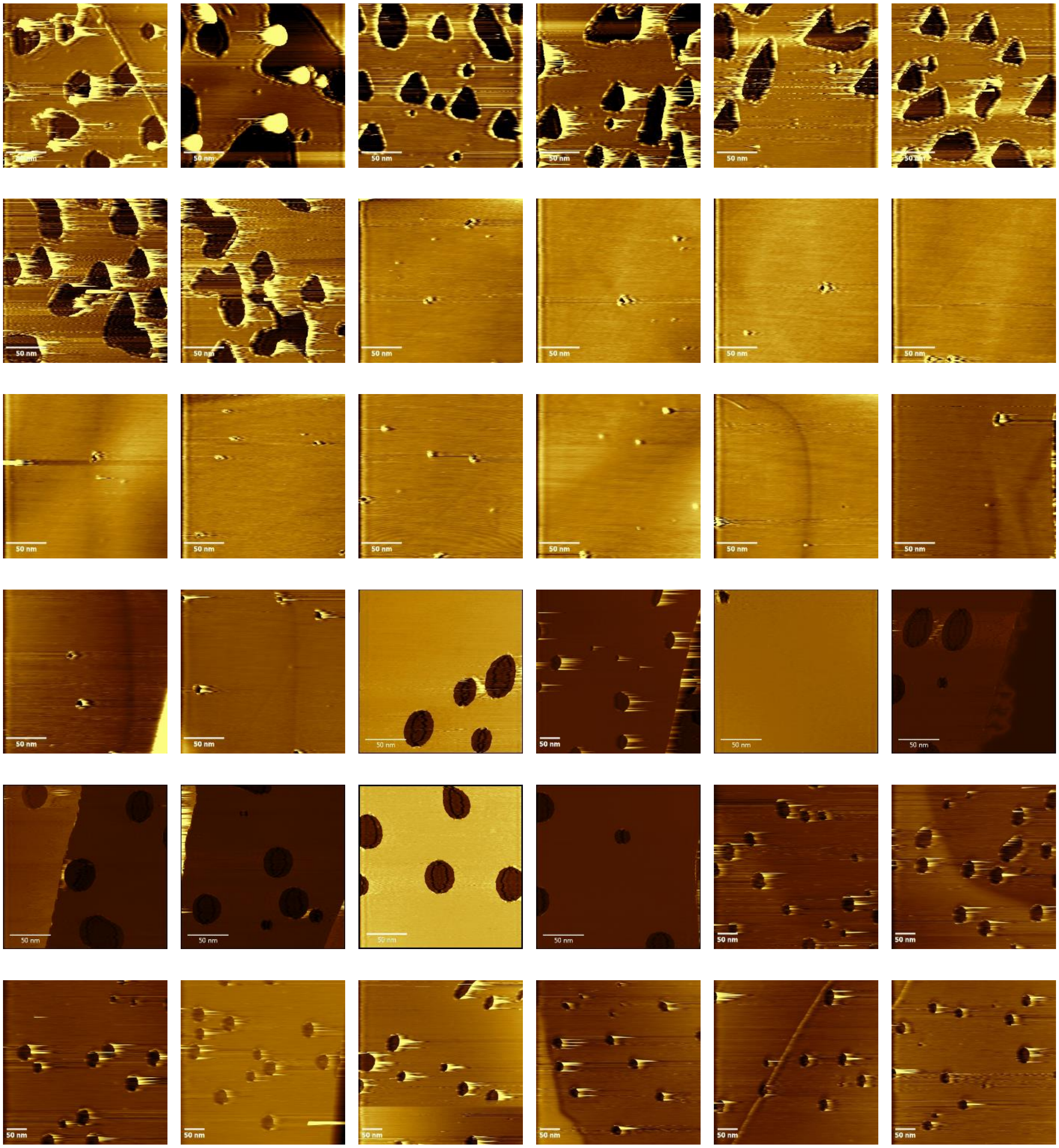

The third set of 36 images used in the middle graph in **Figure 4-5, Figure 4-6,** and the second row of **Table 4-1.**

**Figure A1-12 cont.**

Filenames from top left to bottom right:

Directory: Appendix\A1-12\ 1100C, 0.4eV Beam Trial 1, 17.5hrs
093016_0008
093016_0009
093016_0022
093016_0023
093016_0024
093016_0025
093016_0026
093016_0027

Directory: Appendix\A1-12\ 1100C, 0.4eV Beam Trial 2, 3.5hrs
012717_0001
012717_0006
012717_0009
012717_0011
012717_0013
012717_0015
012717_0018
012717_0021
012717_0022
012717_0024
012717_0028
012717_0030

Directory: Appendix\A1-12\ 1100C, 0.4eV Beam Trial 2, 7hrs
013017_0001
013017_0002
013017_0003
013017_0004
013017_0005
013017_0006
013017_0007
013017_0008
013017_0009
013017_0010
013017_0011
013017_0012
013017_0013
013017_0014
013017_0015
013017_0016

**Figure A1-13**

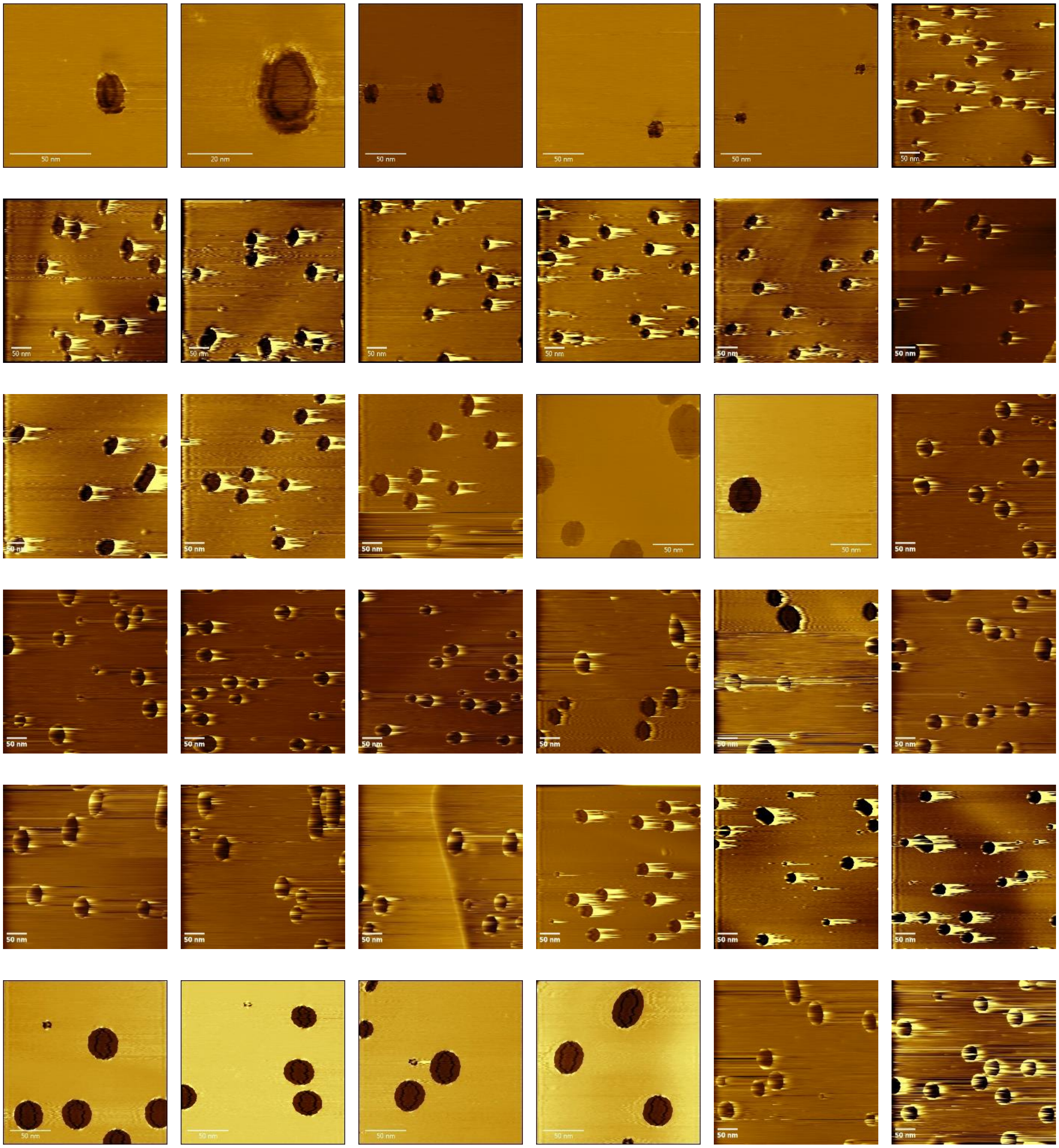

The fourth set of 36 images used in the middle graph in **Figure 4-5, Figure 4-6,** and the second row of **Table 4-1.**

**Figure A1-13 cont.**

Filenames from top left to bottom right:

Directory: Appendix\A1-13\ 1100C, 0.4eV Beam Trial 2, 7hrs
013017_0018
013017_0019
013017_0020
013017_0021
013017_0022

Directory: Appendix\A1-13\ 1100C, 0.4eV Beam Trial 2, 10.5hrs
013117_0008
013117_0009
013117_0010
013117_0011
013117_0012
020117_0001
020117_0002
020117_0003
020117_0004
020117_0005
020117_0007
020117_0008

Directory: Appendix\A1-13\ 1100C, 0.4eV Beam Trial 2, 14hrs
020117_0009
020117_0010
020117_0011
020117_0012
020117_0013
020117_0014
020117_0015
020117_0016
020117_0017
020117_0018
020217_0001
020217_0002
020217_0003
020217_0004
020217_0005
020217_0006
020217_0007

**Figure A1-13 cont.**

Directory: Appendix\A1-13\ 1100C, 0.4eV Beam Trial 2, 14hrs
020217_0014
020217_0015

## Figure A1-14

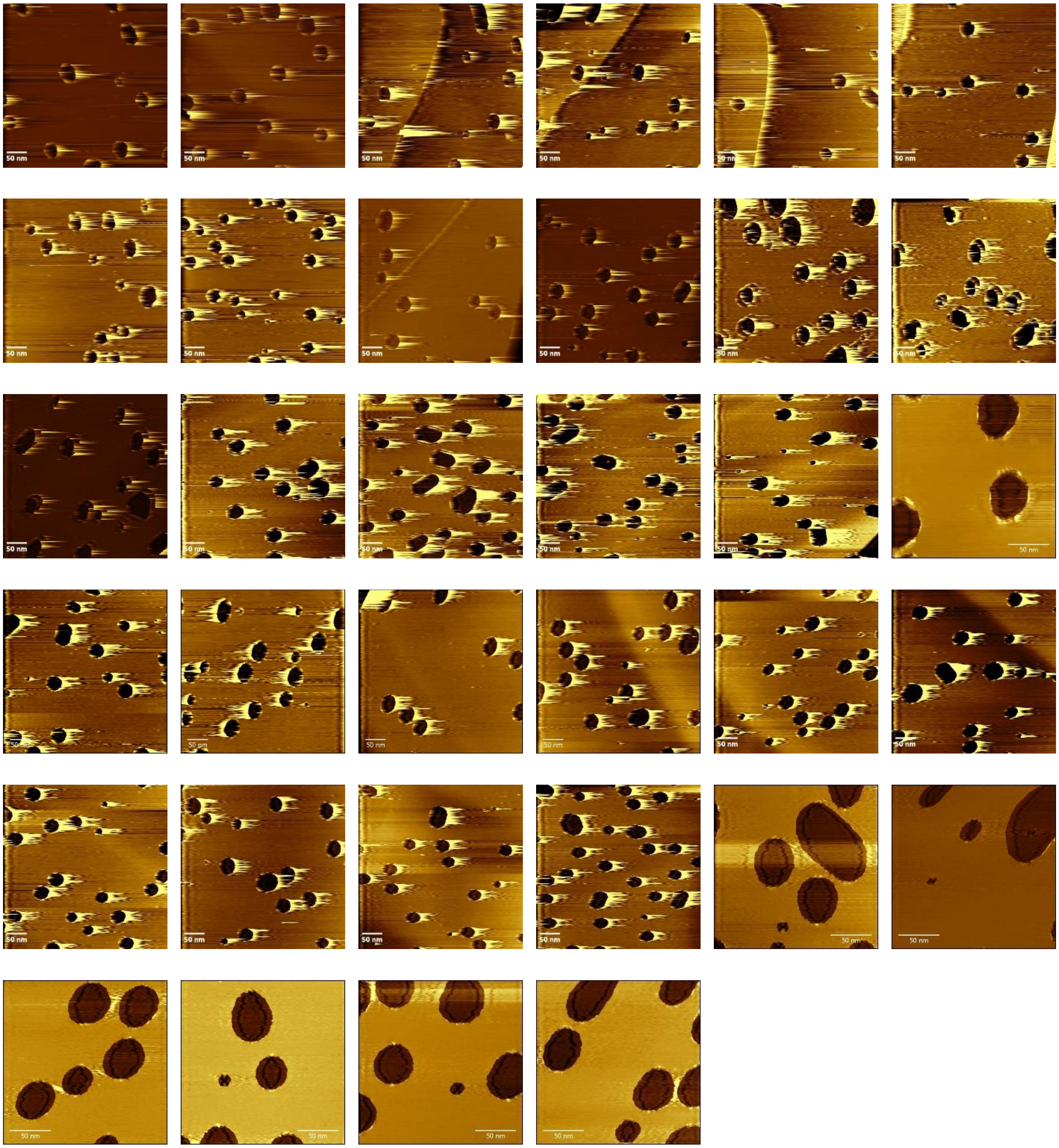

The final set of 34 images used in the middle graph in **Figure 4-5, Figure 4-6,** and the second row of **Table 4-1.**

**Figure A1-14 cont.**

Filenames from top left to bottom right:

Directory: Appendix\A1-14\ 1100C, 0.4eV Beam Trial 2, 17.5hrs
020217_0016
020217_0017
020317_0001
020317_0002
020317_0003
020317_0004
020317_0005
020317_0006
020317_0007
020317_0008
020317_0009
020317_0010
020317_0011
020317_0012
020317_0013
020317_0014
020317_0015
020317_0017

Directory: Appendix\A1-14\ 1100C, 0.4eV Beam Trial 2, 21hrs
020617_0018
020617_0019
020617_0020
020617_0021
020617_0022
020617_0023
020617_0024
020617_0025
020617_0026
020617_0027
020617_0028
020717_0001
020717_0002
020717_0003
020717_0004
020717_0005
020717_0006

## Figure A1-15

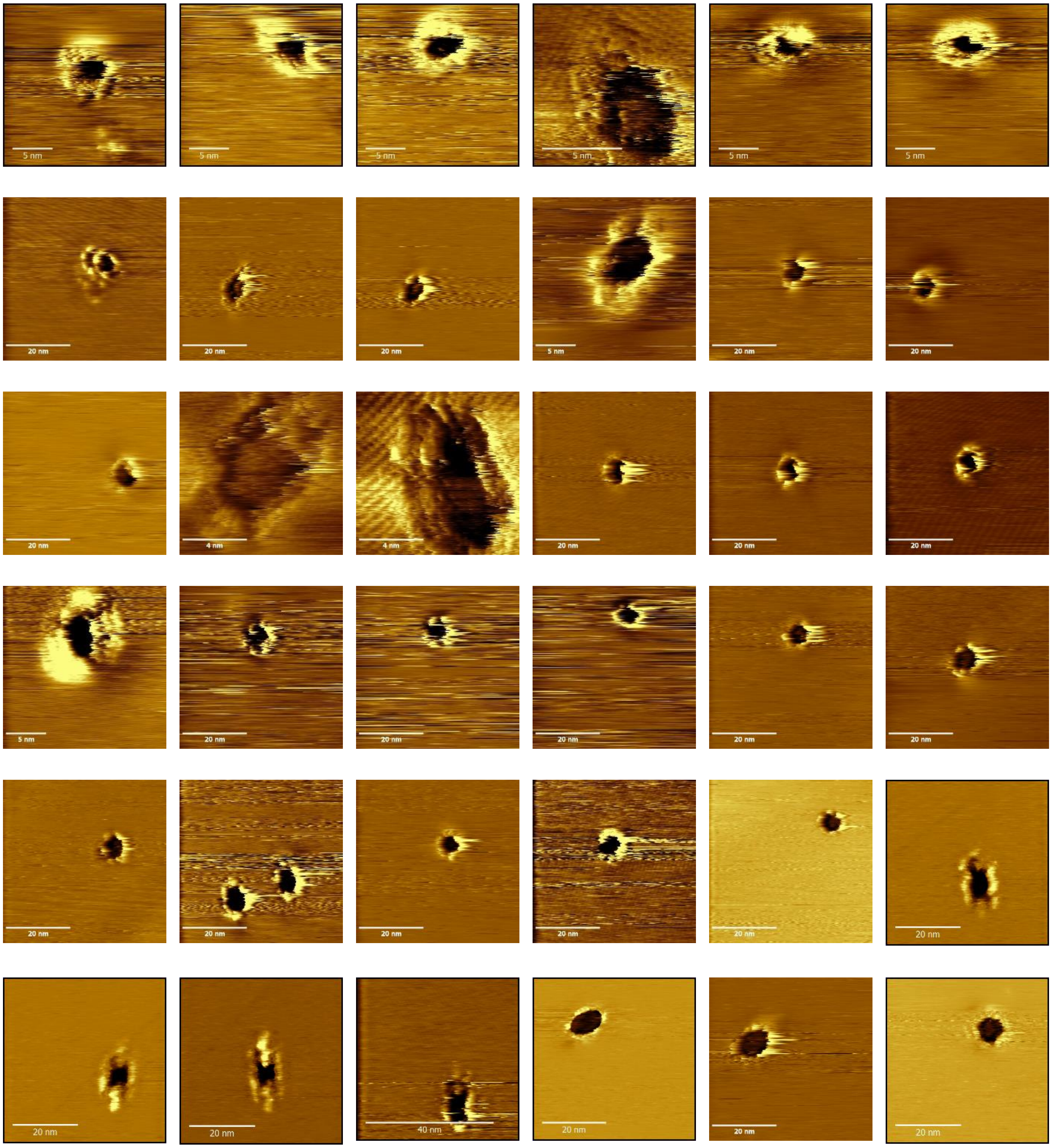

The first set of 36 images used in the bottom graph in **Figure 4-5** and the third row of **Table 4-1.**

**Figure A1-15 cont.**

Filenames from top left to bottom right:

Directory: Appendix\A1-15\ 1200C, 0.4eV Beam, 3hrs
080817_0007
080817_0008
080817_0009
080817_0010
080817_0011
080817_0012

Directory: Appendix\A1-15\ 1200C, 0.4eV Beam, 6hrs
080917_0002
080917_0004
080917_0005
080917_0006
080917_0007
080917_0008
080917_0009
080917_0014
080917_0015
080917_0016
080917_0018
080917_0019
080917_0020

Directory: Appendix\A1-15\ 1200C, 0.4eV Beam, 9hrs
081017_0000
081017_0001
081017_0002
081017_0003
081017_0004
081017_0005
081017_0006
081017_0007
081017_0008
081017_0009

Directory: Appendix\A1-15\ 1200C, 0.4eV Beam, 9hrs
081117_0002
081117_0003
081117_0005
081117_0007

**Figure A1-15 cont.**

081117_0008
081117_0009
081117_0010

## Figure A1-16

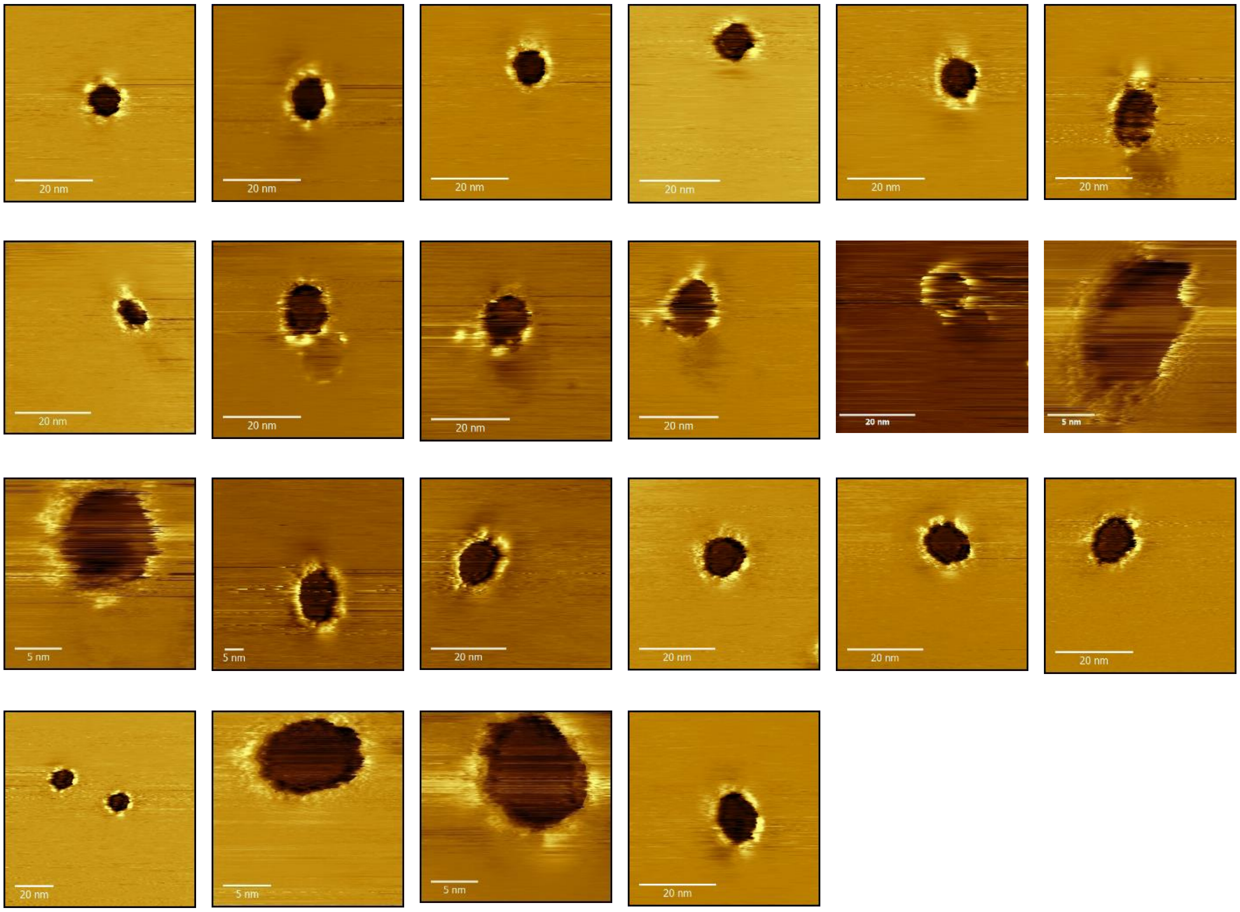

The final 22 images used in the bottom graph in **Figure 4-5** and the third row of **Table 4-1.**

**Figure A1-16 cont.**

Filenames from top left to bottom right:

Directory: Appendix\A1-16\1200C, 0.4eV Beam, 15hrs
081117_0012
081117_0014
081117_0015
081117_0017
081117_0019

Directory: Appendix\A1-16\1200C, 0.4eV Beam, 24hrs
081417_0001
081417_0002
081417_0003
081417_0004
081417_0005
081417_0007
081417_0009
081417_0010
081417_0011
081417_0012
081417_0013
081417_0015
081417_0016
081417_0018
081417_0020
081417_0021
081417_0022

**Figure A1-17**

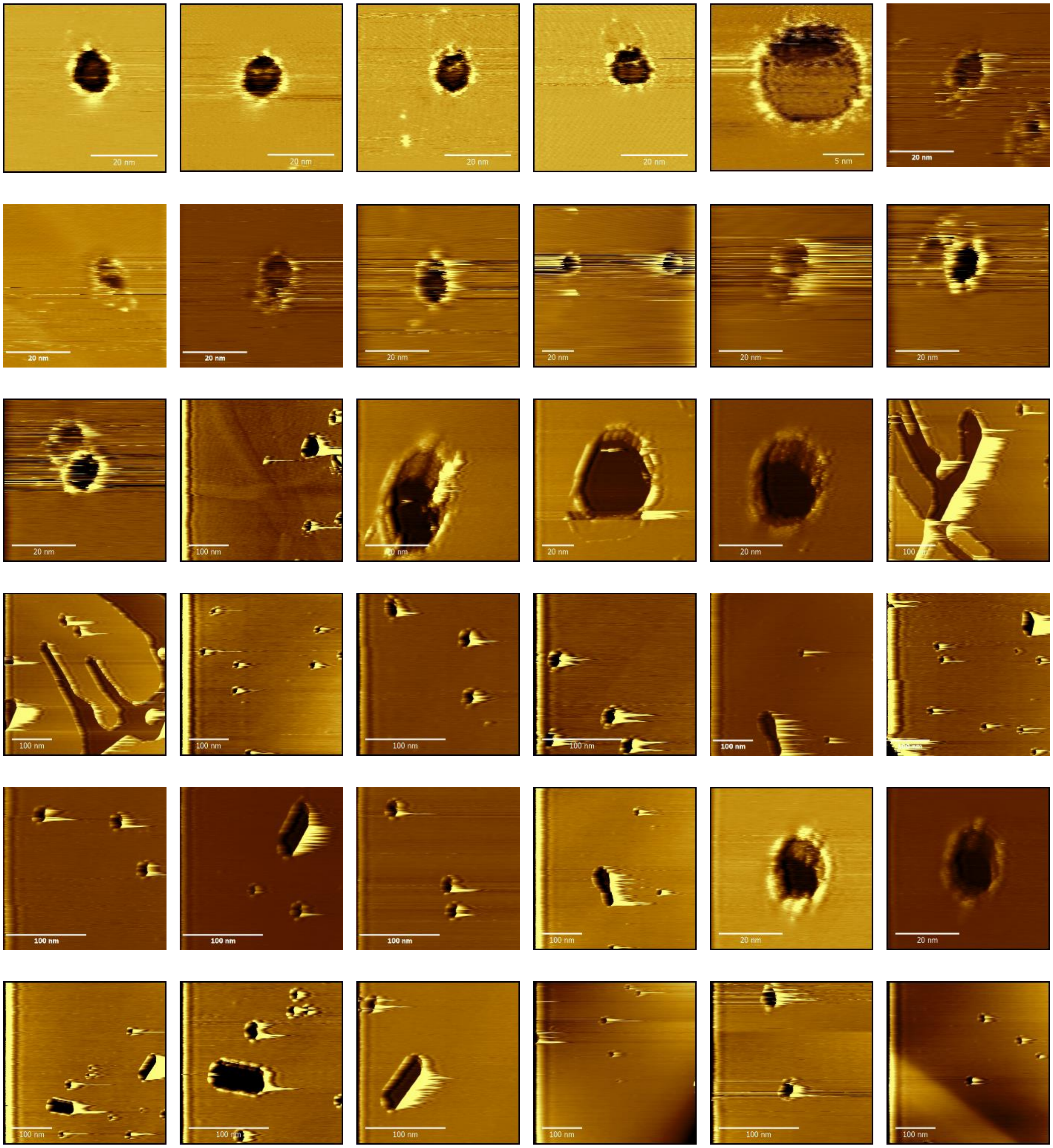

The first set of 36 images used in the fourth row of **Table 4-1.**

**Figure A1-17 cont.**

Filenames from top left to bottom right:

Directory: Appendix\A1-17\ 45 Degree, 1100C, 0.4eV Beam, 12hrs
051517_0008
051517_0009
051517_0011
051517_0012
051517_0013
053117_0001
053117_0003
053117_0004
053117_0006
053117_0007
053117_0008
053117_0009
053117_0010

Directory: Appendix\A1-17\ 45 Degree, 1100C, 0.4eV Beam, 16hrs
060117_0027
060117_0028
060117_0029
060117_0030
060117_0031
060117_0032
060217_0001
060217_0002
060217_0003
060217_0004
060217_0005
060217_0006
060217_0007
060217_0011
060217_0012
060217_0014
060217_0015
060217_0016
060217_0017
060217_0018
060217_0021
060217_0022
060217_0024

**Figure A1-18**

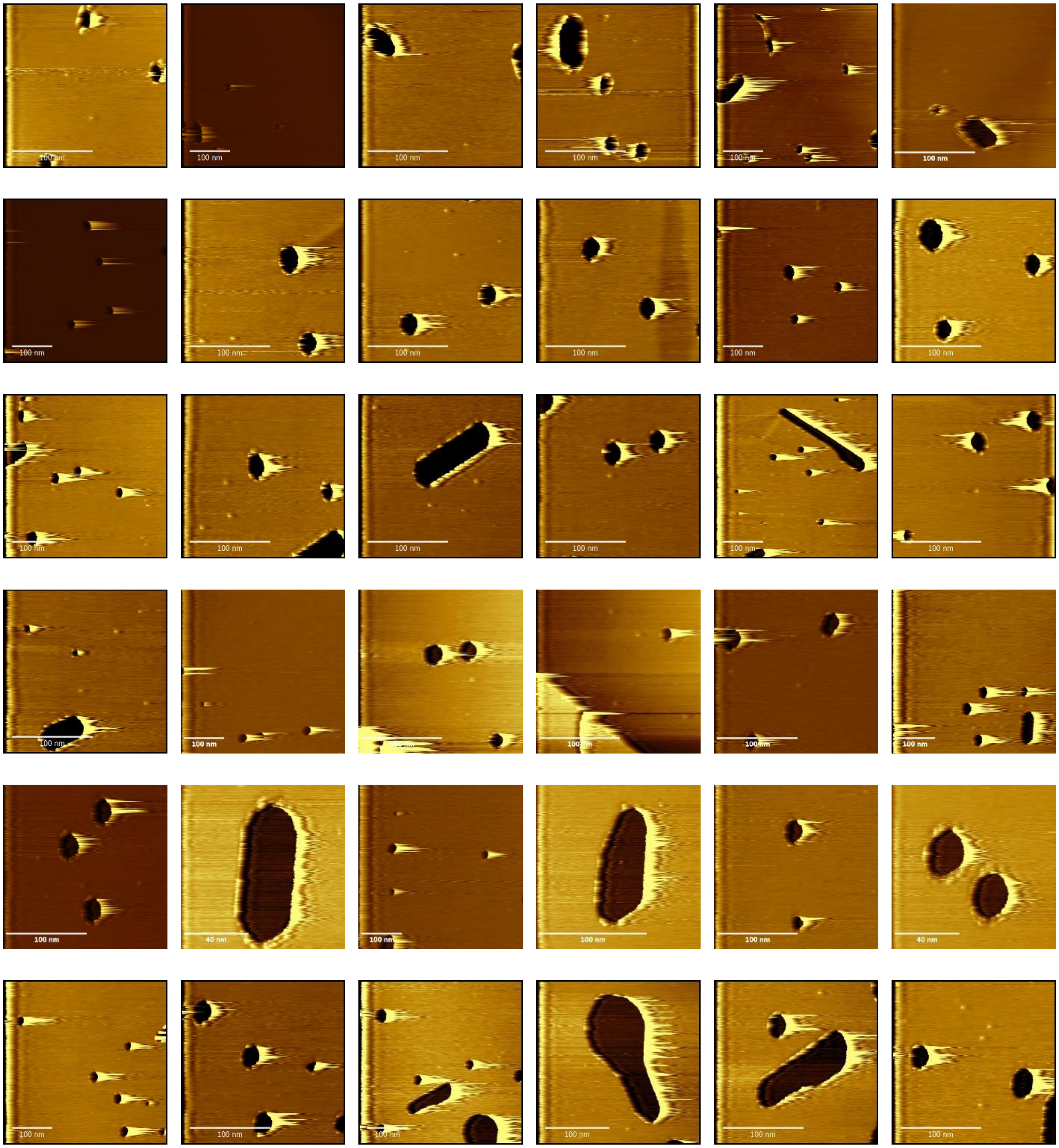

The second set of 36 images used in the fourth row of **Table 4-1.**

**Figure A1-18 cont.**

Filenames from top left to bottom right:

Directory: Appendix\ A1-18\ 45 Degree, 1100C, 0.4eV Beam, 16hrs
060217_0025
060217_0026
060217_0027
060217_0028
060217_0029
060217_0030

Directory: Appendix\ A1-18\ 45 Degree, 1100C, 0.4eV Beam, 19hrs
060317_0001
060317_0002
060317_0003
060317_0004
060317_0005
060317_0006
060317_0007
060317_0008
060317_0009
060317_0010
060317_0011
060317_0012
060317_0013
060317_0014
060517_0001
060517_0002
060517_0003
060517_0004
060517_0005
060517_0008
060517_0009
060517_0010
060517_0011
060517_0012
060517_0013
060517_0014
060517_0015
060517_0017
060517_0018
060517_0019

## Figure A1-19

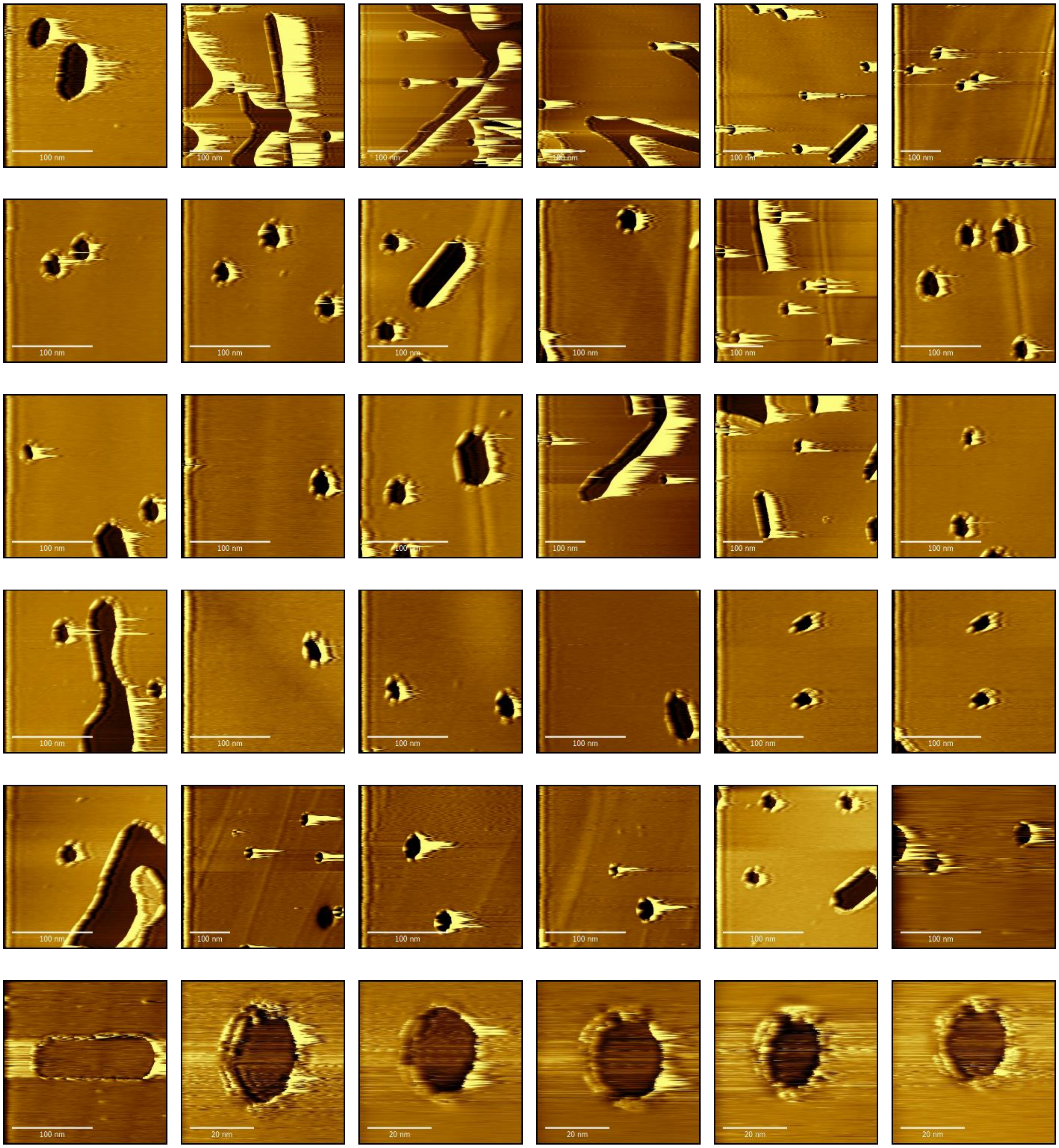

The third set of 36 images used in the fourth row of **Table 4-1.**

**Figure A1-19 cont.**

Filenames from top left to bottom right:

Directory: Appendix\ A1-19\ 45 Degree, 1100C, 0.4eV Beam, 19hrs
060517_0020

Directory: Appendix\ A1-19\ 45 Degree, 1100C, 0.4eV Beam, 22hrs
060517_0021
060517_0022
060517_0023
060517_0024
060517_0025
060517_0026
060517_0027
060517_0028
060517_0029
060517_0030
060517_0031
060517_0032
060517_0033
060517_0034
060517_0035
060517_0036
060517_0037
060517_0038
060517_0039
060517_0040
060517_0041
060517_0042
060517_0043
060517_0044
060517_0045
060517_0046
060517_0047
060517_0048
060617_0001
060617_0002
060617_0003
060617_0004
060617_0005
060617_0006
060617_0007

## Figure A1-20

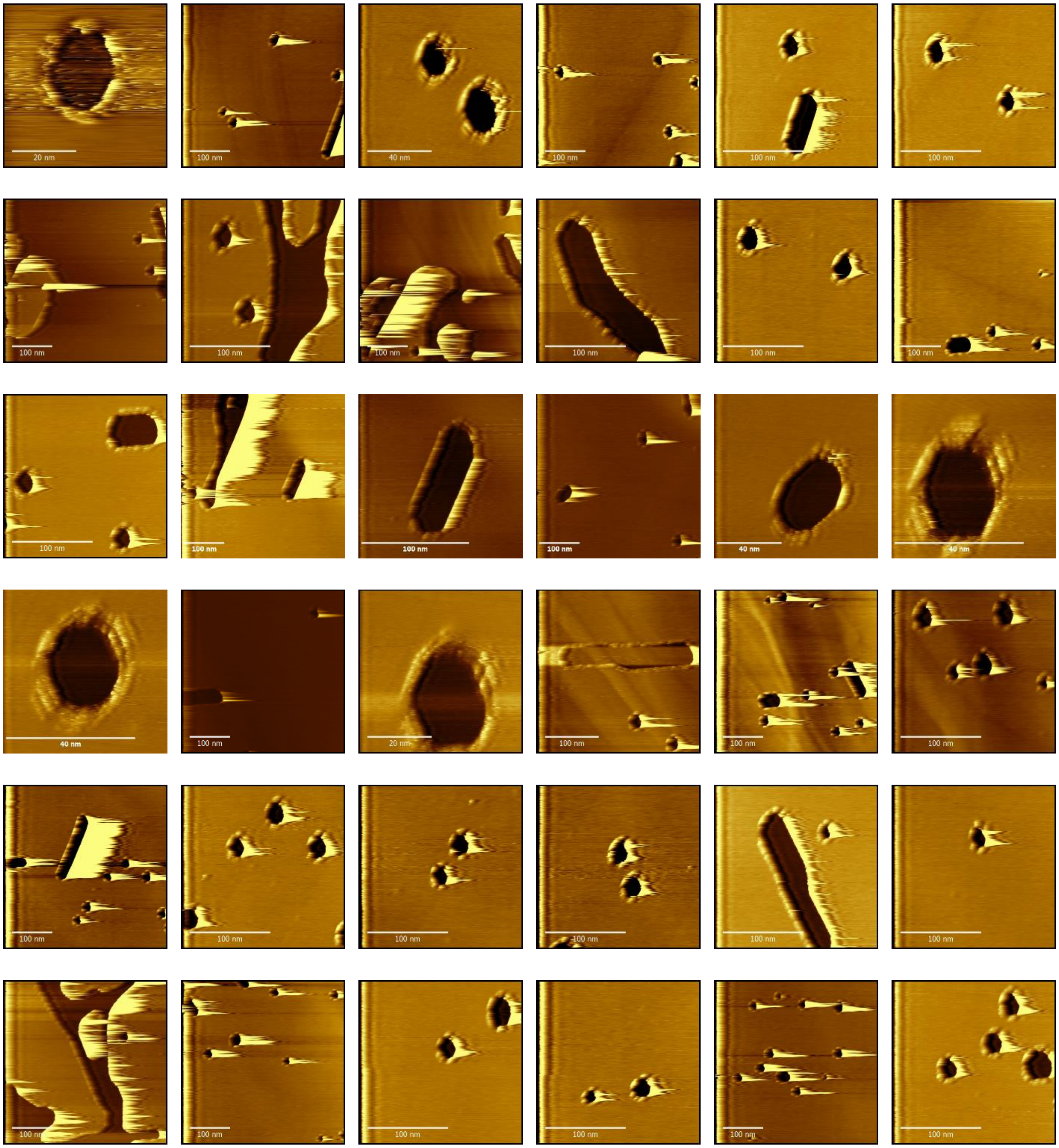

The fourth set of 36 images used in the fourth row of **Table 4-1.**

**Figure A1-20 cont.**

Filenames from top left to bottom right:

Directory: Appendix\ A1-20\ 45 Degree, 1100C, 0.4eV Beam, 22hrs
060617_0008

Directory: Appendix\ A1-20\ 45 Degree, 1100C, 0.4eV Beam, 26hrs
060617_0009
060617_0010
060617_0013
060617_0014
060617_0015
060717_0001
060717_0002
060717_0003
060717_0004
060717_0005
060717_0006
060717_0007
060717_0008
060717_0009
060717_0010
060717_0011
060717_0012
060717_0013
060717_0014
060717_0015
060717_0016
060717_0017
060717_0018
060717_0019
060717_0020
060717_0021
060717_0022
060717_0023
060717_0024
060717_0025
060717_0026
060717_0027
060717_0028
060717_0029
060717_0030

**Figure A1-21**

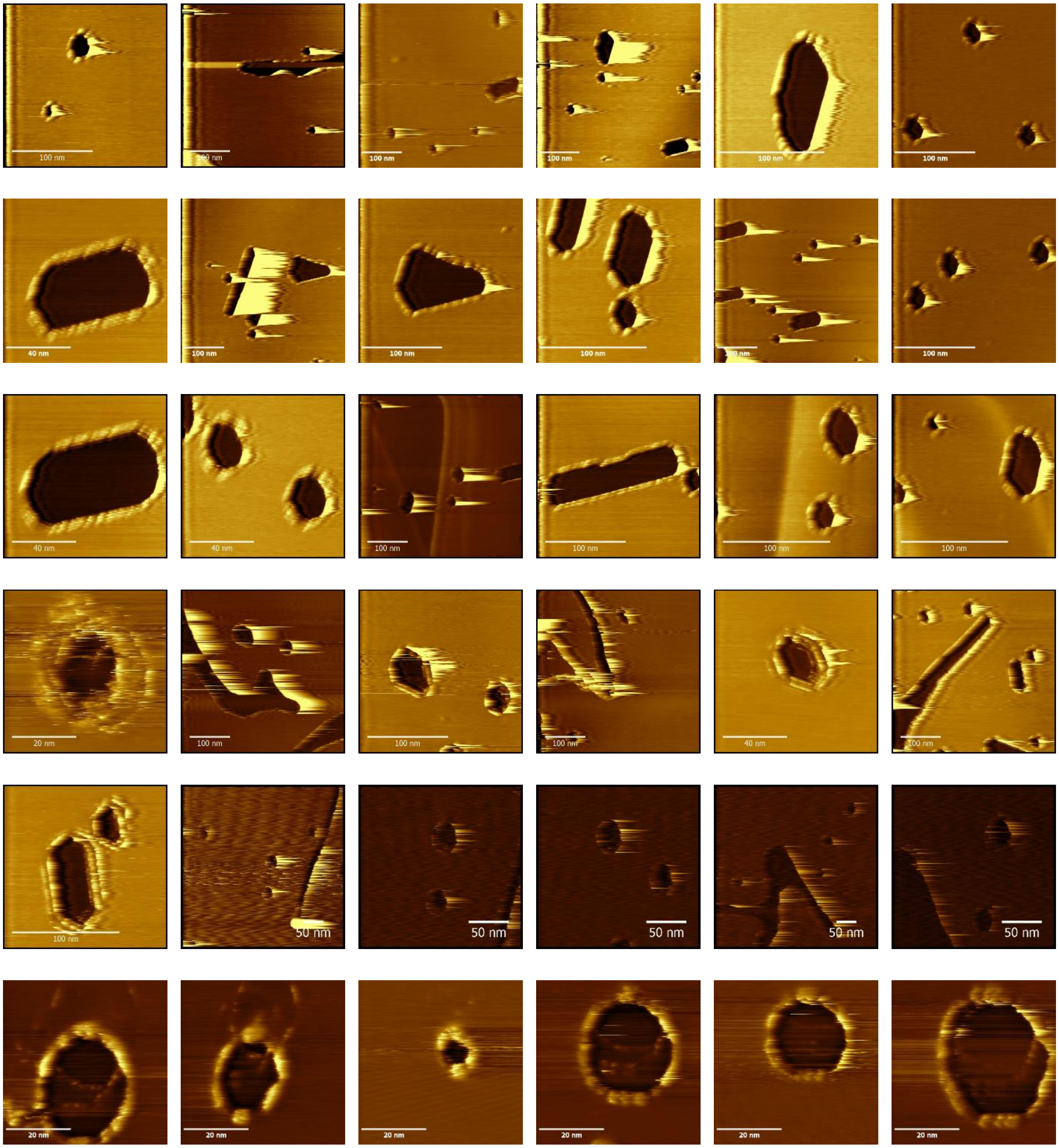

The fifth set of 36 images used in the fourth row of **Table 4-1.**

**Figure A1-21 cont.**

Filenames from top left to bottom right:

Directory: Appendix\ A1-21\ 45 Degree, 1100C, 0.4eV Beam, 26hrs
060717_0031
060717_0032
060717_0033
060717_0035
060717_0036
060717_0037
060717_0038
060717_0039
060717_0040
060717_0041
060717_0042
060717_0043
060717_0044
060717_0045
060717_0046
060717_0047
060717_0048
060717_0049

Directory: Appendix\ A1-21\ 45 Degree, 1100C, 0.4eV Beam, 31hrs
060817_0002
060817_0003
060817_0004
060817_0005
060817_0006
060817_0007
060817_0008
061217_0001
061217_0002
061217_0003
061217_0004
061217_0005
061217_0006
061217_0007
061217_0008
061217_0009
061217_0010
061217_0011

**Figure A1-22**

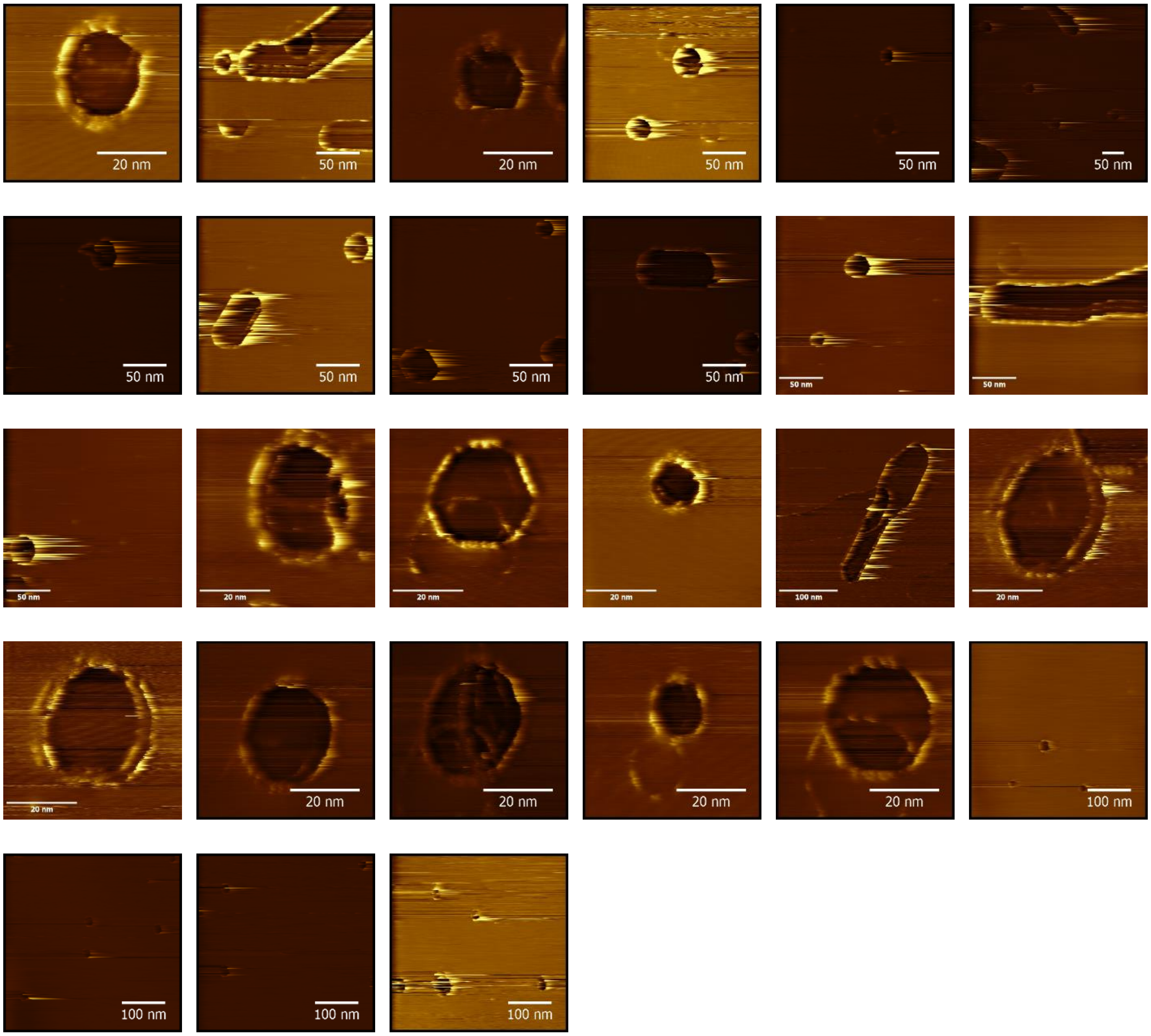

The sixth set of 36 images used in the fourth row of **Table 4-1.**

**Figure A1-22 cont.**

Filenames from top left to bottom right:

Directory: Appendix\ A1-22\ 45 Degree, 1100C, 0.4eV Beam, 31hrs
061217_0013
061217_0015
061217_0016
061217_0018
061217_0019
061217_0020
061217_0021
061217_0022
061217_0023
061217_0024
061217_0026
061217_0030
061217_0032
061217_0033
061217_0034
061217_0036
061217_0037
061217_0039
061217_0040
061217_0042
061217_0043
061217_0044
061217_0045
061317_0001
061317_0002
061317_0003
061317_0004

**Figure A1-23**

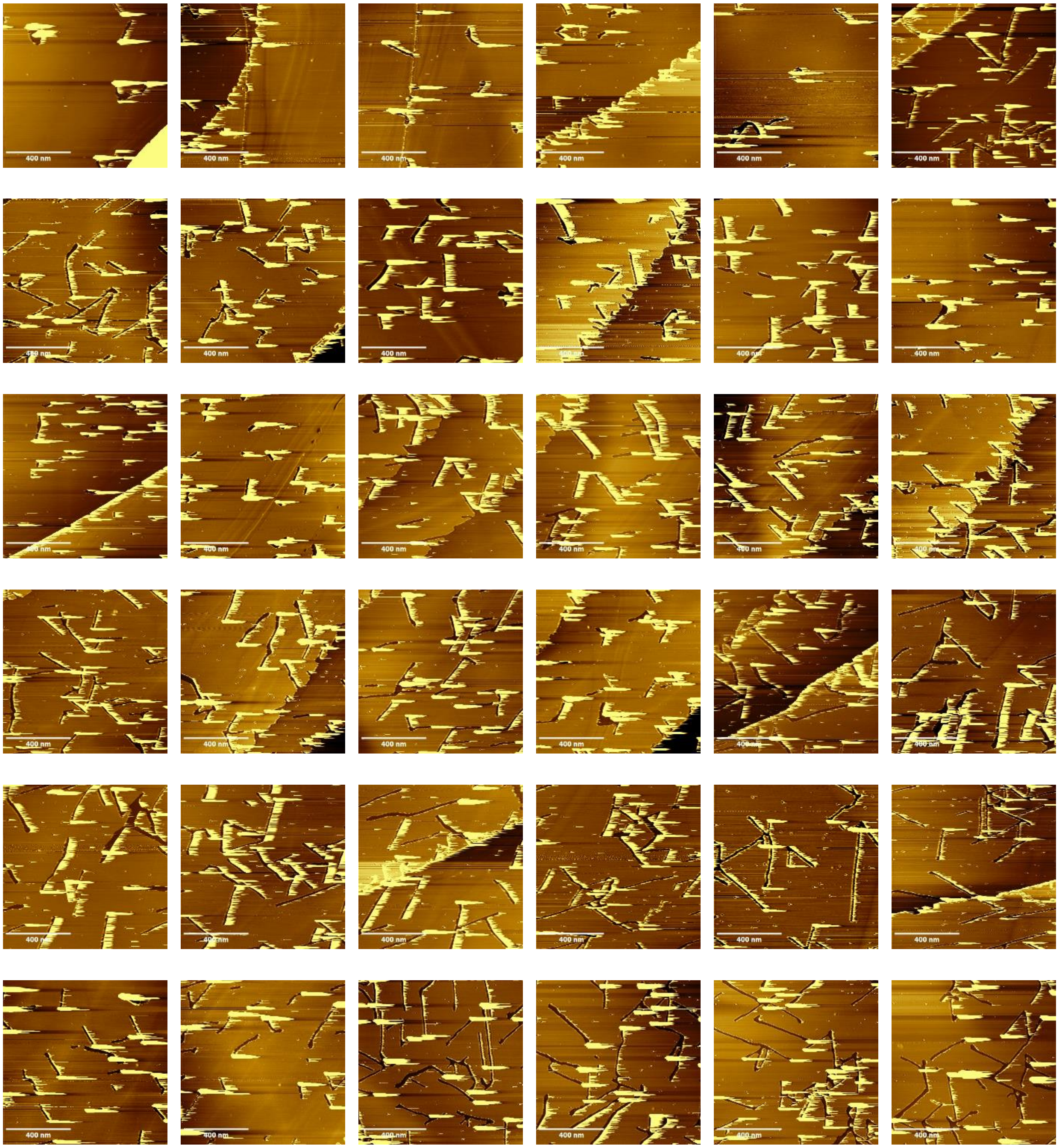

The first set of 36 images used in the fifth row of **Table 4-1.**

**Figure A1-23 cont.**

Filenames from top left to bottom right:

Directory: Appendix\ A1-22\ 1000C, 0.7eV Beam, 2.5hrs
110617_0001
110617_0002
110617_0003
110617_0004
110617_0005
110617_0007
110617_0008

Directory: Appendix\ A1-22\ 1000C, 0.7eV Beam, 3.5hrs
110717_0001
110717_0002
110717_0003
110717_0004
110717_0005
110717_0006
110717_0007
110717_0008
110717_0009
110717_0010
110717_0011
110717_0012
110717_0013
110717_0014

Directory: Appendix\ A1-22\ 1000C, 0.7eV Beam, 5.5hrs
110817_0001
110817_0002
110817_0003
110817_0004
110817_0005
110817_0006
110817_0007
110817_0008
110817_0009
110817_0011
110817_0012

Directory: Appendix\ A1-22\ 1000C, 0.7eV Beam, 8.5hrs
110917_0001
110917_0002

**Figure A1-23 cont.**

110917_0003
110917_0004

**Figure A1-24**

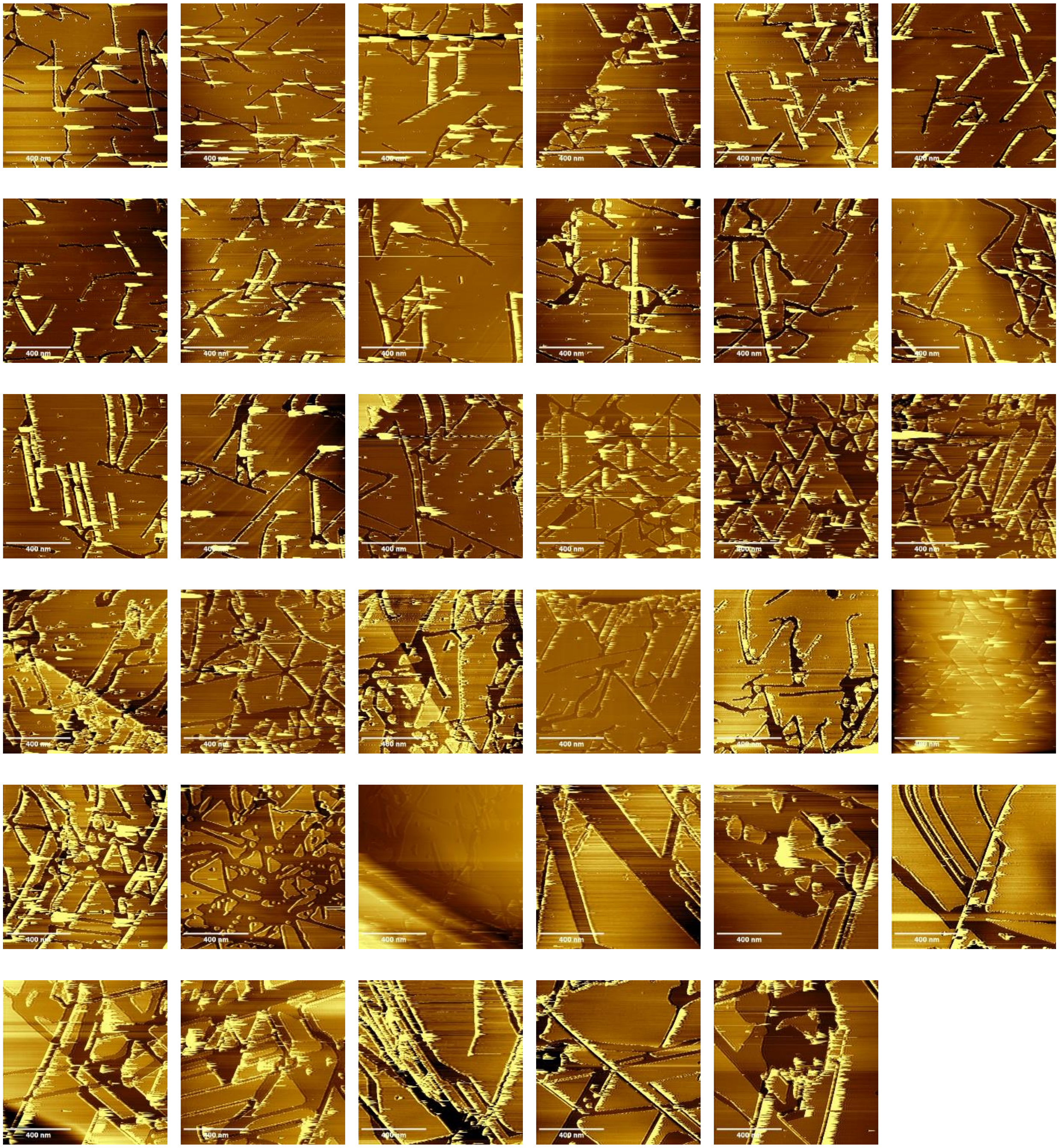

The second set of 36 images used in the fifth row of **Table 4-1.**

**Figure A1-24 cont.**

Filenames from top left to bottom right:

Directory: Appendix\ A1-23\ 1000C, 0.7eV Beam, 8.5hrs
110917_0005
110917_0006
110917_0007
110917_0010
110917_0011
110917_0012
110917_0013
110917_0014

Directory: Appendix\ A1-23\ 1000C, 0.7eV Beam, 13.5hrs
111017_0001
111017_0002
111017_0003
111017_0004
111017_0005
111017_0006
111017_0007
111017_0008
111317_0001
111317_0002
111317_0003
111317_0004
111317_0005
111317_0006
111317_0007
111317_0008

Directory: Appendix\ A1-23\ 1000C, 0.7eV Beam, 18.5hrs
111417_0001
111417_0007
111417_0008
111517_0001
111517_0002
111517_0003
111517_0004
111517_0005
111517_0006
111517_0007
111517_0008

**Figure A1-25**

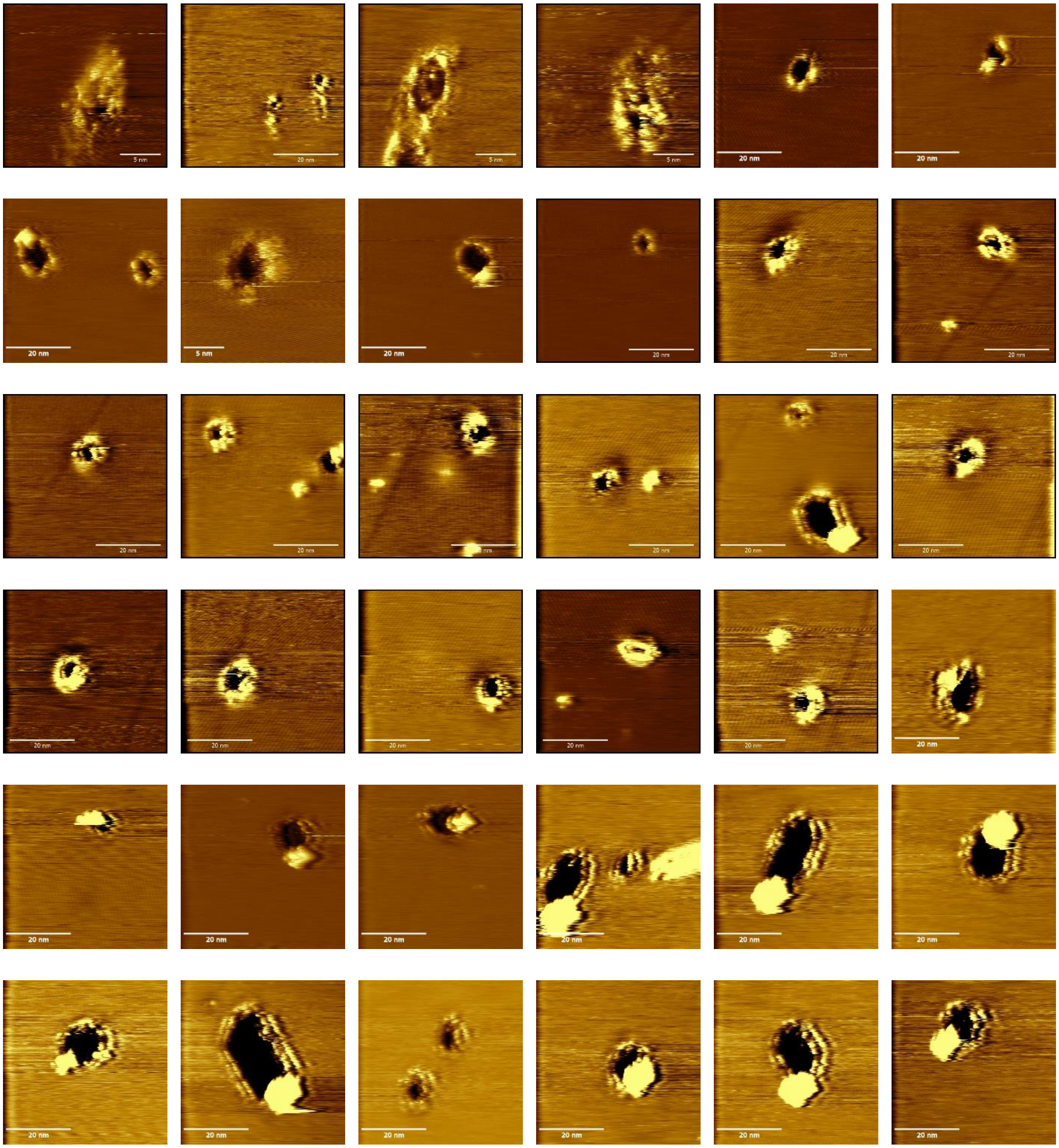

The first set of 36 images used in **Figure 4-6** and the sixth row of **Table 4-1.**

**Figure A1-25 cont.**

Filenames from top left to bottom right:

Directory: Appendix\A1-25\1100C, 0.7eV Beam Trial 2, 30min
072117_0004
072117_0005
072117_0008
072117_0009

Directory: Appendix\A1-25\1100C, 0.7eV Beam Trial 2, 60min
072117_0011
072117_0012
072117_0013
072117_0014
072117_0015
072117_0016
072317_0001
072317_0002
072317_0003
072317_0005
072317_0006
072317_0008
072317_0010
072317_0011
072317_0012
072317_0014
072317_0015
072317_0016
072317_0017

Directory: Appendix\A1-25\1100C, 0.7eV Beam Trial 2, 90min
072417_0002
072417_0003
072417_0005
072417_0006
072417_0007
072417_0009
072417_0010
072417_0012
072417_0014
072417_0015
072417_0016
072417_0018

**Figure A1-25 cont.**

072417_0019

## Figure A1-26

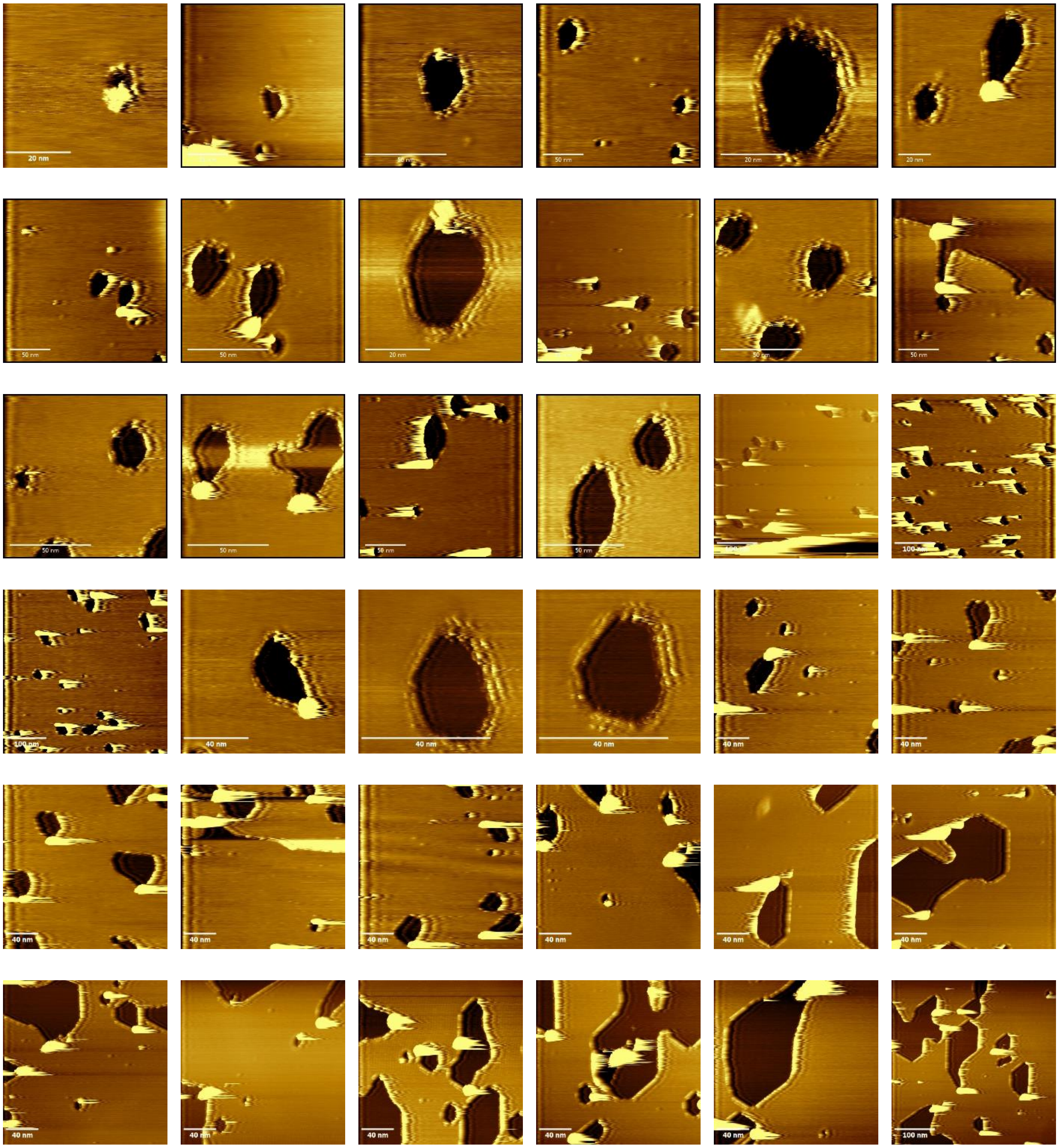

The second set of 36 images used in **Figure 4-6** and the sixth row of **Table 4-1.**

**Figure A1-26 cont.**

Filenames from top left to bottom right:

Directory: Appendix\A1-26\1100C, 0.7eV Beam Trial 2, 90min
072417_0021
072417_0022
072417_0023
072417_0024
072417_0025
072417_0026
072417_0027
072417_0028
072417_0029
072417_0030
072417_0031
072417_0032
072417_0033
072417_0034
072417_0035
072417_0036
072417_0037
072417_0038
072417_0039
072417_0040
072417_0041
072417_0042
072417_0043
072417_0044
072417_0045
072417_0046
072417_0047

Directory: Appendix\A1-26\1100C, 0.7eV Beam Trial 2, 120min
072517_0006
072517_0007
072517_0008
072517_0009
072517_0010
072517_0013
072517_0014
072517_0016
072517_0017

## Figure A1-27

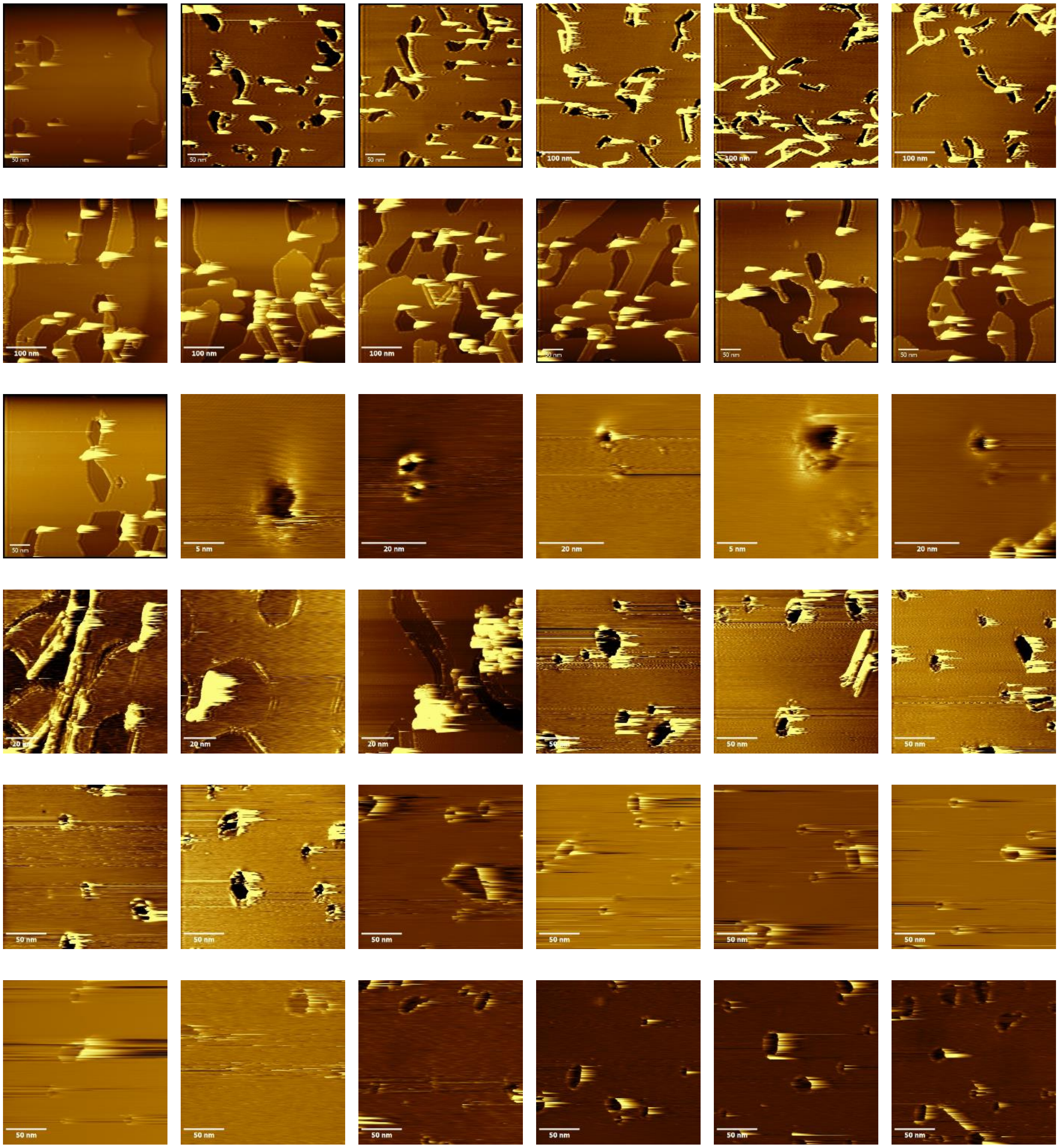

The third set of 36 images used in **Figure 4-6** and the sixth row of **Table 4-1.**

**Figure A1-27 cont.**

Filenames from top left to bottom right:

Directory: Appendix\A1-27\1100C, 0.7eV Beam Trial 2, 120min
072517_0018
072517_0020
072517_0021

Directory: Appendix\A1-27\1100C, 0.7eV Beam Trial 2, 150min
072517_0022
072517_0023
072517_0024
072517_0026
072517_0027
072517_0028
072517_0029
072517_0030
072517_0031
072517_0032

Directory: Appendix\A1-27\1100C, 0.7eV Beam Trial 3, 30min
081717_0001
081717_0003
081717_0004
081717_0005
081717_0006

Directory: Appendix\A1-27\1100C, 0.7eV Beam Trial 3, 90min
081817_0001
081817_0002
081817_0003
081817_0004
081817_0005
081817_0006
081817_0007
081817_0008
082117_0004
082117_0006
082117_0008
082117_0009
082117_0011
082117_0013
082117_0014

**Figure A1-27 cont.**

082117_0016
082117_0017
082117_0018

**Figure A1-28**

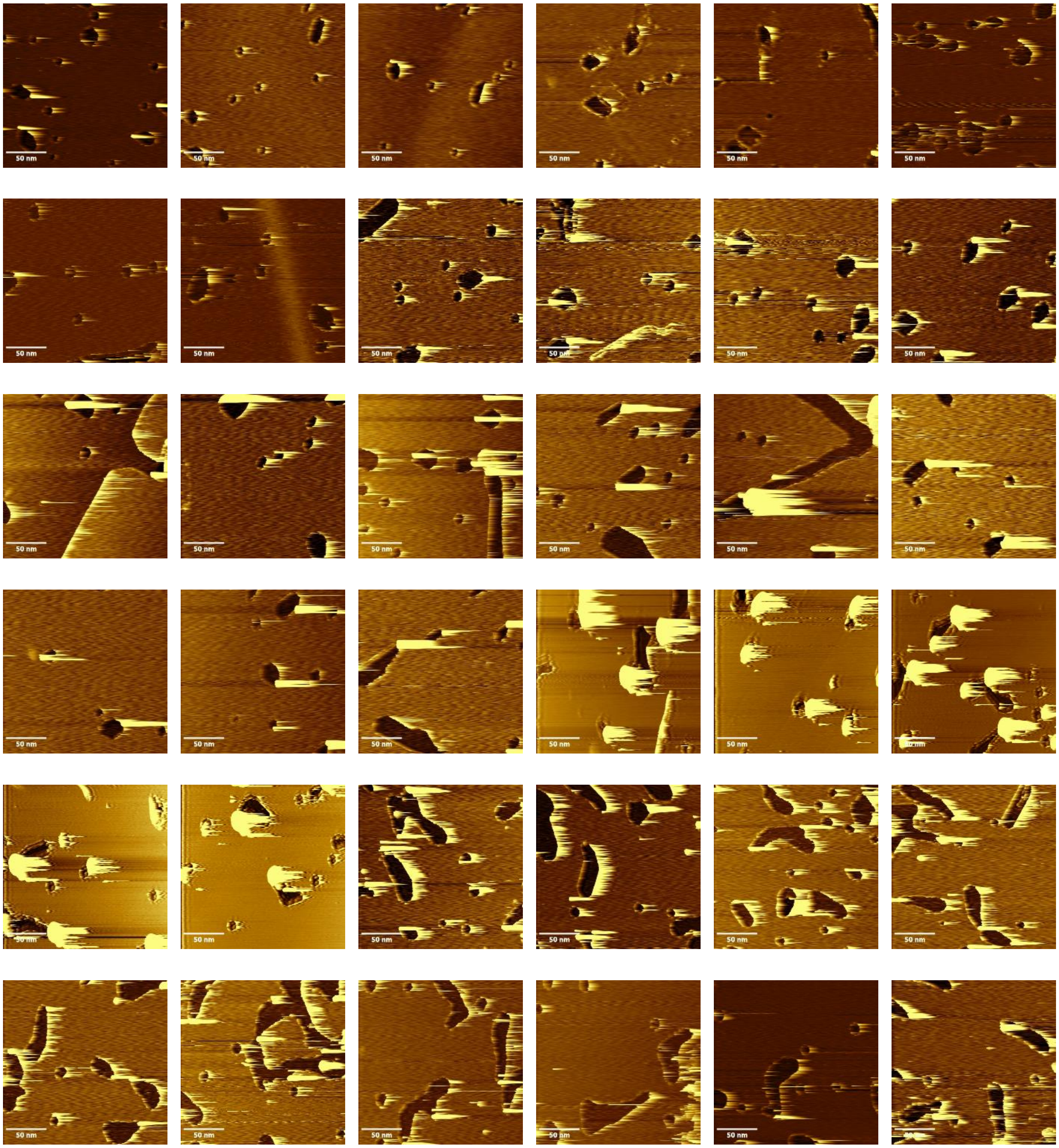

The fourth set of 36 images used in **Figure 4-6** and the sixth row of **Table 4-1.**

**Figure A1-28 cont.**

Filenames from top left to bottom right:

Directory: Appendix\A1-28\1100C, 0.7eV Beam Trial 3, 90min
082117_0019
082117_0020
082117_0021
082117_0022
082117_0023

Directory: Appendix\A1-28\1100C, 0.7eV Beam Trial 3, 105min
082217_0001
082217_0006
082217_0007
082217_0008
082217_0009
082217_0010
082217_0011
082217_0012
082217_0013
082217_0014
082217_0015
082217_0016
082217_0017
082217_0018
082217_0019
082217_0020

Directory: Appendix\A1-28\1100C, 0.7eV Beam Trial 3, 120min
082317_0001
082317_0002
082317_0003
082317_0004
082317_0005
082317_0014
082317_0015
082317_0016
082317_0017
082317_0018
082317_0019
082317_0020
082317_0021
082317_0022

**Figure A1-28 cont.**

082317_0023

**Figure A1-29**

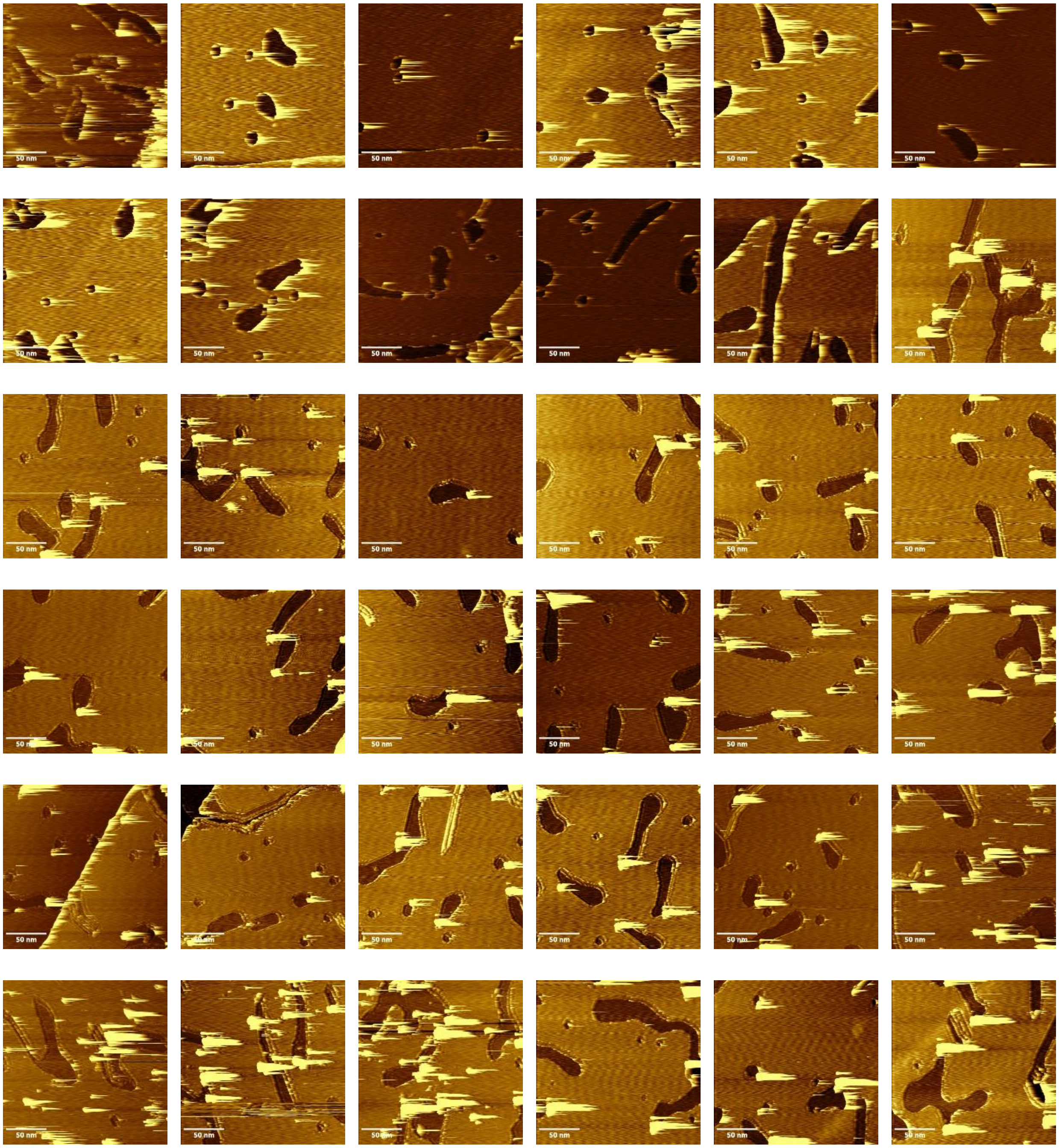

The fifth set of 36 images used in **Figure 4-6** and the sixth row of **Table 4-1.**

**Figure A1-29 cont.**

Filenames from top left to bottom right:

Directory: Appendix\A1-29\1100C, 0.7eV Beam Trial 3, 120min
082317_0024
082317_0025
082317_0026
082317_0027
082317_0028
082317_0029
082317_0030
082317_0031

Directory: Appendix\A1-29\1100C, 0.7eV Beam Trial 3, 135min
082417_0001
082417_0002
082417_0003
082417_0007
082417_0008
082417_0009
082417_0010
082417_0011
082417_0012
082417_0013
082417_0014
082417_0015
082417_0016
082417_0017
082417_0018
082417_0019
082417_0020
082417_0021
082417_0022
082417_0023
082417_0024
082417_0025
082417_0026
082417_0027
082417_0028

Directory: Appendix\A1-29\1100C, 0.7eV Beam Trial 3, 150min
082517_0001
082517_0002

**Figure A1-29 cont.**

082517_0003

## Figure A1-30

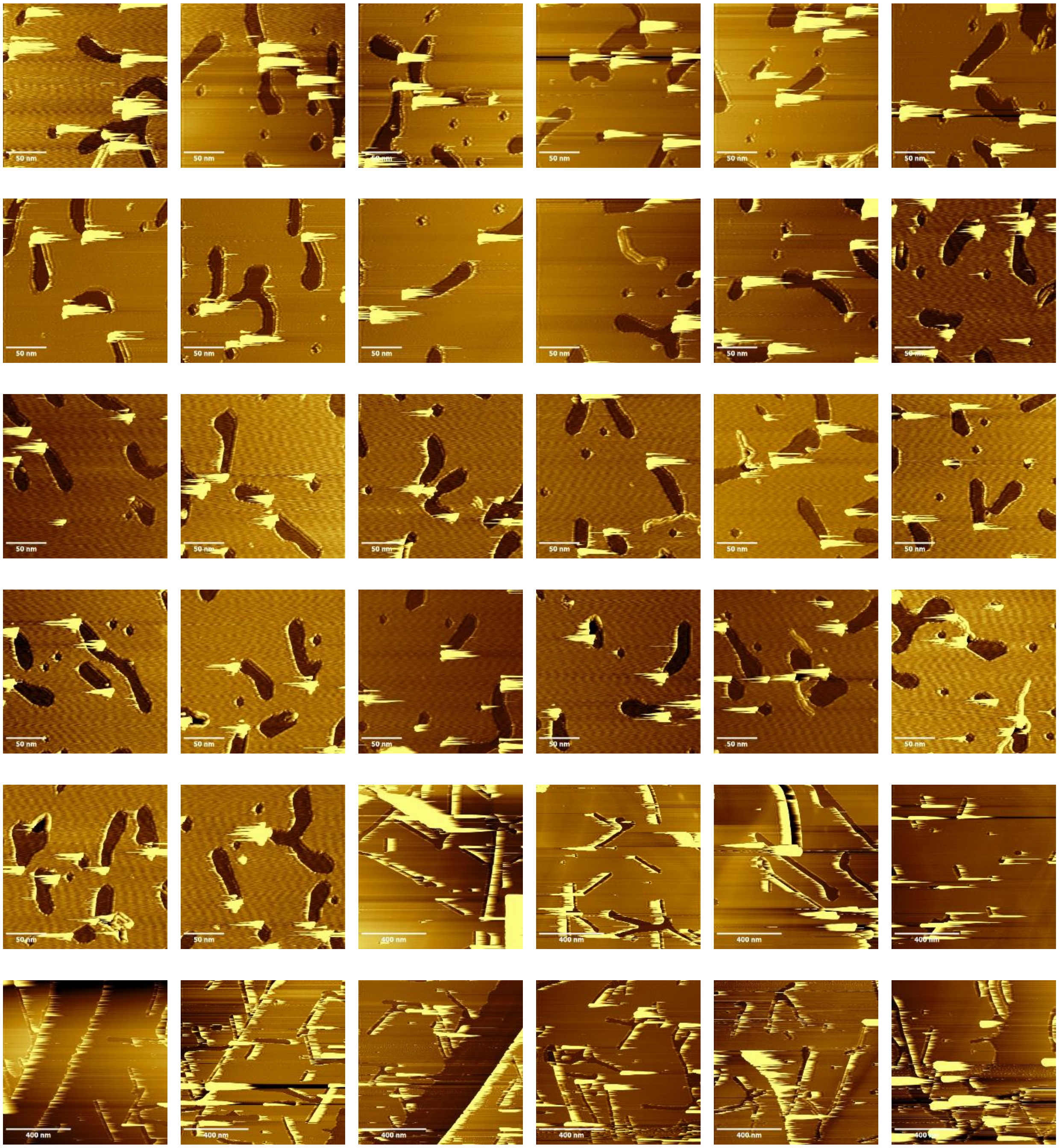

The sixth set of 36 images used in **Figure 4-6** and the sixth row of **Table 4-1.**

**Figure A1-30 cont.**

Filenames from top left to bottom right:

Directory: Appendix\A1-30\1100C, 0.7eV Beam Trial 3, 150min
082517_0004
082517_0005
082517_0006
082517_0007
082517_0008
082517_0009
082517_0010
082517_0011
082517_0012
082517_0013
082517_0014
082817_0001
082817_0002
082817_0003
082817_0004
082817_0005
082817_0006
082817_0007
082817_0008
082817_0009
082817_0010
082817_0011
082817_0012
082817_0013
082817_0014
082817_0016

Directory: Appendix\A1-30\1100C, 0.7eV Beam Trial 4, 90min
100917_0003
100917_0004
100917_0005
100917_0008
100917_0011
100917_0012
100917_0013
100917_0014
100917_0015
100917_0017

## Figure A1-31

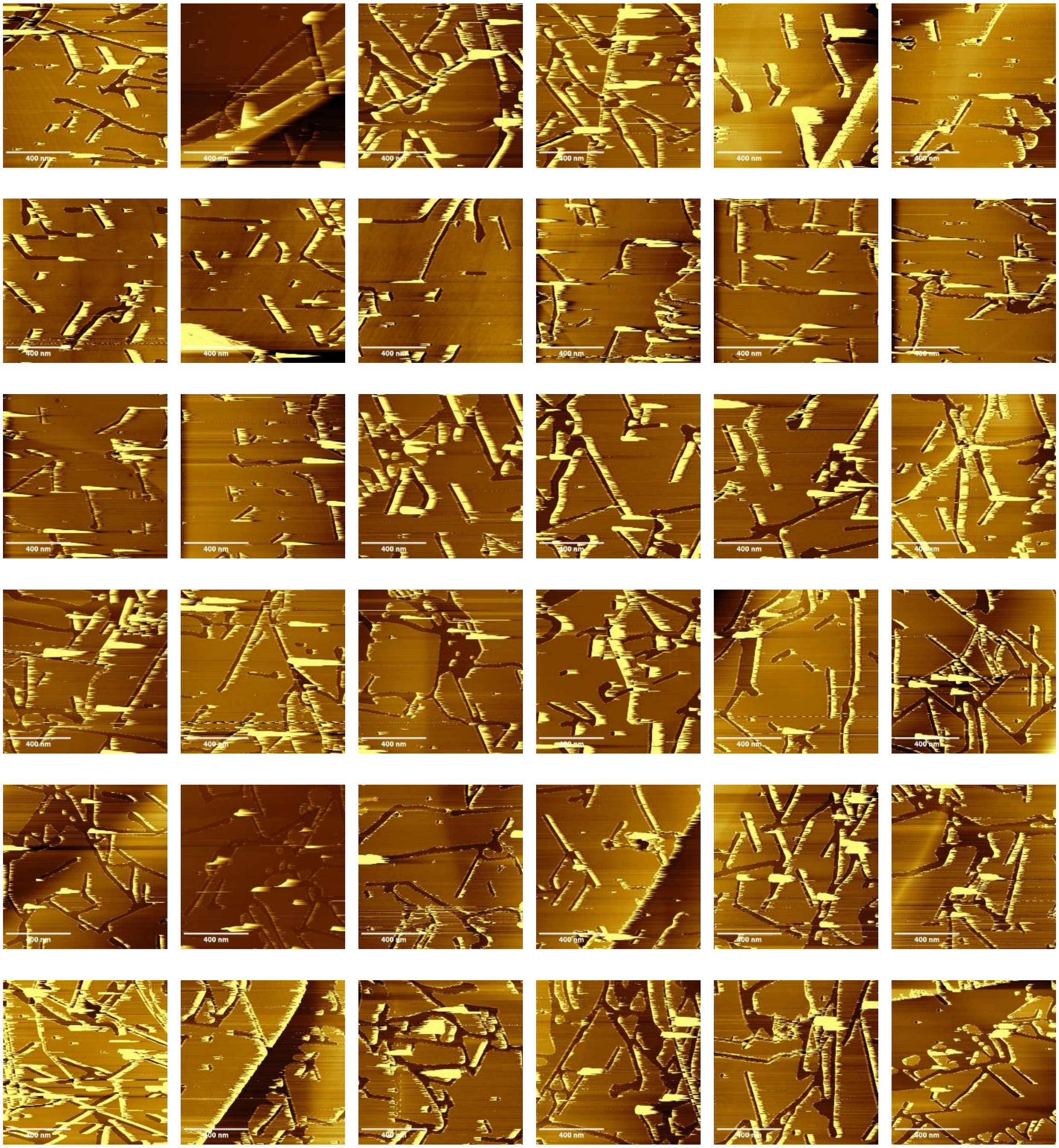

The seventh set of 36 images used in **Figure 4-6** and the sixth row of **Table 4-1.**

**Figure A1-31 cont.**

Filenames from top left to bottom right:

Directory: Appendix\A1-31\1100C, 0.7eV Beam Trial 4, 120min
101017_0001
101017_0002
101017_0003
101017_0004
101017_0005
101017_0006
101017_0010
101017_0011
101017_0012
101017_0013
101017_0014
101017_0015
101017_0016
101017_0017
101017_0018
101017_0019
101017_0020

Directory: Appendix\A1-31\1100C, 0.7eV Beam Trial 4, 150min
101117_0001
101117_0002
101117_0003
101117_0004
101117_0005
101117_0006
101117_0007
101117_0008
101117_0009
101117_0010
101117_0011
101117_0012
101117_0013

Directory: Appendix\A1-31\1100C, 0.7eV Beam Trial 4, 210min
101217_0001
101217_0002
101217_0003
101217_0004
101217_0005

**Figure A1-31 cont.**

101217_0006

**Figure A1-32**

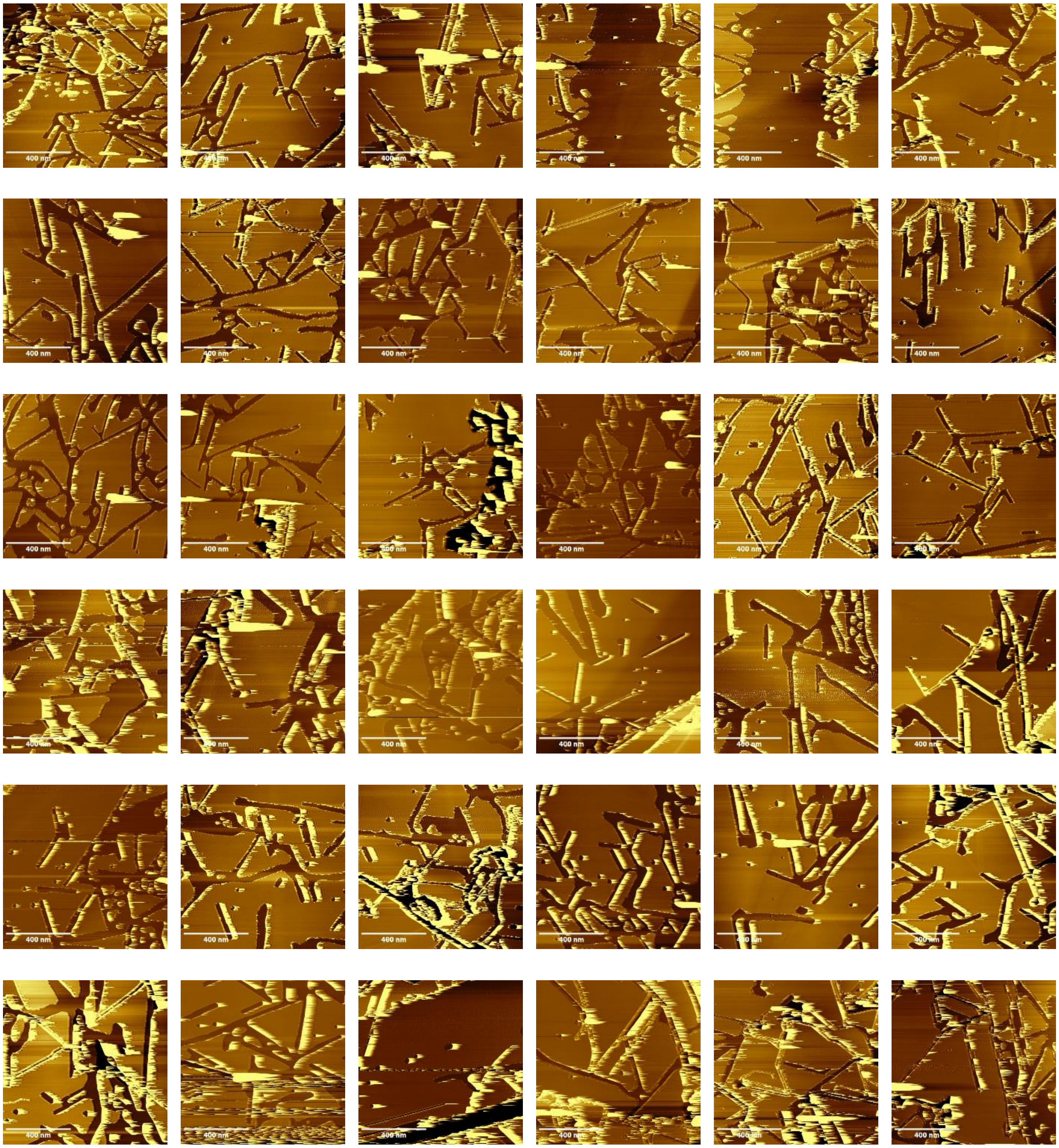

The eighth set of 36 images used in **Figure 4-6** and the sixth row of **Table 4-1.**

**Figure A1-32 cont.**

Filenames from top left to bottom right:

Directory: Appendix\A1-32\1100C, 0.7eV Beam Trial 4, 210min
101217_0007
101217_0008
101217_0009
101217_0012
101217_0013
101217_0014
101217_0015

Directory: Appendix\A1-32\1100C, 0.7eV Beam Trial 4, 270min
101317_0001
101317_0002
101317_0003
101317_0004
101317_0005
101317_0006
101317_0007
101317_0009
101317_0011
101317_0012
101317_0013

Directory: Appendix\A1-32\1100C, 0.7eV Beam Trial 4, 360min
101617_0001
101617_0002
101617_0005
101617_0007
101617_0008
101617_0009
101617_0011
101617_0012
101617_0013
101617_0015
101617_0016

Directory: Appendix\A1-32\1100C, 0.7eV Beam Trial 4, 480min
101717_0001
101717_0002
101717_0003
101717_0004
101717_0005
101717_0006

**Figure A1-32 cont.**

101717_0007

## Figure A1-33

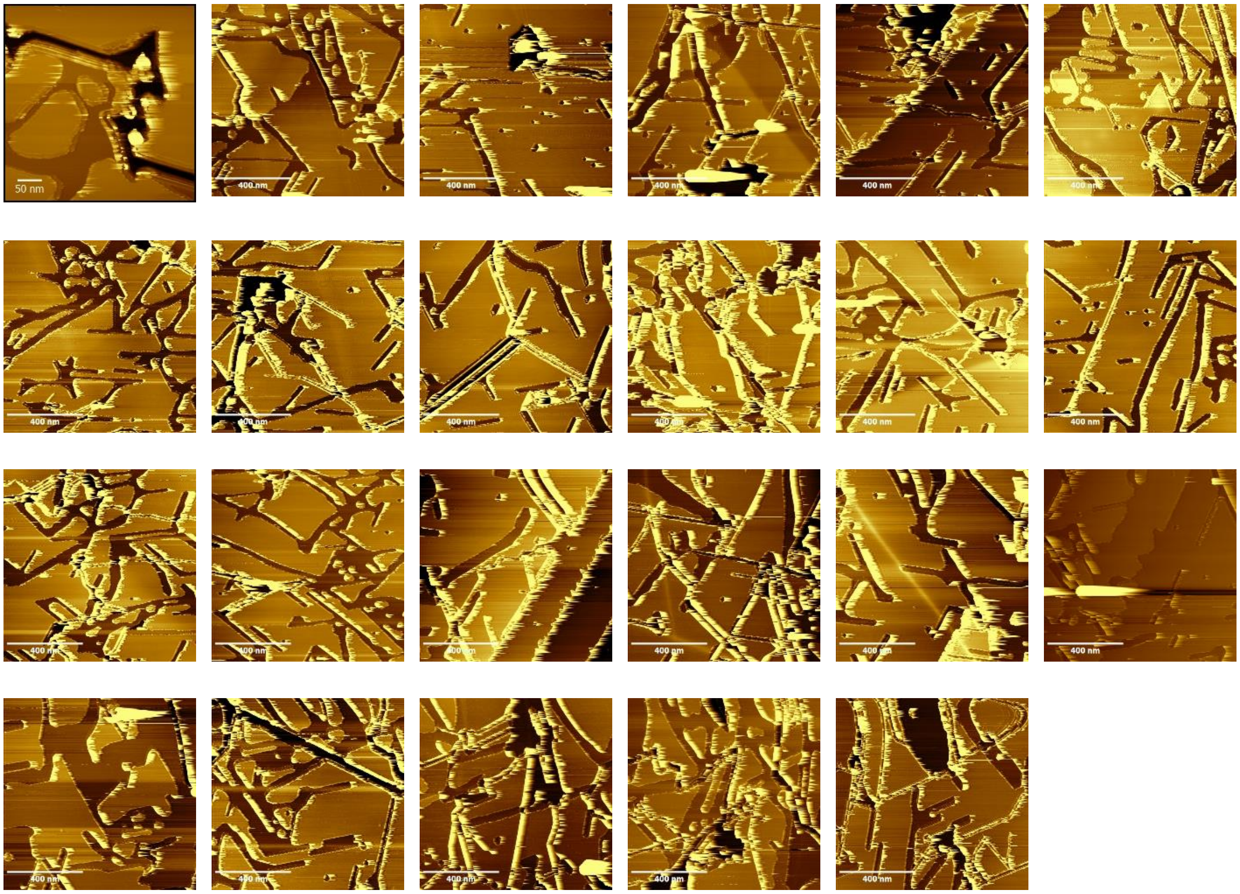

The ninth set of 23 images used in **Figure 4-6** and the sixth row of **Table 4-1.**

**Figure A1-33 cont.**

Filenames from top left to bottom right:

Directory: Appendix\A1-33\1100C, 0.7eV Beam Trial 4, 480min
101717_0008
101717_0009
101717_0010
101717_0012
101717_0013
101817_0001
101817_0002
101817_0003

Directory: Appendix\A1-33\1100C, 0.7eV Beam Trial 4, 600min
101817_0004
101817_0006
101817_0007
101817_0008
101817_0009
101817_0010
101817_0011
101817_0012
101817_0013
101917_0001
101917_0002
101917_0003
101917_0004
101917_0005
101917_0006

**Figure A1-34**

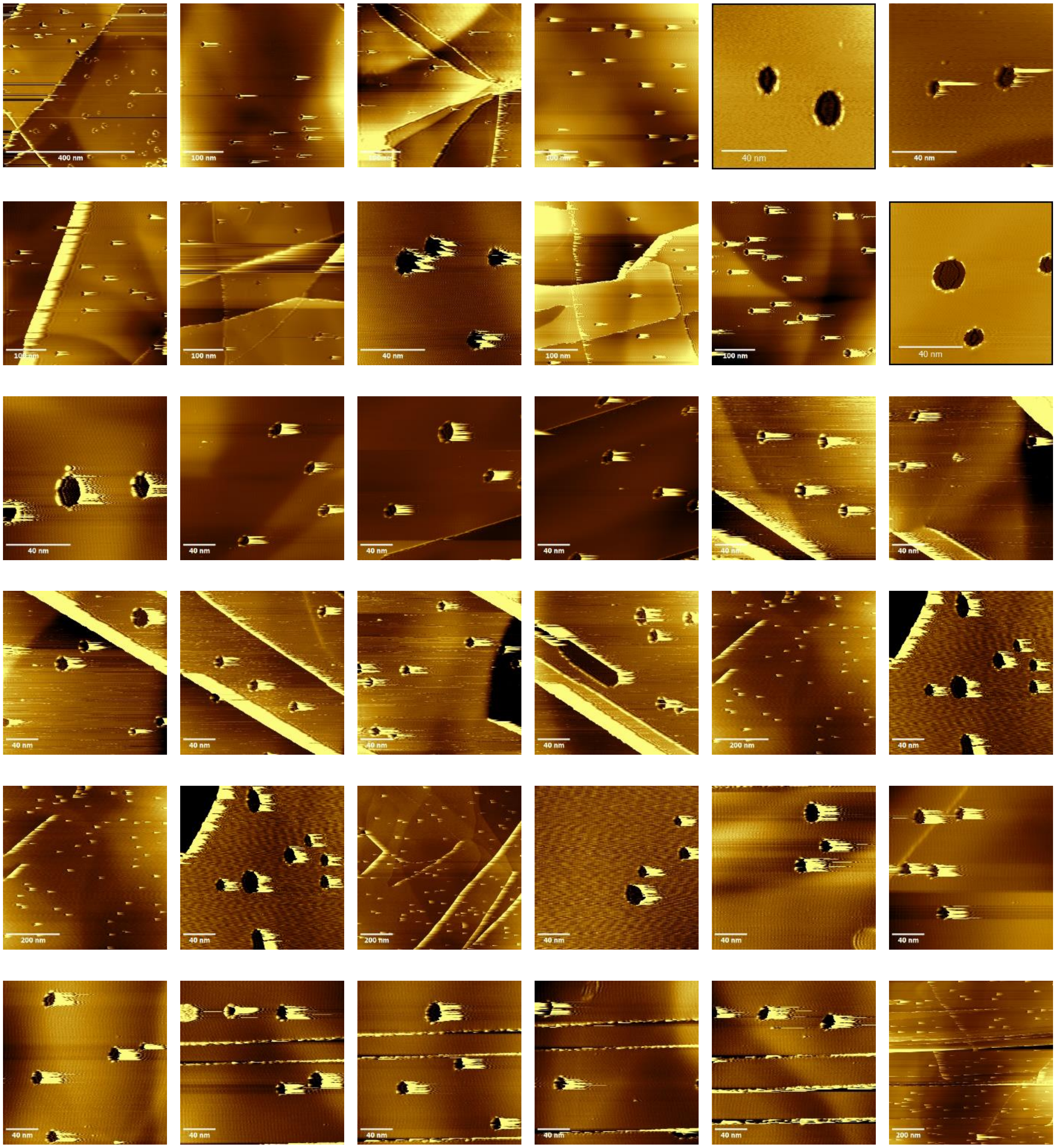

The first set of 36 images used in the seventh row of **Table 4-1.**

**Figure A1-34 cont.**

Filenames from top left to bottom right:

Directory: Appendix\A1-34\ 1100C, 0.7eV Beam, Grade 2, 2hr
102417_0002
102417_0003
102417_0006

Directory: Appendix\A1-34\ 1100C, 0.7eV Beam, Grade 2, 3hr
102417_0010
102417_0011
102417_0012
102417_0013
102517_0001
102517_0002
102517_0003

Directory: Appendix\A1-34\ 1100C, 0.7eV Beam, Grade 2, 8hr
102617_0014
102617_0015
102617_0016
102617_0021
102617_0022
102617_0023
102717_0002
102717_0003
102717_0005
102717_0006
102717_0007
102717_0009

Directory: Appendix\A1-34\ 1100C, 0.7eV Beam, Grade 2, 11.5hr
102717_0015
102717_0017
102717_0019
102717_0020
103017_0002
103017_0003
103017_0004
103017_0006
103017_0007
103017_0008
103017_0009

**Figure A1-34 cont.**

103017_0010

## Figure A1-35

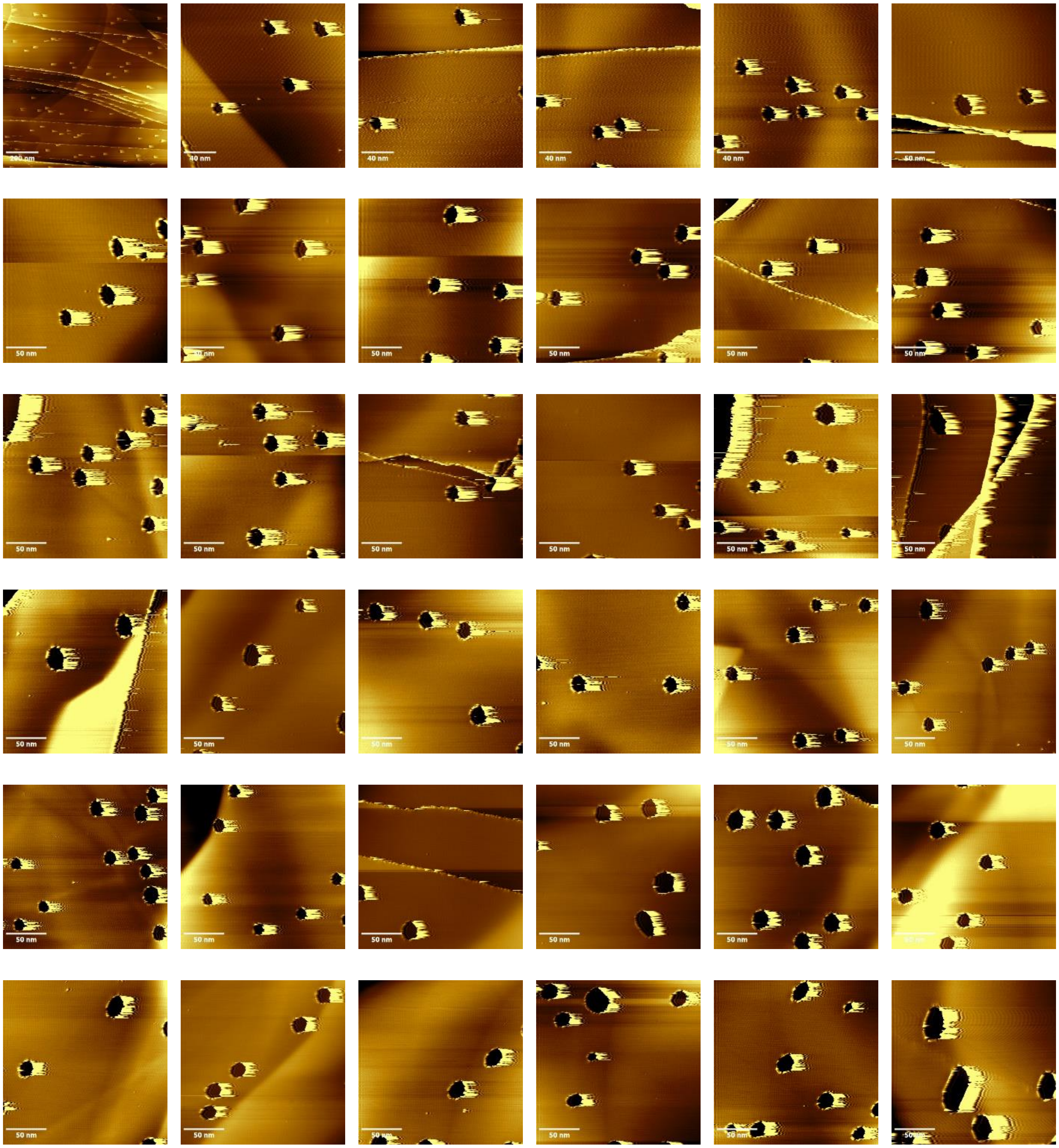

The second set of 36 images used in the seventh row of **Table 4-1.**

**Figure A1-35 cont.**

Filenames from top left to bottom right:

Directory: Appendix\A1-35\ 1100C, 0.7eV Beam, Grade 2, 11.5hr
103017_0012
103017_0013
103017_0015
103017_0016
103017_0017
103017_0018

Directory: Appendix\A1-35\ 1100C, 0.7eV Beam, Grade 2, 16hr
103017_0021
103017_0022
103017_0023
103017_0024
103017_0025
103017_0026
103117_0002
103117_0003
103117_0004
103117_0005
103117_0006
103117_0008
103117_0009
103117_0010
103117_0011
103117_0012
103117_0013
103117_0015
103117_0016
103117_0017

Directory: Appendix\A1-35\ 1100C, 0.7eV Beam, Grade 2, 25.5hr
110117_0002
110117_0003
110117_0004
110117_0005
110117_0006
110117_0007
110117_0008
110117_0009
110117_0010
110117_0012

**Figure A1-36**

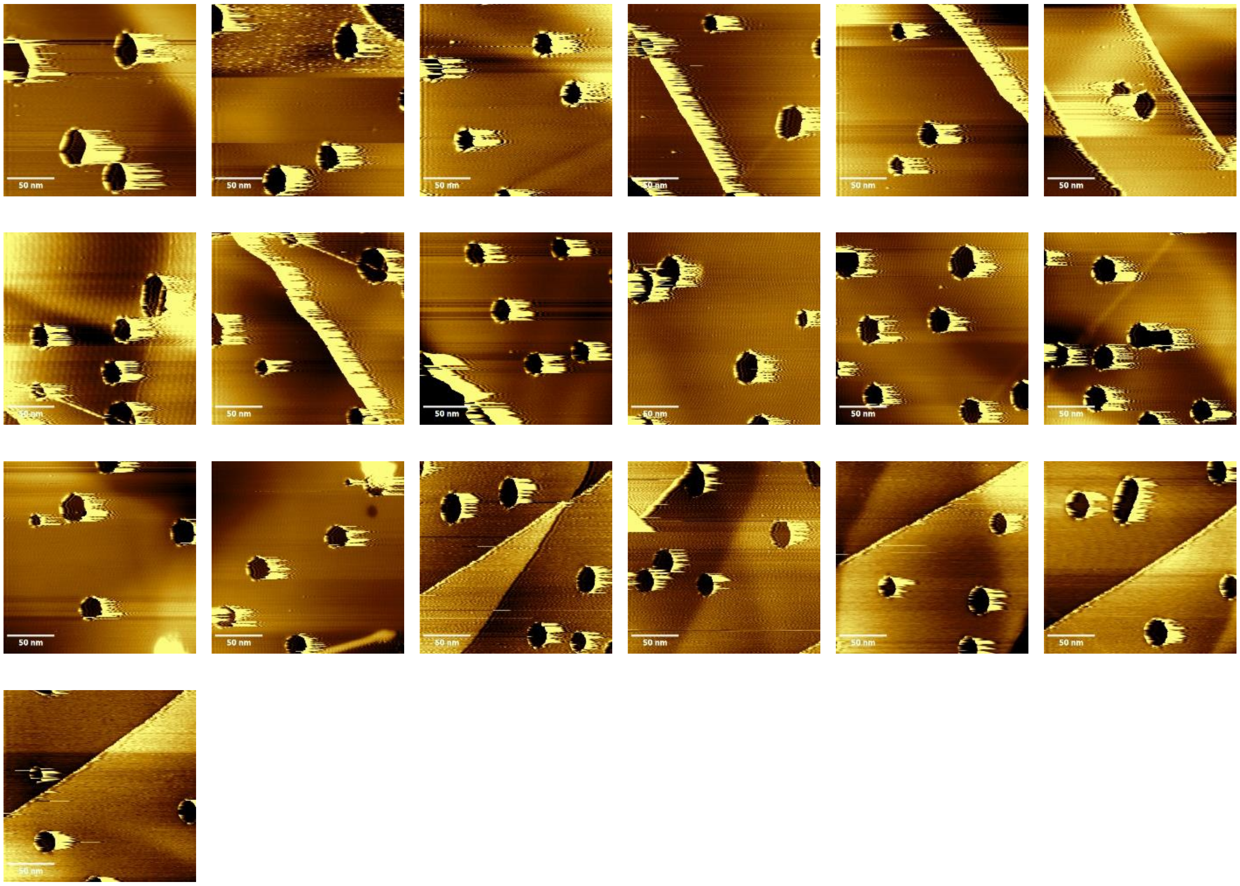

The final 19 images used in the seventh row of **Table 4-1.**

**Figure A1-36 cont.**

Filenames from top left to bottom right:

Directory: Appendix\A1-36\ 1100C, 0.7eV Beam, Grade 2, 25.5hr
110117_0013
110217_0002
110217_0003
110217_0004
110217_0005
110217_0006
110217_0008
110217_0009
110217_0010
110217_0012
110217_0013
110217_0014
110217_0015
110217_0016
110217_0018
110217_0019
110217_0020
110217_0021
110217_0022

## Figure A1-37

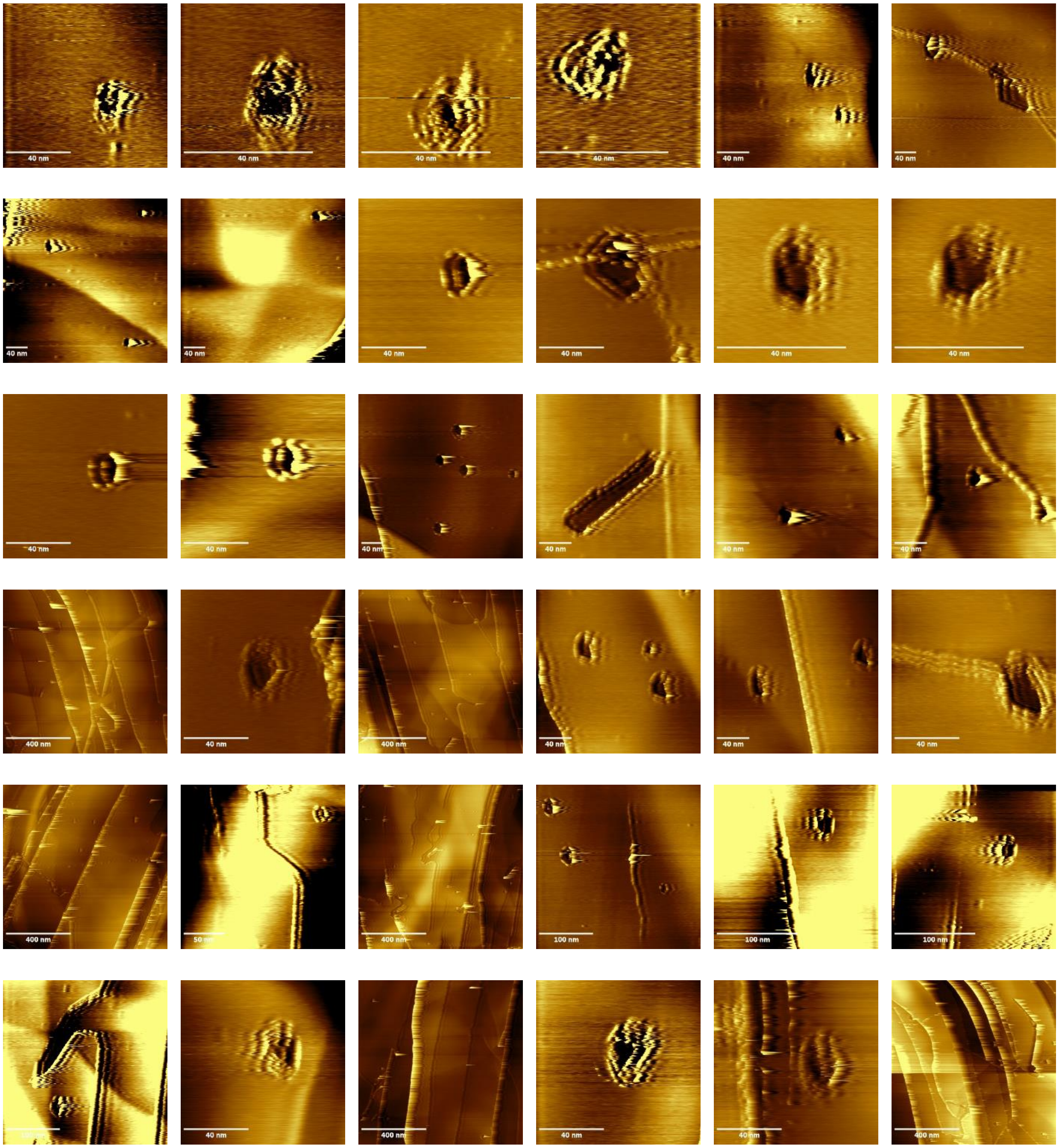

The first set of 36 of images used in the eighth row of **Table 4-1.**

**Figure A1-37 cont.**

Filenames from top left to bottom right:

Directory: Appendix\A1-37\ 45 Degrees, 1100C, 0.7eV Beam, Grade 2, 3.5hr
120117_0002
120117_0003
120117_0004
120117_0005

Directory: Appendix\A1-37\ 45 Degrees, 1100C, 0.7eV Beam, Grade 2, 7hr
120417_0002
120417_0003
120417_0004
120417_0006
120417_0009
120417_0010
120417_00103
120417_0014
120417_0016
120417_0017
120417_0019
120417_0021
120417_0023
120417_0025

Directory: Appendix\A1-37\ 45 Degrees, 1100C, 0.7eV Beam, Grade 2, 12hr
120517_0003
120517_0004
120517_0005
120517_0006
120517_0007
120517_0008
120517_0011
120617_0001
120617_0002
120617_0003
120617_0004
120617_0005
120617_0006
120617_0007
120617_0008
120617_0009
120617_0010

**Figure A1-37 cont.**

Directory: Appendix\A1-37\ 45 Degrees, 1100C, 0.7eV Beam, Grade 2, 17hr
120617_0011

**Figure A1-38**

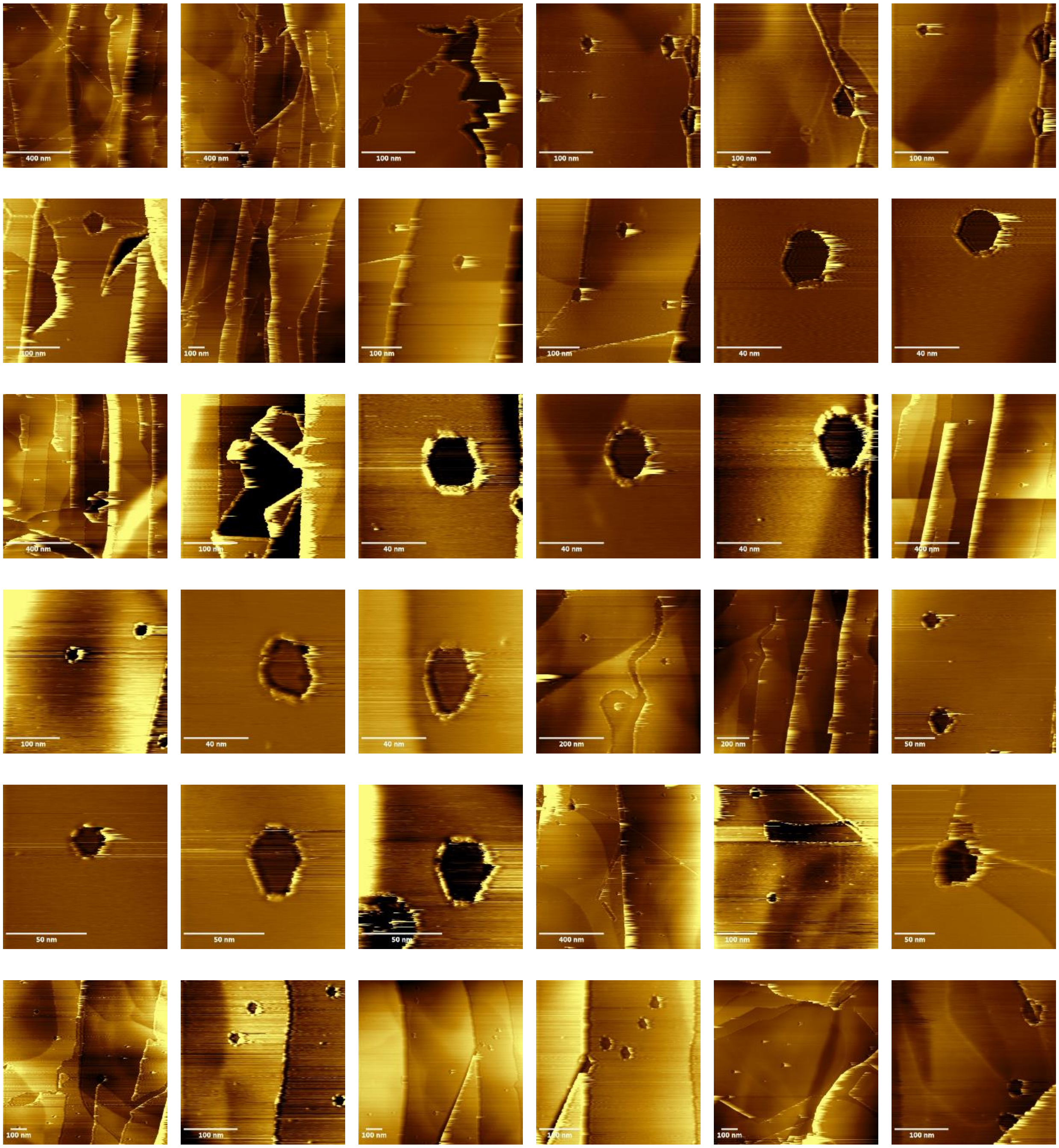

The second set of 36 images used in the eighth row of **Table 4-1.**

**Figure A1-38 cont.**

Filenames from top left to bottom right:

Directory: Appendix\A1-38\ 45 Degrees, 1100C, 0.7eV Beam, Grade 2, 17hr
120617_0012
120717_0001
120717_0002
120717_0003
120717_0004
120717_0005
120717_0006
120717_0007
120717_0008
120717_0009
120717_0010
120717_0011
120717_0012
120717_0013
120717_0014
120717_0015
120717_0016
120717_0017
120717_0018
120717_0019
120717_0020
120717_0021
120717_0022
120717_0023
120717_0024
120717_0025
120717_0026
120717_0028
120717_0029
120717_0030
120717_0031
120717_0032
120717_0033
120717_0034

Directory: Appendix\A1-38\ 45 Degrees, 1100C, 0.7eV Beam, Grade 2, 22hr
120817_0001
120817_0002

## Figure A1-39

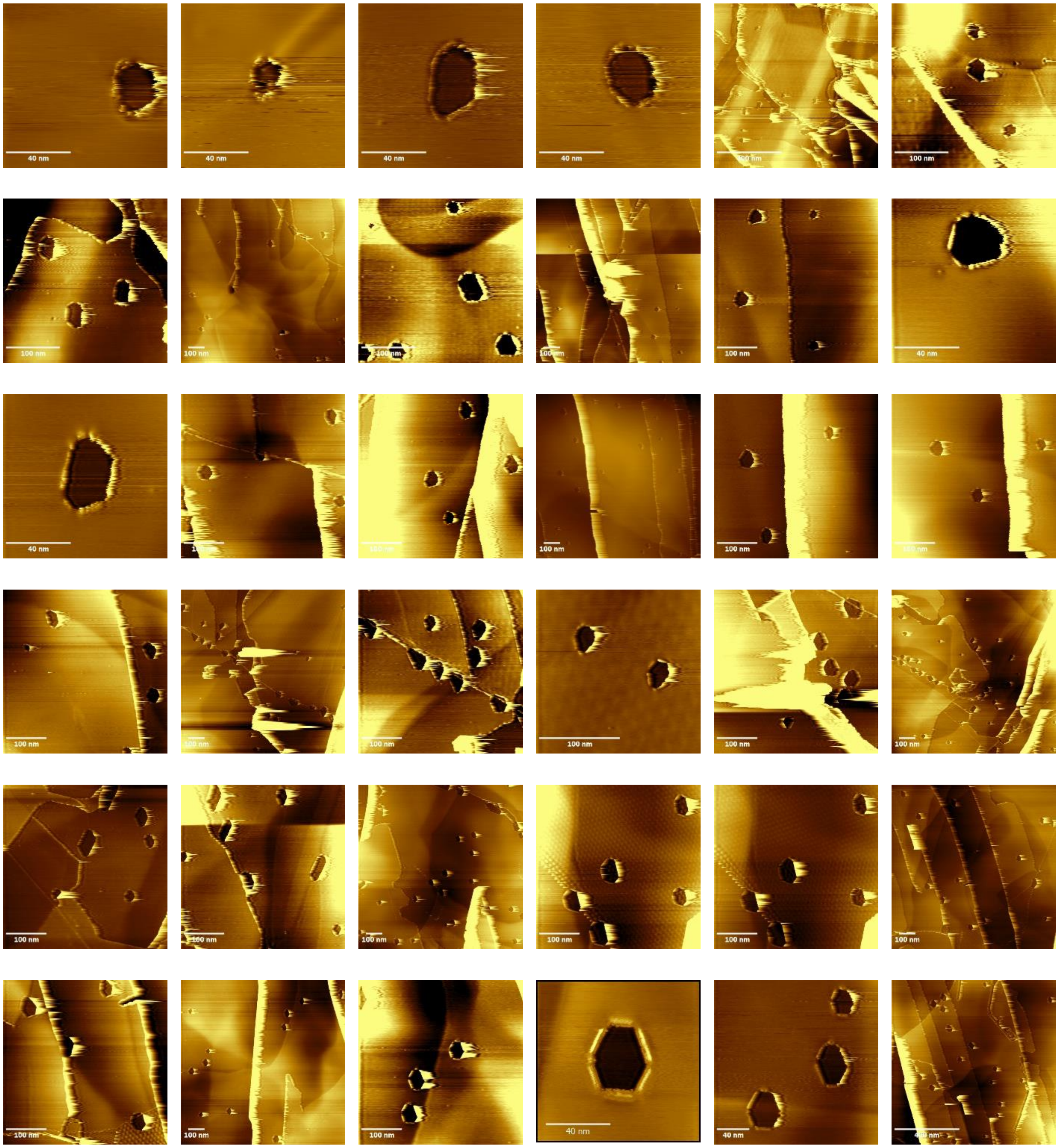

The third set of 36 images used in the eighth row of **Table 4-1.**

**Figure A1-39 cont.**

Filenames from top left to bottom right:

Directory: Appendix\A1-39\ 45 Degrees, 1100C, 0.7eV Beam, Grade 2, 22hr
120817_0003
120817_0004
120817_0005
120817_0006
120817_0007
120817_0008
120817_0009
120817_0010
120817_0011
121117_0001
121117_0002
121117_0004
121117_0005
121117_0006
121117_0007
121117_0008
121117_0009
121117_0010
121117_0011
121117_0012
121117_0013
121117_0014
121117_0015
121117_0016
121117_0017
121117_0018

Directory: Appendix\A1-39\ 45 Degrees, 1100C, 0.7eV Beam, Grade 2, 31hr
121217_0001
121217_0002
121217_0003
121217_0004
121217_0005
121217_0006
121217_0007
121217_0008
121217_0009
121217_0010

**Figure A1-40**

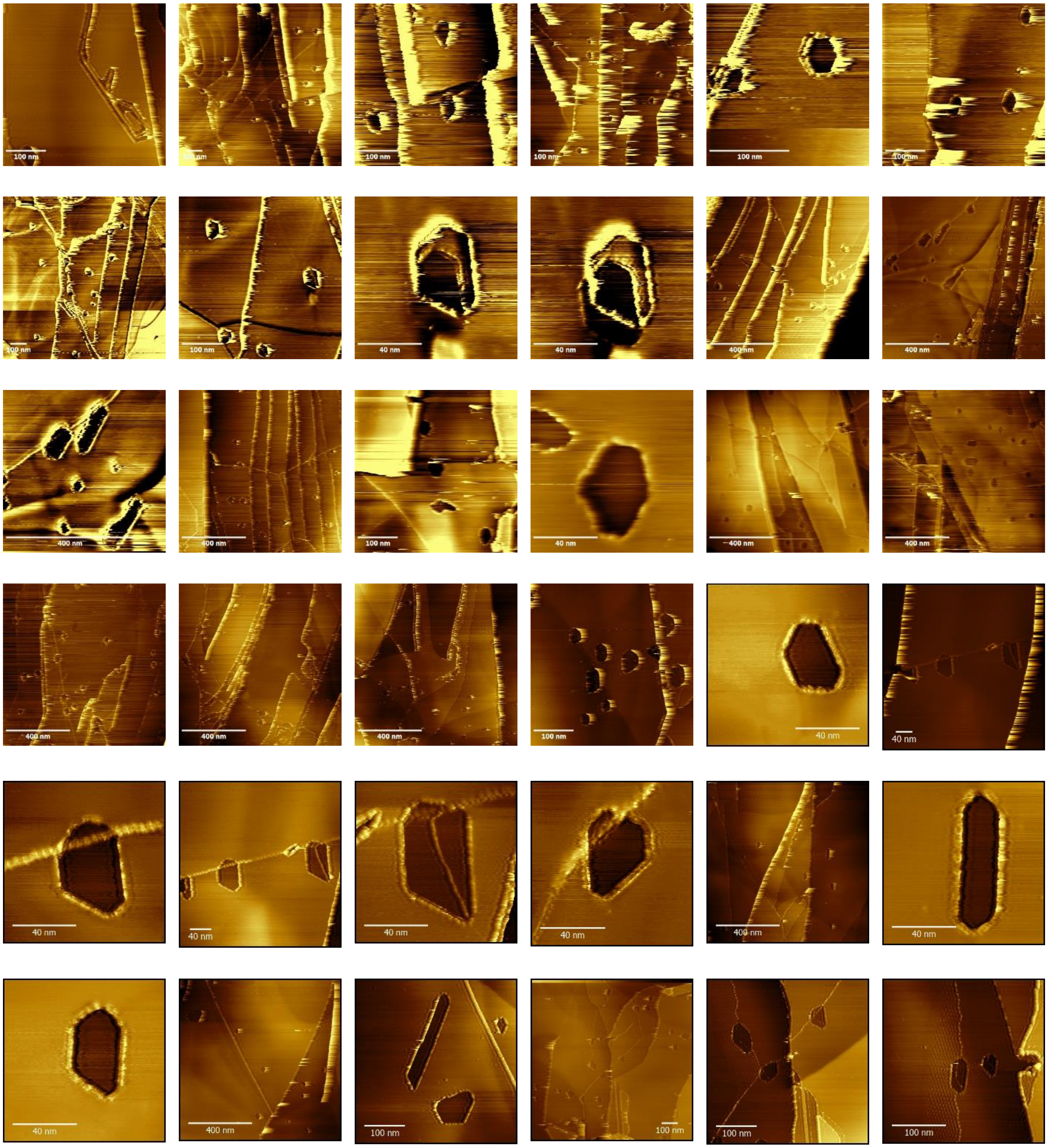

The fourth set of 36 images used in the eighth row of **Table 4-1.**

**Figure A1-40 cont.**

Filenames from top left to bottom right:

Directory: Appendix\A1-40\ 45 Degrees, 1100C, 0.7eV Beam, Grade 2, 31hr
121217_0011
121217_0012
121217_0013
121317_0001
121317_0002
121317_0003
121317_0004
121317_0005
121317_0007
121317_0008
121317_0009
121317_0010
121317_0011
121317_0012
121417_0002
121417_0003
121417_0007
121417_0008
121517_0001
121517_0002
121517_0003
121517_0004
121917_0001
121917_0002
121917_0003
121917_0004
121917_0005
121917_0006
122017_0001
122017_0002
122017_0003
122017_0004
122017_0005
122017_0006
122017_0007
122017_0008

**Figure A1-41**

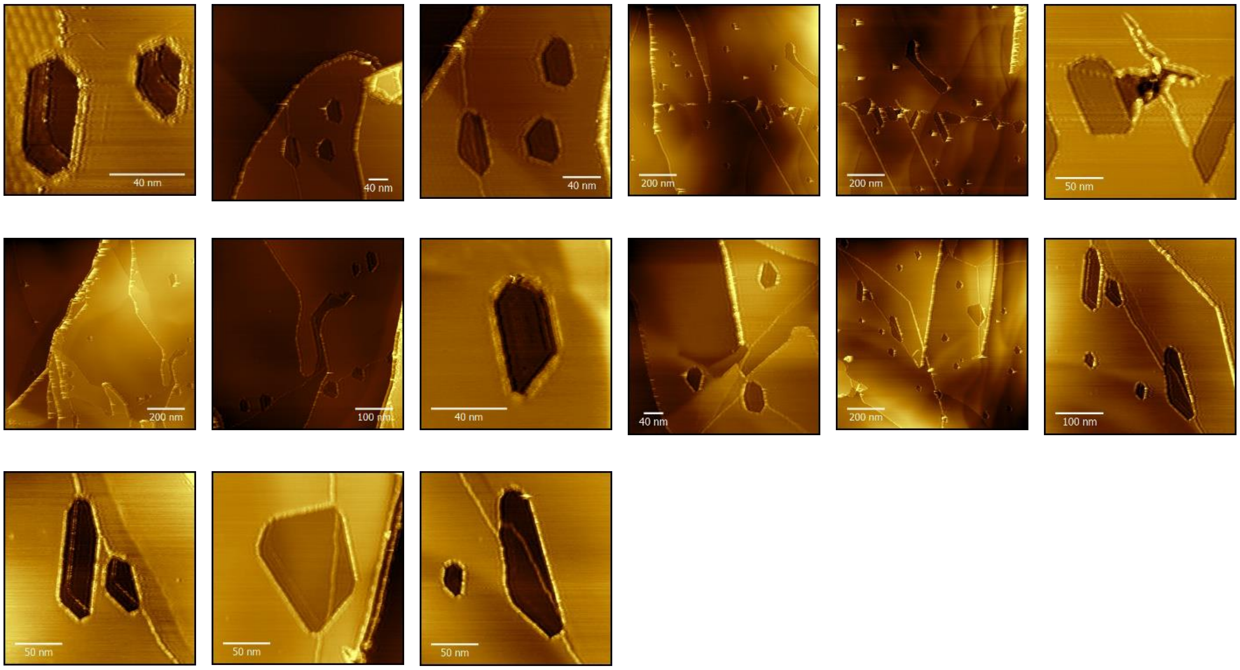

The final 15 images used in the eighth row of **Table 4-1.**

**Figure A1-41 cont.**

Filenames from top left to bottom right:

Directory: Appendix\A1-41\ 45 Degrees, 1100C, 0.7eV Beam, Grade 2, 31hr
122017_0009
122017_0010
122017_0011
122017_0012
122017_0013
122017_0014
122117_0001
122117_0002
122117_0003
122117_0004
122117_0005
122117_0006
122117_0007
122117_0008
122117_0009

**Figure A1-42**

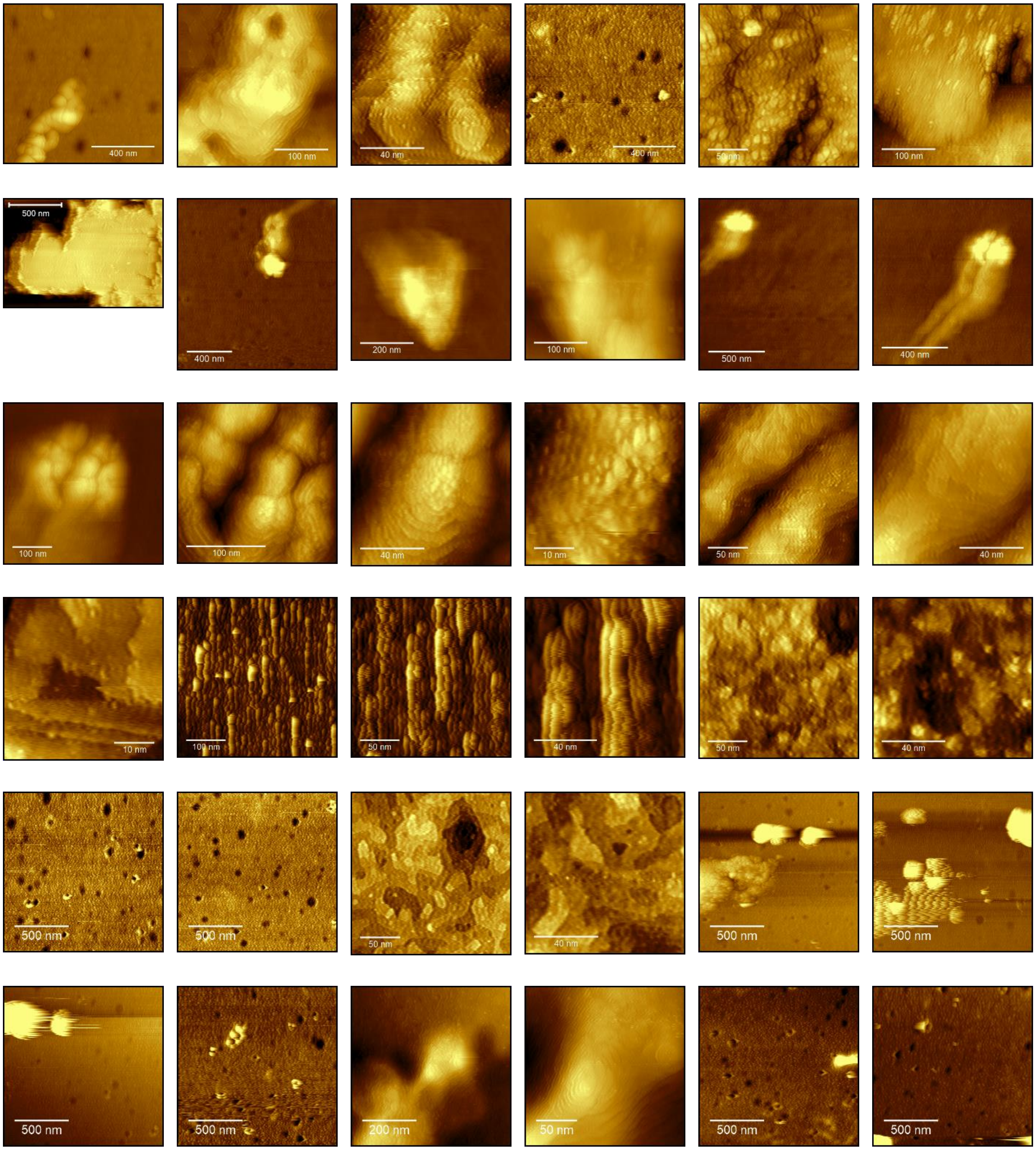

The first set of 36 images used in **Figure 5-2** and the heterogeneous reactivity series in **Figure 5-9.**

**Figure A1-42 cont.**

Filenames from top left to bottom right:

Directory: Appendix\A1-42\ 0.4eV Beam, 16hr
012218_0022
012218_0024
012218_0025
012218_0026
012218_0028
012318_0003
012318_0005_crop
012318_0008
012318_0012
012318_0013
012318_0016
012318_0017
012318_0018
012318_0019
012318_0020
012318_0021
012318_0022
012318_0023
012318_0024
012318_0031
012318_0032
012318_0033
012318_0034
012318_0035

Directory: Appendix\A1-42\ 0.7eV Beam, 13hr
020418_0001
020418_0002
020418_0003
020418_0004
020418_0005
020418_0008
020418_0009
020418_0010
020418_0011
020418_0012
020418_0014
020418_0015

## Figure A1-43

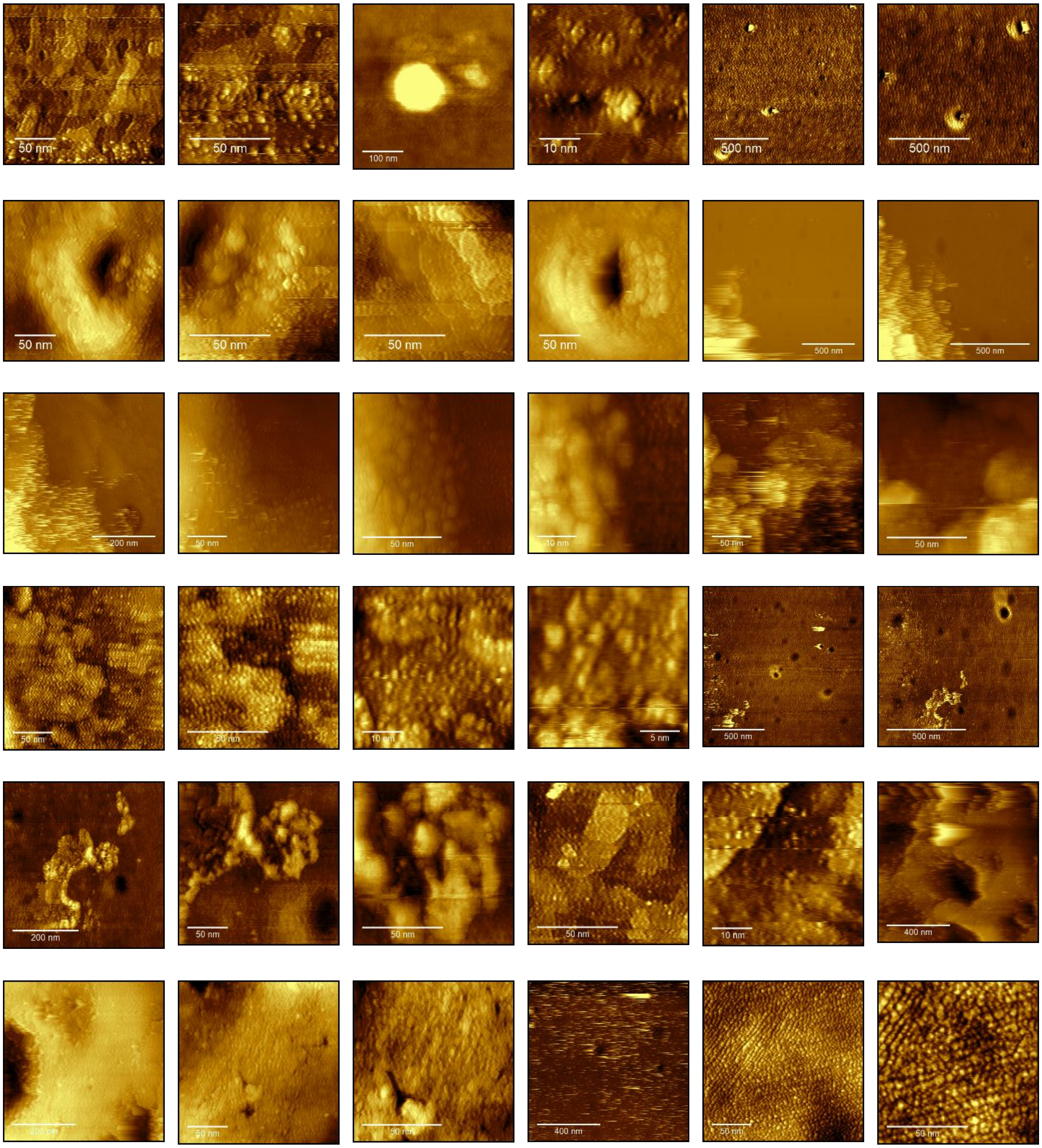

The second set of 36 images used in **Figure 5-2** and the heterogeneous reactivity series in **Figure 5-9.**

**Figure A1-43 cont.**

Filenames from top left to bottom right:

Directory: Appendix\A1-43\ 0.7eV Beam, 13hr
020418_0016
020418_0017
020418_0020
020418_0025
020418_0026
020418_0027
020418_0028
020418_0029
020418_0030
020418_0031

Directory: Appendix\A1-43\ 1.0eV Beam, 12hr
022219_0001
022219_0002
022219_0003
022219_0004
022219_0005
022219_0006
022219_0007
022219_0008
022219_0009
022219_0010
022219_0011
022219_0012
022219_0013
022219_0014
022219_0015
022219_0016
022219_0017
022219_0018
022219_0019
022219_0020
022219_0021
022219_0022
022219_0023
022219_0024
022219_0025
022219_0026

**Figure A1-44**

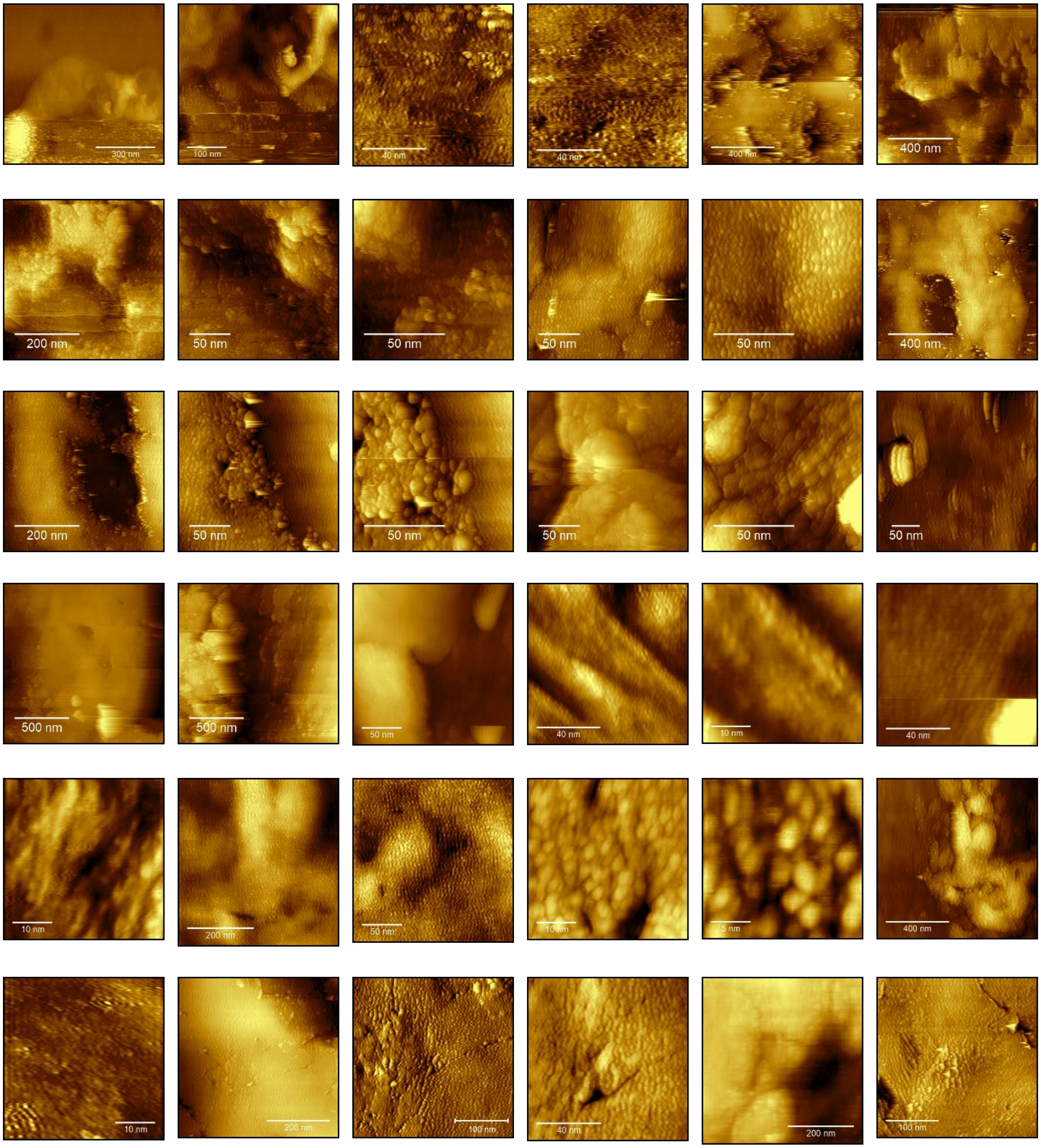

The third set of 36 images used in **Figure 5-2** and the heterogeneous reactivity series in **Figure 5-9.**

**Figure A1-44 cont.**

Filenames from top left to bottom right:

Directory: Appendix\A1-44\ 1.0eV Beam, 12hr
022419_0002
022419_0003
022419_0004
022419_0005
022419_0007

Directory: Appendix\A1-44\ 1.1eV Beam, 7.5hr
030719_0026
030719_0027
030719_0028
030719_0029
030719_0032
030719_0033
030719_0034
030719_0035
030719_0036
030719_0037
030719_0040
030719_0041
030719_0042
030819_0001
030819_0002

Directory: Appendix\A1-44\ 1.2eV Beam, 75min
011018_0035
011018_0036
011018_0037
011018_0038
011018_0039
011018_0040
011018_0041
011018_0042
011018_0043
011018_0044
011018_0045
011018_0048
011018_0049
011018_0050
011018_0052

**Figure A1-44 cont.**

011018_0053

**Figure A1-45**

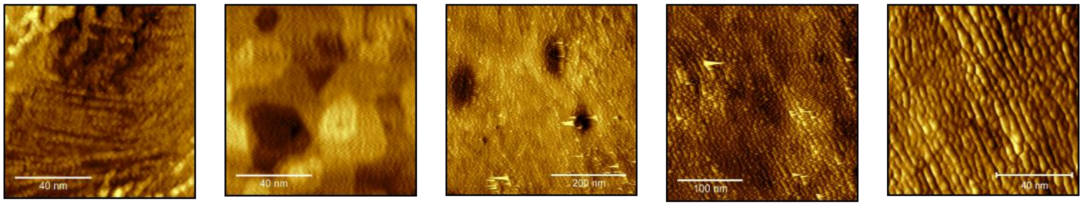

The final 5 images used in **Figure 5-2** and the heterogeneous reactivity series in **Figure 5-9.**

**Figure A1-45 cont.**

Filenames from top left to bottom right:

Directory: Appendix\A1-45\ 1.2eV Beam, 75min
011018_0054
011018_0056
011118_0002
011118_0003
011118_0004

## Figure A1-46

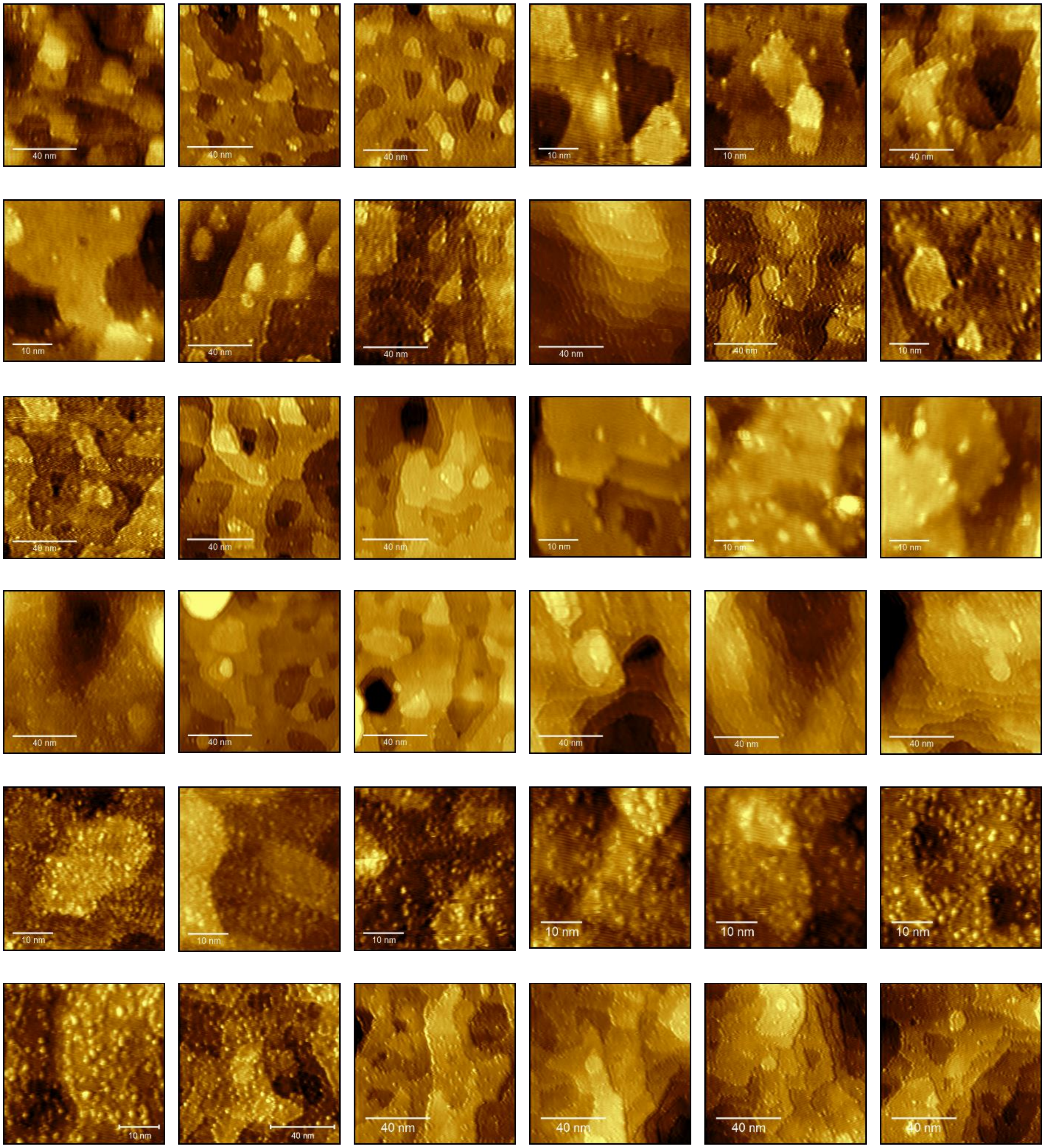

The first set of 36 images used in **Figure 5-8** and the homogeneous reactivity series in **Figure 5-9.**

**Figure A1-46 cont.**

Filenames from top left to bottom right:

Directory: Appendix\A1-46\Bright Sites, Clean
010318_0002
010318_0005
011218_0003
011218_0004
011218_0005
011218_0007
011218_0019
020518_0002
020518_0009
021118_0014
021118_0016
021118_0017
021218_0007
022818_0007
022818_0008
022818_0009
022818_0016
022818_0020
022818_0023
022818_0026
022818_0027
030118_0001
030118_0002
030118_0003

Directory: Appendix\A1-46\Bright Sites, 1.0eV, 10hr
022119_0012
022119_0013
022119_0019
022119_0028
022119_0029
022119_0030
022119_0031

Directory: Appendix\A1-46\Bright Sites, 1.1eV, 1.5hr
030118_0025
030118_0034
030118_0035
030118_0036

**Figure A1-46 cont.**

030118_0037

**Figure A1-47**

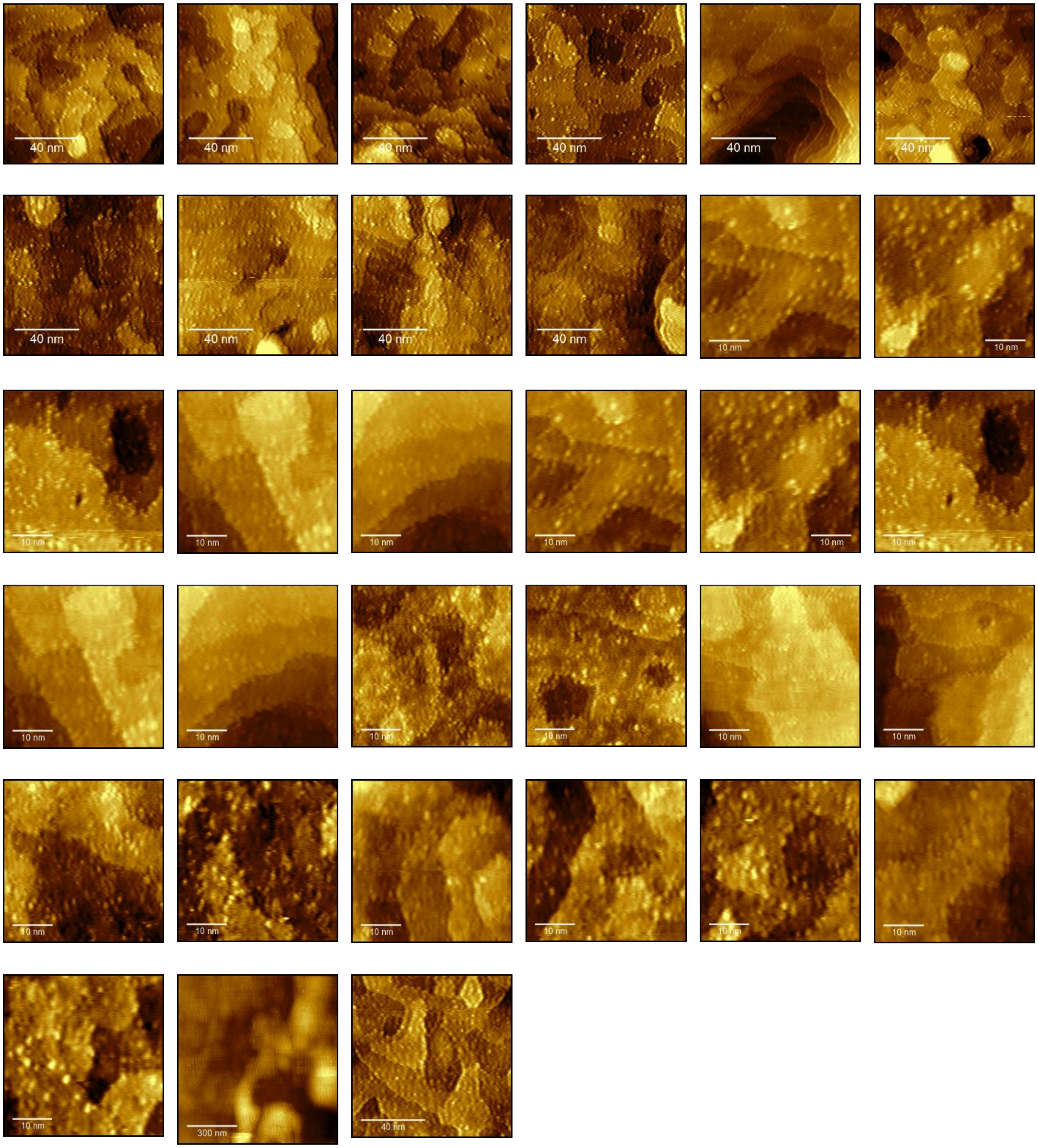

The final 33 images used in **Figure 5-8** and the homogeneous reactivity series in **Figure 5-9.**

**Figure A1-47 cont.**

Filenames from top left to bottom right:

Directory: Appendix\A1-47\Bright Sites, 1.1eV, 1.5hr
030118_0038
030118_0039
030118_0040
030218_0004

Directory: Appendix\A1-47\Bright Sites, 1.1eV, 1.75hr
030219_0011
030219_0012
030219_0016
030219_0017
030219_0018
030219_0019

Directory: Appendix\A1-47\Bright Sites, 1.1eV, 3.5hr
030419_0023
030419_0024
030419_0025
030419_0026
030419_0027

Directory: Appendix\A1-47\Bright Sites, 1.1eV, 4hr
030519_0010
030519_0011
030519_0012
030519_0013

Directory: Appendix\A1-47\Bright Sites, 1.1eV, 5.5hr
030719_0006
030719_0007
030719_0008
030719_0009
030719_0010
030719_0011
030719_0012

Directory: Appendix\A1-47\Bright Sites, 1.2eV, 1hr
010918_0046
011018_0021

# Appendix 2: Copyright Attribution

**Chapter 2** is adapted in part with permission from Wiggins, B.; Avila-Bront, L. G.; Edel, R.; Sibener, S. J. Temporally and Spatially Resolved Oxidation of Si (111)-(7×7) Using Kinetic Energy Controlled Supersonic Beams in Combination with Scanning Tunneling Microscopy. *The Journal of Physical Chemistry C* **2016**, *120* (15), 8191–8197. Copyright 2016 American Chemical Society.

**Chapter 3** is reprinted with permission from Wiggins, B.; Avila-Bront, L. G.; Edel, R.; Sibener, S. J. Temporally and Spatially Resolved Oxidation of Si (111)-(7×7) Using Kinetic Energy Controlled Supersonic Beams in Combination with Scanning Tunneling Microscopy. *The Journal of Physical Chemistry C* **2016**, *120* (15), 8191–8197. Copyright 2016 American Chemical Society.

**Chapter 4** is reprinted with permission from Edel, R.; Grabnic, T.; Wiggins, B.; Sibener, S. J. Atomically-Resolved Oxidative Erosion and Ablation of Basal Plane HOPG Graphite Using Supersonic Beams of $O_2$ with Scanning Tunneling Microscopy Visualization. *J. Phys. Chem. C* **2018**, *122* (26), 14706–14713. https://doi.org/10.1021/acs.jpcc.8b04139. Copyright 2018 American Chemical Society. It is also adapted in part with permission from Hariharan, S.; Majumder, M.; Edel, R.; Grabnic, T.; Sibener, S. J.; Hase, W. L. Exploratory Direct Dynamics Simulations of $^3O_2$ Reaction with Graphene at High Temperatures. *J. Phys. Chem. C* **2018**, *122* (51), 29368–29379. https://doi.org/10.1021/acs.jpcc.8b10146. Copyright 2018 American Chemical Society

**Chapter 5** is reprinted with permission from Grabnic, T.; Edel, R.; Sibener, S. J. Room Temperature Oxidation of GaAs(110) Using High Translational Kinetic Energy Molecular Beams of $O_2$ Visualized by STM. *Surface Science* **2020**, *692*, 121516. https://doi.org/10.1016/j.susc.2019.121516. Copyright 2019 Elsevier.

# References

(1) Avouris, P.; Lyo, I.-W.; Bozso, F. Atom-Resolved Surface Chemistry: The Early Steps of Si (111)-7×7 Oxidation. *Journal of Vacuum Science & Technology B* **1991**, *9* (2), 424–430.

(2) Yan, C.; Jensen, J. A.; Kummel, A. C. Scanning Tunneling Microscopy of the Effect of Incident Energy upon Chemisorption Sites for $O_2$/Si(111)-7×7. *The Journal of Chemical Physics* **1996**, *105* (2), 773–778. https://doi.org/10.1063/1.471887.

(3) Yoshigoe, A.; Teraoka, Y. Synchrotron Radiation Photoelectron Spectroscopy Study on Oxide Evolution during Oxidation of a Si(111)-7 × 7 Surface at 300 K: Comparison of Thermal Equilibrium Gas and Supersonic Molecular Beams for Oxygen Adsorption. *The Journal of Physical Chemistry C* **2014**, *118* (18), 9436–9442. https://doi.org/10.1021/jp410821r.

(4) Delehouzé, A.; Rebillat, F.; Weisbecker, P.; Leyssale, J.-M.; Epherre, J.-F.; Labrugère, C.; Vignoles, G. L. Temperature Induced Transition from Hexagonal to Circular Pits in Graphite Oxidation by $O_2$. *Applied Physics Letters* **2011**, *99* (4), 044102.

(5) Murray, V. J.; Smoll, E. J.; Minton, T. K. Dynamics of Graphite Oxidation at High Temperature. *J. Phys. Chem. C* **2018**. https://doi.org/10.1021/acs.jpcc.7b11772.

(6) Hariharan, S.; Majumder, M.; Edel, R.; Grabnic, T.; Sibener, S. J.; Hase, W. L. Exploratory Direct Dynamics Simulations of $^3O_2$ Reaction with Graphene at High Temperatures. *J. Phys. Chem. C* **2018**, *122* (51), 29368–29379. https://doi.org/10.1021/acs.jpcc.8b10146.

(7) Stroscio, J. A.; Feenstra, R. M.; Fein, A. P. Structure of Oxygen Adsorbed on the GaAs (110) Surface Studied Using Scanning Tunneling Microscopy. *Physical Review B* **1987**, *36* (14), 7718.

(8) Landgren, G.; Ludeke, R.; Morar, J. F.; Jugnet, Y.; Himpsel, F. J. Oxidation of GaAs(110): New Results and Models. *Phys. Rev. B* **1984**, *30* (8), 4839–4841. https://doi.org/10.1103/PhysRevB.30.4839.

(9) Childs, K. D.; Lagally, M. G. Species-Specific Densities of States of Ga and As in the Chemisorption of Oxygen on GaAs(110). *Phys. Rev. B* **1984**, *30* (10), 5742–5752. https://doi.org/10.1103/PhysRevB.30.5742.

(10) Askeland, D. R.; Fulay, P. P.; Wright, W. J. *The Science and Engineering of Materials*; Cengage Learning, 2010.

(11) Takayanagi, K.; Tanishiro, Y.; Takahashi, M.; Takahashi, S. Structural Analysis of Si (111)-7×7 by UHV-Transmission Electron Diffraction and Microscopy. *Journal of Vacuum Science & Technology A* **1985**, *3* (3), 1502–1506.

(12) Feenstra, R. M.; Stroscio, J. A.; Tersoff, J.; Fein, A. P. Atom-Selective Imaging of the GaAs(110) Surface. *Phys. Rev. Lett.* **1987**, *58* (12), 1192–1195. https://doi.org/10.1103/PhysRevLett.58.1192.

(13) Duke, C. B.; Meyer, R. J.; Paton, A.; Mark, P.; Kahn, A.; So, E.; Yeh, J. L. Structure Determination for the (110) Surface of Zincblende Structure Compound Semiconductors. *Journal of Vacuum Science and Technology* **1979**, *16* (5), 1252–1257. https://doi.org/10.1116/1.570136.

(14) Feenstra, R. M.; Fein, A. P. Surface Morphology of GaAs(110) by Scanning Tunneling Microscopy. *Phys. Rev. B* **1985**, *32* (2), 1394–1396. https://doi.org/10.1103/PhysRevB.32.1394.

(15) Chung, D. D. L. Review Graphite. *Journal of Materials Science* **2002**, *37* (8), 1475–1489. https://doi.org/10.1023/A:1014915307738.

(16) Hembacher, S.; Giessibl, F.; Mannhart, J.; F Quate, C. Revealing the Hidden Atom in Graphite by Low-Temperature Atomic Force Microscopy. *Proceedings of the National Academy of Sciences of the United States of America* **2003**, *100*, 12539–12542. https://doi.org/10.1073/pnas.2134173100.

(17) Binnig, G.; Rohrer, H.; Gerber, C.; Weibel, E. Surface Studies by Scanning Tunneling Microscopy. *Physical review letters* **1982**, *49* (1), 57.

(18) Griffiths, D. J.; Schroeter, D. F. *Introduction to Quantum Mechanics*; Cambridge University Press, 2018.

(19) Hipps, K. W. Scanning Tunneling Spectroscopy (STS). In *Handbook of Applied Solid State Spectroscopy*; Springer, 2006; pp 305–350.

(20) Moore, J. H.; Davis, C. C.; Coplan, M. A.; Greer, S. C. *Building Scientific Apparatus*; Cambridge University Press, 2009.

(21) Ramsey, N. *Molecular Beams*; OUP Oxford, 1985.

(22) Luth, H.; Rubloff, G. W.; Grobman, W. D. Chemisorption and Decomposition Reactions of Oxygen-Containing Organic Molecules on Clean Pd Surfaces Studied by UV Photoemission. *Surface Science* **1977**, *63* (Supplement C), 325–338. https://doi.org/10.1016/0039-6028(77)90348-X.

(23) van de Meerakker, S. Y. T.; Bethlem, H. L.; Meijer, G. Taming Molecular Beams. *Nat Phys* **2008**, *4* (8), 595–602. https://doi.org/10.1038/nphys1031.

(24) Pan, S. H.; Hudson, E. W.; Davis, J. C. $^3$He Refrigerator Based Very Low Temperature Scanning Tunneling Microscope. *Review of Scientific Instruments* **1999**, *70* (2), 1459–1463. https://doi.org/10.1063/1.1149605.

(25) Nečas, D.; Klapetek, P. Gwyddion: An Open-Source Software for SPM Data Analysis. *Open Physics* **2012**, *10* (1), 181–188.

(26) Engel, T. The Interaction of Molecular and Atomic Oxygen with Si (100) and Si (111). *Surface Science Reports* **1993**, *18* (4), 93–144.

(27) Chabal, Y. J. *Fundamental Aspects of Silicon Oxidation*; Springer-Verlag Berlin Heidelberg, 2001.

(28) Stiévenard, D.; Legrand, B. Silicon Surface Nano-Oxidation Using Scanning Probe Microscopy. *Progress in Surface Science* **2006**, *81* (2–3), 112–140. https://doi.org/10.1016/j.progsurf.2006.01.003.

(29) Okuyama, K.; Sugimura, A.; Sunami, H. Optimized Silicidation Technique for Source and Drain of Fin-Type Field-Effect Transistor. *Japanese Journal of Applied Physics* **2008**, *47* (4), 2407–2409. https://doi.org/10.1143/JJAP.47.2407.

(30) Liu, Y.; Sugimata, E.; Ishii, K.; Masahara, M.; Endo, K.; Matsukawa, T.; Yamauchi, H.; O'uchi, S.; Suzuki, E. Experimental Study of Effective Carrier Mobility of Multi-Fin-Type Double-Gate Metal–Oxide–Semiconductor Field-Effect Transistors with (111) Channel Surface Fabricated by Orientation-Dependent Wet Etching. *Japanese Journal of Applied Physics* **2006**, *45* (4B), 3084–3087. https://doi.org/10.1143/JJAP.45.3084.

(31) Martel, R.; Avouris, P.; Lyo, I. W. Molecularly Adsorbed Oxygen Species on Si (111)-(7×7): STM-Induced Dissociative Attachment Studies. *Science* **1996**, *272* (5260), 385–388.

(32) Jensen, J. A.; Yan, C.; Kummel, A. C. Direct Chemisorption Site Selectivity for Molecular Halogens on the Si(111)- (7×7) Surface. *Phys. Rev. Lett.* **1996**, *76* (8), 1388–1391. https://doi.org/10.1103/PhysRevLett.76.1388.

(33) Kim, K.-Y.; Shin, T.-H.; Han, S.-J.; Kang, H. Identification of the Precursor State in the Initial Stages of $\mathrm{Si}(111)- (7×7) Oxidation. *Phys. Rev. Lett.* **1999**, *82* (6), 1329–1332. https://doi.org/10.1103/PhysRevLett.82.1329.

(34) Höfer, U.; Morgen, P.; Wurth, W.; Umbach, E. Initial Stages of Oxygen Adsorption on Si(111). II. The Molecular Precursor. *Phys. Rev. B* **1989**, *40* (2), 1130–1145. https://doi.org/10.1103/PhysRevB.40.1130.

(35) Gupta, P.; Mak, C. H.; Coon, P. A.; George, S. M. Oxidation Kinetics of Si (111)-7×7 in the Submonolayer Regime. *Physical Review B* **1989**, *40* (11), 7739–7749.

(36) Okuyama, H.; Aruga, T.; Nishijima, M. Vibrational Characterization of the Oxidation Products on S i (111)-(7×7). *Physical review letters* **2003**, *91* (25), 256102/1-4.

(37) Niu, C.-Y.; Wang, J.-T. Adsorption and Dissociation of Oxygen Molecules on Si (111)-(7×7) Surface. *The Journal of chemical physics* **2013**, *139* (19), 194709/1-5.

(38) Lee, S.-H.; Kang, M.-H. Electronic and Vibrational Properties of Initial-Stage Oxidation Products on Si (111)-7×7. *Physical Review B* **2000**, *61* (12), 8250–8255.

(39) Lee, S.-H.; Kang, M.-H. Identification of the Initial-Stage Oxidation Products on Si(111)-7×7. *Phys. Rev. Lett.* **1999**, *82* (5), 968–971. https://doi.org/10.1103/PhysRevLett.82.968.

(40) Schubert, B.; Avouris, P.; Hoffmann, R. A Theoretical Study of the Initial Stages of Si (111)–7×7 Oxidation. I. The Molecular Precursor. *The Journal of chemical physics* **1993**, *98* (9), 7593–7605.

(41) Schubert, B.; Avouris, P.; Hoffmann, R. A Theoretical Study of the Initial Stages of Si (111)–7×7 Oxidation. II. The Dissociated State and Formation of $SiO_4$. *The Journal of chemical physics* **1993**, *98* (9), 7606–7612.

(42) Avouris, P.; Lyo, I.-W.; Bozso, F. Atom-Resolved Surface Chemistry: The Early Steps of Si (111)-7×7 Oxidation. *Journal of Vacuum Science & Technology B* **1991**, *9* (2), 424–430.

(43) Lyo, I. W.; Avouris, P.; Schubert, B.; Hoffmann, R. Elucidation of the Initial Stages of the Oxidation of Silicon (111) Using Scanning Tunneling Microscopy and Spectroscopy. *Journal of Physical Chemistry* **1990**, *94* (11), 4400–4403.

(44) Leibsle, F. M.; Samsavar, A.; Chiang, T.-C. Oxidation of Si (111)-7×7 as Studied by Scanning Tunneling Microscopy. *Physical Review B* **1988**, *38* (8), 5780–5784.

(45) Mayne, A. J.; Rose, F.; Comtet, G.; Hellner, L.; Dujardin, G. Variable Temperature STM Studies of the Adsorption of Oxygen on the Si(1 1 1)-7×7 Surface. *Surface Science* **2003**, *528* (1–3), 132–137. https://doi.org/10.1016/S0039-6028(02)02622-5.

(46) Kinahan, N. T.; Meehan, D. E.; Narushima, T.; Sachert, S.; Boland, J. J.; Miki, K. Site-Specific Evolution of Surface Stress during the Room-Temperature Oxidation of the Si (111)-(7×7) Surface. *Physical review letters* **2010**, *104* (14), 146101/1-4.

(47) Yoshigoe, A.; Teraoka, Y. Immediate Product after Exposing Si (111)-7×7 Surface to $O_2$ at 300 K. *Japanese Journal of Applied Physics* **2010**, *49* (11R), 115704/1-6.

(48) Lee, D. Y.; Kautz, N. A.; Kandel, S. A. Reactivity of Gas-Phase Radicals with Organic Surfaces. *J. Phys. Chem. Lett.* **2013**, *4* (23), 4103–4112. https://doi.org/10.1021/jz401691w.

(49) Lee, D. Y.; Kandel, S. A. Communication: Site-Dependent Reactivity between Chlorine Atoms and Mixed-Chain-Length Alkanethiolate Monolayers. *The Journal of Chemical Physics* **2013**, *139* (16), 161103. https://doi.org/10.1063/1.4827101.

(50) Hundt, P. M.; Jiang, B.; Reijzen, M. E. van; Guo, H.; Beck, R. D. Vibrationally Promoted Dissociation of Water on Ni(111). *Science* **2014**, *344* (6183), 504–507. https://doi.org/10.1126/science.1251277.

(51) Campbell, V. L.; Chen, N.; Guo, H.; Jackson, B.; Utz, A. L. Substrate Vibrations as Promoters of Chemical Reactivity on Metal Surfaces. *J. Phys. Chem. A* **2015**, *119* (50), 12434–12441. https://doi.org/10.1021/acs.jpca.5b07873.

(52) Moritani, K.; Okada, M.; Teraoka, Y.; Yoshigoe, A.; Kasai, T. Kinetics of Oxygen Adsorption and Initial Oxidation on Cu (110) by Hyperthermal Oxygen Molecular Beams. *The Journal of Physical Chemistry A* **2009**, *113* (52), 15217–15222.

(53) Rettner, C. T.; Mullins, C. B. Dynamics of the Chemisorption of $O_2$ on Pt (111): Dissociation via Direct Population of a Molecularly Chemisorbed Precursor at High Incidence Kinetic Energy. *The Journal of chemical physics* **1991**, *94* (2), 1626–1635.

(54) Davis, J. E.; Nolan, P. D.; Karseboom, S. G.; Mullins, C. B. Kinetics and Dynamics of the Dissociative Chemisorption of Oxygen on Ir(111). *The Journal of Chemical Physics* **1997**, *107* (3), 943–952. https://doi.org/10.1063/1.474447.

(55) Sjövall, P.; Uvdal, P. Oxygen Sticking on Pd(111): Double Precursors, Corrugation and Substrate Temperature Effects. *Chemical Physics Letters* **1998**, *282* (5–6), 355–360. https://doi.org/10.1016/S0009-2614(97)01293-1.

(56) Nolan, P. D.; Lutz, B. R.; Tanaka, P. L.; Davis, J. E.; Mullins, C. B. Molecularly Chemisorbed Intermediates to Oxygen Adsorption on Pt (111): A Molecular Beam and Electron Energy-Loss Spectroscopy Study. *The Journal of chemical physics* **1999**, *111* (8), 3696–3704.

(57) Nolan, P. D.; Lutz, B. R.; Tanaka, P. L.; Davis, J. E.; Mullins, C. B. Translational Energy Selection of Molecular Precursors to Oxygen Adsorption on Pt (111). *Physical review letters* **1998**, *81* (15), 3179–3182.

(58) Yan, C.; Jensen, J. A.; Kummel, A. C. Scanning Tunneling Microscopy of the Effect of Incident Energy upon Chemisorption Sites for $O_2$/Si(111)-7×7. *The Journal of Chemical Physics* **1996**, *105* (2), 773–778. https://doi.org/10.1063/1.471887.

(59) Yoshigoe, A.; Teraoka, Y. Synchrotron Radiation Photoelectron Spectroscopy Study on Oxide Evolution during Oxidation of a Si(111)-7 × 7 Surface at 300 K: Comparison of Thermal Equilibrium Gas and Supersonic Molecular Beams for Oxygen Adsorption. *J. Phys. Chem. C* **2014**, *118* (18), 9436–9442. https://doi.org/10.1021/jp410821r.

(60) Yoshigoe, A.; Teraoka, Y. Adsorption Dynamics on Si (111)-7×7 Surface Induced by Supersonic $O_2$ Beam Studied Using Real-Time Photoelectron Spectroscopy. *The Journal of Physical Chemistry C* **2010**, *114* (51), 22539–22545.

(61) Yoshigoe, A.; Teraoka, Y. Atomic Lineation of Products during Oxidation of Si (111)-7×7 Surface Using $O_2$ at 300 K. *The Journal of Physical Chemistry C* **2012**, *116* (6), 4039–4043.

(62) Onoda, J.; Ondráček, M.; Yurtsever, A.; Jelínek, P.; Sugimoto, Y. Initial and Secondary Oxidation Products on the Si (111)-(7×7) Surface Identified by Atomic Force Microscopy and First Principles Calculations. *Applied Physics Letters* **2014**, *104* (13), 133107/1-4.

(63) Dujardin, G.; Mayne, A.; Comtet, G.; Hellner, L.; Jamet, M.; Le Goff, E.; Millet, P. New Model of the Initial Stages of Si(111)-(7x7) Oxidation. *Phys. Rev. Lett.* **1996**, *76* (20), 3782–3785. https://doi.org/10.1103/PhysRevLett.76.3782.

(64) Pelz, J. P.; Koch, R. H. Successive Oxidation Stages and Annealing Behavior of the Si (111) 7×7 Surface Observed with Scanning Tunneling Microscopy and Scanning Tunneling Spectroscopy. *Journal of Vacuum Science & Technology B* **1991**, *9* (2), 775–778.

(65) Hasegawa, T.; Kohno, M.; Hosoki, S. Initial Stage of Oxygen Adsorption onto a Si (111)–7×7 Surface Studied by Scanning Tunneling Microscopy. *Japanese journal of applied physics* **1994**, *33* (6S), 3702–3705.

(66) Pelz, J. P.; Koch, R. H. Successive Oxidation Stages of Adatoms on the Si (111) 7×7 Surface Observed with Scanning Tunneling Microscopy and Spectroscopy. *Physical Review B* **1990**, *42* (6), 3761–3765.

(67) Blyholder, G.; Eyring, H. Kinetics of Graphite Oxidation. *The Journal of Physical Chemistry* **1957**, *61* (5), 682–688.

(68) Strange, J. F.; Walker, P. L. Carbon-Carbon Dioxide Reaction: Langmuir-Hinshelwood Kinetics at Intermediate Pressures. *Carbon* **1976**, *14* (6), 345–350. https://doi.org/10.1016/0008-6223(76)90008-7.

(69) Marchon, B.; Carrazza, J.; Heinemann, H.; Somorjai, G. A. TPD and XPS Studies of $O_2$, $CO_2$, and $H_2O$ Adsorption on Clean Polycrystalline Graphite. *Carbon* **1988**, *26* (4), 507–514. https://doi.org/10.1016/0008-6223(88)90149-2.

(70) Kamioka, I.; Izumi, K.; Kitajima, M.; Kawabe, T.; Ishioka, K.; Nakamura, K. G. Translational Energy Distribution of CO Produced in Infrared-Laser-Assisted Reaction of $O_2$ with a Graphite Surface. *Japanese journal of applied physics* **1998**, *37* (1A), L74.

(71) Olander, D. R.; Siekhaus, W.; Jones, R.; Schwarz, J. A. Reactions of Modulated Molecular Beams with Pyrolytic Graphite. I. Oxidation of the Basal Plane. *The Journal of Chemical Physics* **1972**, *57* (1), 408–420. https://doi.org/10.1063/1.1677980.

(72) Olander, D. R.; Jones, R. H.; Schwarz, J. A.; Siekhaus, W. J. Reactions of Modulated Molecular Beams with Pyrolytic Graphite. II Oxidation of the Prism Plane. *The Journal of Chemical Physics* **1972**, *57* (1), 421–433. https://doi.org/10.1063/1.1677981.

(73) Acharya, T. R.; Olander, D. R. The Rate of Oxidation of the Basal and Prismatic Surfaces of Pyrolytic Graphite in the Transition Regime between Chemical and Diffusional Control. *Carbon* **1973**, *11* (1), 7–18. https://doi.org/10.1016/0008-6223(73)90003-1.

(74) Sun, T.; Yao, X.; Fabris, S. Effects of Thermal Electronic Excitations on the Diffusion of Oxygen Adatoms on Graphene. *J. Phys. Chem. A* **2016**, *120* (17), 2607–2613. https://doi.org/10.1021/acs.jpca.6b00423.

(75) Chang, H.; Bard, A. J. Scanning Tunneling Microscopy Studies of Carbon-Oxygen Reactions on Highly Oriented Pyrolytic Graphite. *Journal of the American Chemical Society* **1991**, *113* (15), 5588–5596.

(76) Chu, X.; Schmidt, L. D. Reactions of NO, $O_2$, $H_2O$, and $CO_2$ with the Basal Plane of Graphite. *Surface Science* **1992**, *268* (1), 325–332. https://doi.org/10.1016/0039-6028(92)90972-9.

(77) Stevens, F.; Kolodny, L. A.; Beebe, T. P. Kinetics of Graphite Oxidation: Monolayer and Multilayer Etch Pits in HOPG Studied by STM. *J. Phys. Chem. B* **1998**, *102* (52), 10799–10804. https://doi.org/10.1021/jp982025e.

(78) Hahn, J. R. Kinetic Study of Graphite Oxidation Along Two Lattice Directions. *Carbon* **2005**, *43* (7), 1506–1511. https://doi.org/10.1016/j.carbon.2005.01.032.

(79) Xu, S. C.; Chen, H.-L.; Lin, M. C. Quantum Chemical Prediction of Reaction Pathways and Rate Constants for the Reactions of $O_x$ (x = 1 and 2) with Pristine and Defective Graphite (0001) Surfaces. *J. Phys. Chem. C* **2012**, *116* (2), 1841–1849. https://doi.org/10.1021/jp206934r.

(80) Wiggins, B.; Avila-Bront, L. G.; Edel, R.; Sibener, S. J. Temporally and Spatially Resolved Oxidation of Si(111)-(7 × 7) Using Kinetic Energy Controlled Supersonic Beams in Combination with Scanning Tunneling Microscopy. *J. Phys. Chem. C* **2016**, *120* (15), 8191–8197. https://doi.org/10.1021/acs.jpcc.6b01360.

(81) Hahn, J. R.; Kang, H. Vacancy and Interstitial Defects at Graphite Surfaces: Scanning Tunneling Microscopic Study of the Structure, Electronic Property, and Yield for Ion-Induced Defect Creation. *Phys. Rev. B* **1999**, *60* (8), 6007–6017. https://doi.org/10.1103/PhysRevB.60.6007.

(82) Lee, S. M.; Lee, Y. H.; Hwang, Y. G.; Hahn, J. R.; Kang, H. Defect-Induced Oxidation of Graphite. *Phys. Rev. Lett.* **1999**, *82* (1), 217–220. https://doi.org/10.1103/PhysRevLett.82.217.

(83) Chu, X.; Schmidt, L. D. Gasification of Graphite Studied by Scanning Tunneling Microscopy. *Carbon* **1991**, *29* (8), 1251–1255. https://doi.org/10.1016/0008-6223(91)90044-J.

(84) Atamny, F.; Schlögl, R.; Wirth, W. J.; Stephan, J. Topochemistry of Graphite Oxidation. *Ultramicroscopy* **1992**, *42*, 660–667. https://doi.org/10.1016/0304-3991(92)90338-K.

(85) Klusek, Z. Scanning Tunneling Microscopy and Spectroscopy of the Thermally Oxidized (0001) Basal Plane of Highly Oriented Pyrolitic Graphite. *Applied Surface Science* **1998**, *125* (3), 339–350. https://doi.org/10.1016/S0169-4332(97)00500-X.

(86) Tandon, D.; Hippo, E. J.; Marsh, H.; Sebok, E. Surface Topography of Oxidized HOPG by Scanning Tunneling Microscopy. *Carbon* **1997**, *35* (1), 35–44. https://doi.org/10.1016/S0008-6223(96)00122-4.

(87) Zhu, Y.-J.; Hansen, T. A.; Ammermann, S.; McBride, J. D.; Beebe, T. P. Nanometer-Size Monolayer and Multilayer Molecule Corrals on HOPG: A Depth-Resolved Mechanistic Study by STM. *J. Phys. Chem. B* **2001**, *105* (32), 7632–7638. https://doi.org/10.1021/jp011377+.

(88) Böttcher, A.; Heil, M.; Stürzl, N.; Jester, S. S.; Malik, S.; Pérez-Willard, F.; Patrice Brenner; Gerthsen, D.; Kappes, M. M. Nanostructuring the Graphite Basal Plane by Focused Ion Beam Patterning and Oxygen Etching. *Nanotechnology* **2006**, *17* (23), 5889. https://doi.org/10.1088/0957-4484/17/23/029.

(89) Paredes, J. I.; Martínez-Alonso, A.; Tascón, J. M. D. Comparative Study of the Air and Oxygen Plasma Oxidation of Highly Oriented Pyrolytic Graphite: A Scanning Tunneling and Atomic Force Microscopy Investigation. *Carbon* **2000**, *38* (8), 1183–1197. https://doi.org/10.1016/S0008-6223(99)00241-9.

(90) Murray, V. J.; Marshall, B. C.; Woodburn, P. J.; Minton, T. K. Inelastic and Reactive Scattering Dynamics of Hyperthermal O and $O_2$ on Hot Vitreous Carbon Surfaces. *The Journal of Physical Chemistry C* **2015**, *119* (26), 14780–14796.

(91) Liu, G. N.-K. *High Temperature Oxidation of Graphite by a Dissociated Oxygen Beam*; 1973.

(92) Sun, T.; Fabris, S.; Baroni, S. Surface Precursors and Reaction Mechanisms for the Thermal Reduction of Graphene Basal Surfaces Oxidized by Atomic Oxygen. *J. Phys. Chem. C* **2011**, *115* (11), 4730–4737. https://doi.org/10.1021/jp111372k.

(93) Poovathingal, S.; Schwartzentruber, T. E.; Srinivasan, S. G.; van Duin, A. C. T. Large Scale Computational Chemistry Modeling of the Oxidation of Highly Oriented Pyrolytic Graphite. *J. Phys. Chem. A* **2013**, *117* (13), 2692–2703. https://doi.org/10.1021/jp3125999.

(94) Carlsson, J. M.; Hanke, F.; Linic, S.; Scheffler, M. Two-Step Mechanism for Low-Temperature Oxidation of Vacancies in Graphene. *Phys. Rev. Lett.* **2009**, *102* (16), 166104. https://doi.org/10.1103/PhysRevLett.102.166104.

(95) Stevens, F.; Beebe, T. P. Computer Modeling of Graphite Oxidation: Differences Between Monolayer and Multilayer Etching. *Computers & Chemistry* **1999**, *23* (2), 175–183. https://doi.org/10.1016/S0097-8485(98)00031-X.

(96) Hahn, J. R.; Kang, H.; Song, S.; Jeon, I. C. Observation of Charge Enhancement Induced by Graphite Atomic Vacancy: A Comparative STM and AFM Study. *Phys. Rev. B* **1996**, *53* (4), R1725–R1728. https://doi.org/10.1103/PhysRevB.53.R1725.

(97) Chu, X.; Schmidt, L. D. Intrinsic Rates of Nitrogen Oxide ($NO_x$)-Carbon Reactions. *Industrial & engineering chemistry research* **1993**, *32* (7), 1359–1366.

(98) Tracz, A.; Wegner, G.; Rabe, J. P. Kinetics of Surface Roughening via Pit Growth During the Oxidation of the Basal Plane of Graphite. 1. Experiments. *Langmuir* **1993**, *9* (11), 3033–3038. https://doi.org/10.1021/la00035a048.

(99) Rodriguez-reinoso, F.; Thrower, P. A. Microscopic Studies of Oxidized Highly Oriented Pyrolytic Graphites. *Carbon* **1974**, *12* (3), 269–279. https://doi.org/10.1016/0008-6223(74)90069-4.

(100) del Alamo, J. A. Nanometre-Scale Electronics with III–V Compound Semiconductors. *Nature* **2011**, *479* (7373), 317–323. https://doi.org/10.1038/nature10677.

(101) Whitesides, George. M. Materials for Advanced Electronic Devices. In *Biotechnology and Materials Science: Chemistry for the Future*; Good, M., L., Baum, R., Peterson, I., Henderson, N., Eds.; American Chemical Society: Washington, DC, 1988; pp 85–99.

(102) Schmuki, P.; Sproule, G. I.; Bardwell, J. A.; Lu, Z. H.; Graham, M. J. Thin Anodic Oxides Formed on GaAs in Aqueous Solutions. *Journal of Applied Physics* **1996**, *79* (9), 7303–7311. https://doi.org/10.1063/1.361524.

(103) Wang, H.-H.; Wu, J.-Y.; Wang, Y.-H.; Houng, M.-P. Effects of PH Values on the Kinetics of Liquid-Phase Chemical-Enhanced Oxidation of GaAs. *J. Electrochem. Soc.* **1999**, *146* (6), 2328–2332. https://doi.org/10.1149/1.1391935.

(104) Telford, M. Progress in GaAs Manufacturing Technology. *III-Vs Review* **2001**, *14* (6), 22–26. https://doi.org/10.1016/S0961-1290(01)80526-3.

(105) Pakes, A.; Skeldon, P.; Thompson, G. E.; Hussey, R. J.; Moisa, S.; Sproule, G. I.; Landheer, D.; Graham, M. J. Composition and Growth of Anodic and Thermal Oxides on InP and GaAs. *Surface and Interface Analysis* **2002**, *34* (1), 481–484. https://doi.org/10.1002/sia.1343.

(106) Lee, H.-Y. Growth of GaAs Oxide Layer Using Photoelectrochemical Method. *Journal of The Electrochemical Society* **2008**, *155* (7), G141. https://doi.org/10.1149/1.2907751.

(107) Lee, H.-Y.; Lin, Y.-F. GaAs Metal-Oxide-Semiconductor Devices with a Complex Gate Oxide Composed of $SiO_2$ and GaAs Oxide Grown Using a Photoelectrochemical Oxidation Method. *Semicond. Sci. Technol.* **2009**, *25* (1), 015005. https://doi.org/10.1088/0268-1242/25/1/015005.

(108) Gucmann, F.; Kúdela, R.; Kordoš, P.; Dobročka, E.; Gaži, Š.; Dérer, J.; Liday, J.; Vogrinčič, P.; Gregušová, D. III-As Heterostructure Field-Effect Transistors with Recessed Ex-Situ Gate Oxide by $O_2$ Plasma-Oxidized GaAs Cap. *Journal of Vacuum Science & Technology B* **2015**, *33* (1), 01A111. https://doi.org/10.1116/1.4905938.

(109) Sharma, H.; Moumanis, K.; Dubowski, J. J. PH-Dependent Photocorrosion of GaAs/AlGaAs Quantum Well Microstructures. *J. Phys. Chem. C* **2016**, *120* (45), 26129–26137. https://doi.org/10.1021/acs.jpcc.6b08844.

(110) Mönch, W. Oxidation of Silicon and III–V Compound Semiconductors. In *Semiconductor Surfaces and Interfaces*; Mönch, W., Ed.; Springer Series in Surface Sciences; Springer Berlin Heidelberg: Berlin, Heidelberg, 2001; pp 353–376. https://doi.org/10.1007/978-3-662-04459-9_17.

(111) Wiggins, B.; Avila-Bront, L. G.; Edel, R.; Sibener, S. J. Temporally and Spatially Resolved Oxidation of Si(111)-(7 × 7) Using Kinetic Energy Controlled Supersonic Beams in Combination with Scanning Tunneling Microscopy. *The Journal of Physical Chemistry C* **2016**, *120* (15), 8191–8197. https://doi.org/10.1021/acs.jpcc.6b01360.

(112) Edel, R.; Grabnic, T.; Wiggins, B.; Sibener, S. J. Atomically-Resolved Oxidative Erosion and Ablation of Basal Plane HOPG Graphite Using Supersonic Beams of $O_2$ with Scanning Tunneling Microscopy Visualization. *The Journal of Physical Chemistry C* **2018**, *122* (26), 14706–14713. https://doi.org/10.1021/acs.jpcc.8b04139.

(113) Frankel, D. J.; Anderson, J. R.; Lapeyre, G. J. UV Photoemission Study of Low Temperature Oxygen Adsorption on GaAs(110). *Journal of Vacuum Science & Technology B: Microelectronics Processing and Phenomena* **1983**, *1* (3), 763–766. https://doi.org/10.1116/1.582688.

(114) Bartels, F.; Surkamp, L.; Clemens, H. J.; Mönch, W. Oxygen and Hydrogen Adsorption on GaAs(110). *Journal of Vacuum Science & Technology B: Microelectronics Processing and Phenomena* **1983**, *1* (3), 756–762. https://doi.org/10.1116/1.582687.

(115) Hughes, G.; Ludeke, R. O 1s Studies of the Oxidation of InP(110) and GaAs(110) Surfaces. *Journal of Vacuum Science & Technology B: Microelectronics Processing and Phenomena* **1986**, *4* (4), 1109–1114. https://doi.org/10.1116/1.583551.

(116) Mönch, W. On the Oxidation of III–V Compound Semiconductors. *Surface Science* **1986**, *168* (1), 577–593. https://doi.org/10.1016/0039-6028(86)90889-7.

(117) Bartels, F.; Mönch, W. On the Growth Mode of Oxide Films on Cleaved GaAs(110) Surfaces at Room Temperature. *Solid State Communications* **1986**, *57* (8), 571–574. https://doi.org/10.1016/0038-1098(86)90323-6.

(118) Bartels, F.; Mönch, W. Oxidation Mechanism of III–V Semiconductors. *Vacuum* **1990**, *41* (1), 667–668. https://doi.org/10.1016/S0042-207X(05)80156-3.

(119) Landgren, G.; Ludeke, R.; Jugnet, Y.; Morar, J. F.; Himpsel, F. J. The Oxidation of GaAs(110): A Reevaluation. *Journal of Vacuum Science & Technology B: Microelectronics Processing and Phenomena* **1984**, *2* (3), 351–358. https://doi.org/10.1116/1.582823.

(120) Landgren, G.; Ludeke, R.; Morar, J. F.; Jugnet, Y.; Himpsel, F. J. Oxidation of GaAs(110): New Results and Models. *Physical Review B* **1984**, *30* (8), 4839–4841. https://doi.org/10.1103/PhysRevB.30.4839.

(121) Bertness, K. A.; Yeh, J.-J.; Friedman, D. J.; Mahowald, P. H.; Wahi, A. K.; Kendelewicz, T.; Lindau, I.; Spicer, W. E. Growth Structure of Chemisorbed Oxygen on GaAs(110) and InP(110) Surfaces. *Physical Review B* **1988**, *38* (8), 5406–5421. https://doi.org/10.1103/PhysRevB.38.5406.

(122) Cabrera, N.; Mott, N. F. Theory of the Oxidation of Metals. *Rep. Prog. Phys.* **1949**, *12* (1), 163–184. https://doi.org/10.1088/0034-4885/12/1/308.

(123) Pianetta, P.; Lindau, I.; Garner, C. M.; Spicer, W. E. Oxidation Properties of GaAs (110) Surfaces. *Physical Review Letters* **1976**, *37* (17), 1166–1169. https://doi.org/10.1103/PhysRevLett.37.1166.

(124) Pianetta, P.; Lindau, I.; Garner, C.; Spicer, W. E. Determination of the Oxygen Binding Site on GaAs(110) Using Soft-X-Ray-Photoemission Spectroscopy. *Physical Review Letters* **1975**, *35* (20), 1356–1359. https://doi.org/10.1103/PhysRevLett.35.1356.

(125) Pianetta, P.; Lindau, I.; Garner, C. M.; Spicer, W. E. Chemisorption and Oxidation Studies of the (110) Surfaces of GaAs, GaSb, and InP. *Physical Review B* **1978**, *18* (6), 2792–2806. https://doi.org/10.1103/PhysRevB.18.2792.

(126) Ludeke, R. The Oxidation of the GaAs (110) Surface. *Solid State Communications* **1977**, *21* (8), 815–818. https://doi.org/10.1016/0038-1098(77)91160-7.

(127) Ludeke, R. Oxidation Properties of GaAs (110) Surfaces. *Physical Review B* **1977**, *16* (12), 5598–5599. https://doi.org/10.1103/PhysRevB.16.5598.

(128) Brundle, C. R.; Seybold, D. Oxygen Interaction with GaAs Surfaces: An XPS/UPS Study. *Journal of Vacuum Science and Technology* **1979**, *16* (5), 1186–1190. https://doi.org/10.1116/1.570187.

(129) Tsai, M.-H.; Packard, W. E.; Dow, J. D.; Kasowski, R. V. Oxidation of the GaAs(110) Surface. *Physica B: Condensed Matter* **1993**, *192* (4), 365–370. https://doi.org/10.1016/0921-4526(93)90012-U.

(130) Spicer, W. E.; Lindau, I.; Gregory, P. E.; Garner, C. M.; Pianetta, P.; Chye, P. W. Synchrotron Radiation Studies of Electronic Structure and Surface Chemistry of GaAs, GaSb, and InP. *Journal of Vacuum Science and Technology* **1976**, *13* (4), 780–785. https://doi.org/10.1116/1.568989.

(131) Dorn, R.; Lüth, H.; Russell, G. J. Adsorption of Oxygen on Clean Cleaved (110) Gallium-Arsenide Surfaces. *Physical Review B* **1974**, *10* (12), 5049–5056. https://doi.org/10.1103/PhysRevB.10.5049.

(132) Chye, P. W.; Pianetta, P.; Lindau, I.; Spicer, W. E. Oxygen Sorption and Excitonic Effects on GaAs Surfaces. *Journal of Vacuum Science and Technology* **1977**, *14* (4), 917–919. https://doi.org/10.1116/1.569328.

(133) Ludeke, R.; Koma, A. Electronic Surface States on Clean and Oxygen-exposed GaAs Surfaces. *Journal of Vacuum Science and Technology* **1976**, *13* (1), 241–247. https://doi.org/10.1116/1.568859.

(134) Stroscio, J. A.; Feenstra, R. M.; Fein, A. P. Structure of Oxygen Adsorbed on the GaAs(110) Surface Studied Using Scanning Tunneling Microscopy. *Phys. Rev. B* **1987**, *36* (14), 7718–7721. https://doi.org/10.1103/PhysRevB.36.7718.

(135) Kruse, P.; McLean, J. G.; Kummel, A. C. Relative Reactivity of Arsenic and Gallium Dimers and Backbonds during the Adsorption of Molecular Oxygen on GaAs(100)(6×6). *J. Chem. Phys.* **2000**, *113* (20), 9217–9223. https://doi.org/10.1063/1.1315599.

(136) Kruse, P.; McLean, J. G.; Kummel, A. C. Chemically Selective Adsorption of Molecular Oxygen on GaAs(100)-(2×8). *The Journal of Chemical Physics* **2000**, *113* (20), 9224–9232. https://doi.org/10.1063/1.1315600.

(137) Passlack, M.; Hong, M.; Mannaerts, J. P.; Opila, R. L.; Ren, F. Thermodynamic and Photochemical Stability of Low Interface State Density $Ga_2O_3$–GaAs Structures Fabricated by in Situ Molecular Beam Epitaxy. *Appl. Phys. Lett.* **1996**, *69* (3), 302–304. https://doi.org/10.1063/1.118040.

(138) Feenstra, R. M.; Stroscio, J. A.; Tersoff, J.; Fein, A. P. Atom-Selective Imaging of the GaAs(110) Surface. *Physical Review Letters* **1987**, *58* (12), 1192–1195. https://doi.org/10.1103/PhysRevLett.58.1192.

(139) Stroscio, J. A.; Feenstra, R. M.; Fein, A. P. Local State Density and Long-Range Screening of Adsorbed Oxygen Atoms on the GaAs(110) Surface. *Physical Review Letters* **1987**, *58* (16), 1668–1671. https://doi.org/10.1103/PhysRevLett.58.1668.

(140) Moriarty, P.; Hughes, G. An Investigation of the Early Stages of Native Oxide Growth on Chemically Etched and Sulfur-Treated GaAs(100) and InP(100) Surfaces by Scanning Tunnelling Microscopy. *Ultramicroscopy* **1992**, *42–44*, 956–961. https://doi.org/10.1016/0304-3991(92)90385-W.

(141) Nevo, I.; Aloni, S.; Cohen, S. R.; Hasse, G. The Effect of Adsorbed Oxygen on the Surface Potential of N-GaAs(110). *The Journal of Chemical Physics* **2005**, *123* (6), 064705. https://doi.org/10.1063/1.1997127.

(142) Hollinger, G.; Hughes, G.; Himpsel, F. J.; Jordan, J. L.; Morar, J. F.; Houzay, F. Early Stages in the Formation of the Oxide-InP(110) Interface. *Surface Science* **1986**, *168* (1), 617–625. https://doi.org/10.1016/0039-6028(86)90892-7.

(143) Piercy, P.; Castonguay, A. M.-J. Diffusion-Limited Kinetics of Terrace Growth on GaAs(110). *Physical Review B* **2005**, *72* (11). https://doi.org/10.1103/PhysRevB.72.115420.

(144) Pechman, R. J.; Wang, X.-S.; Weaver, J. H. Vacancy Kinetics and Sputtering of GaAs(110). *Physical Review B* **1995**, *51* (16), 10929–10936. https://doi.org/10.1103/PhysRevB.51.10929.

(145) Wang, X.-S.; Pechman, R. J.; Weaver, J. H. Trends in Surface Roughening: Analysis of Ion-Sputtered GaAs(110). *Surface Science* **1996**, *364* (1), L511–L518. https://doi.org/10.1016/0039-6028(96)00768-6.

(146) Barrett, N. T.; Greaves, G. N.; Pizzini, S.; Roberts, K. J. The Local Atomic Structure of the Oxide Coating on Polished GaAs(100). *Surface Science* **1990**, *227* (3), 337–346. https://doi.org/10.1016/S0039-6028(05)80022-6.

(147) Proietti, M. G.; Garcia, J.; Chaboy, J.; Morier-Genoud, F.; Martin, D. Structural Properties of GaAs Oxide Layers Grown on Polished (100) Surfaces. *J. Phys.: Condens. Matter* **1993**, *5* (9), 1229–1238. https://doi.org/10.1088/0953-8984/5/9/008.

(148) Thurmond, C. D.; Schwartz, G. P.; Kammlott, G. W.; Schwartz, B. GaAs Oxidation and the Ga-As-O Equilibrium Phase Diagram. *J. Electrochem. Soc.* **1980**, *127* (6), 1366–1371. https://doi.org/10.1149/1.2129900.

(149) Donnelly, K. Simulations to Determine the Variance and Edge-Effect of Total Nearest Neighbour Distance. In *Simulation Methods in Archaeology*; Hodder, I., Ed.; Cambridge University Press: London, 1978; pp 91–95.